# Dispersion Engineering of Surface Plasmon Polaritons

by

**Hüseyin Serhat Tetikol**

A Dissertation Submitted to the
Graduate School of Sciences and Engineering
in Partial Fulfillment of the Requirements for
the Degree of

Doctor of Philosophy

in

Electrical and Electronics Engineering

KOÇ ÜNİVERSİTESİ

September 7, 2020

**Dispersion Engineering of Surface Plasmon Polaritons**

Koç University

Graduate School of Sciences and Engineering

This is to certify that I have examined this copy of a doctoral dissertation by

**Hüseyin Serhat Tetikol**

and have found that it is complete and satisfactory in all respects,

and that any and all revisions required by the final

examining committee have been made.

Committee Members:

Prof. M. İrsadi Aksun (Advisor)

Prof. Alper T. Erdoğan

Prof. Özgür E. Müstecaplıoğlu

Prof. Vakur B. Erturk

Assoc. Prof. Lale H. Alatan

Date:

*To the pursuit of understanding, and a lifetime of learning...*

# ABSTRACT

**Dispersion Engineering of Surface Plasmon Polaritons**
**Hüseyin Serhat Tetikol**
**Doctor of Philosophy in Electrical and Electronics Engineering**
**September 7, 2020**

Surface plasmon polaritons (SPPs) and their features have been scrutinized and documented in the scientific literature for decades. Experimental configurations that can excite and exploit SPP modes have been developed. The characteristic phenomena related to SPPs such as local field enhancement, electromagnetic energy confinement, increased absorption of incident light have formed the basis of many novel applications. Significant improvements in spectroscopic methods, sensors, solar cells, nanoparticle-based targeted disease solutions have been enabled by the use of SPPs. However, this fast pace of advancement in the field seems to have left behind several important pieces missing in its theoretical foundations. The purpose of this thesis is to uncover these pieces, investigate them in detail, resolve some of the current discussions in the literature, and finally show how a thorough understanding of SPP modes opens up new venues for improvement in essentially any plasmonic system.

In this thesis, the SPP modes in layered media are analyzed by taking into account all facets of the electromagnetic response of the plasmonic structure, without any prior assumptions about whether the modes are physical/proper or unphysical/improper. It is shown that all extrema defining the response of the structure, including the ones that are seemingly unphysical and usually dismissed as such in other studies, are responsible for the SPP phenomena and experimental measurements in realistic scenarios. This is achieved by a detailed investigation of the Riemann sheets that show up in the evaluation of the electromagnetic response of plasmonic structures, and by establishing connections between the modes on different Riemann sheets. Based on this exhaustive analysis of SPP modes, optimal values for parameters such as the metal film thickness and the dielectric constant are discussed for various experimental purposes.

Surface plasmon dispersion relation is also analyzed and shown to support a much richer domain of SPP modes than what is commonly assumed in the literature. In this thesis, we refrain from prematurely applying any conditions that originate from pre-existing physical intuitions and only rely on the mathematical restrictions that are imposed by the boundary conditions of the problem. This enables the expansion of the dispersion relation to the third dimension as a surface rather than just a curve, resulting in SPP modes with simultaneous complex frequencies and complex wave vectors. The connection between the SPP modes on this dispersion surface and the temporal and spatial boundary conditions is also established. These results are applied to two popular examples in plasmonics: A metal-dielectric-metal plasmonic waveguide and the super lens which provides resolution beyond the diffraction limit. In each case, it is shown that the features such as image resolution, mode propagation length and field confinement can be dramatically improved using the dispersion surface compared to conventional approaches.

# ÖZETÇE

**Yüzey Plazmon Polaritonlarının Dispersiyon Mühendisliği**
**Hüseyin Serhat Tetikol**
**Elektrik ve Elektronik Mühendisliği, Doktora**
**7 Eylül 2020**

Yüzey plazmon polaritonları (SPP'ler) ve özellikleri, onlarca yıldır bilimsel literatürde incelenmiş ve belgelenmiştir. SPP modlarını harekete geçirebilen ve kullanabilen deneysel konfigürasyonlar geliştirilmiştir. Yerel elektrik alanın şiddetlenmesi, elektromanyetik enerjinin lokalize olması, gelen ışığın yüksek verimle emilimi gibi SPP'lerle ilgili karakteristik özellikler, birçok yeni uygulamanın temelini oluşturmuştur. SPP'lerin kullanılması sayesinde spektroskopik yöntemler, sensörler, güneş pilleri, nanoparçacık bazlı tedaviler gibi birçok alanda önemli gelişmeler sağlanmıştır. Fakat plazmonik alanındaki bu hızlı ve önemli gelişmeler, yüzey plazmonlarının teorik temellerinde birtakım konuların eksik kalmasına sebep olmuştur. Bu tezin amacı, eksik kalan bu konuları ortaya çıkarmak, ayrıntılı olarak incelemek, literatürdeki bir takım güncel tartışmaları sonuçlandırmak ve SPP modlarının kapsamlı olarak anlaşılmasını sağlayarak plazmonik sistemlerin iyileştirilmesi için yeni alanlar açılabileceğini göstermektir.

Bu tezde, katmanlı ortamdaki SPP modları, modların fiziksel olup olmadığına dair herhangi bir varsayım olmaksızın, plazmonik yapının elektromanyetik tepkisinin tüm yönleri dikkate alınarak analiz edilmiştir. Görünüşte fiziksel olmayan ve bu sebeple diğer bilimsel çalışmalarda göz ardı edilen modlar da dahil olmak üzere, plazmonik yapının tepkisini tanımlayan tüm minimum ve maksimumların, SPP özelliklerinin ve gerçekçi deneysel senaryolardaki ölçümlerin açıklamasında rol oynadığı gösterilmiştir. Bu, plazmonik yapıların elektromanyetik tepkisinin hesaplanmasında ortaya çıkan Riemann yüzeylerinin ayrıntılı incelenmesi ve farklı Riemann yüzeylerinin üzerindeki modlar arasında bağlantılar kurulmasıyla sağlanmıştır. SPP modlarının bu kapsamlı analizine dayanarak, metal film kalınlığı ve dielektrik sabiti gibi parametreler için optimal değerler, çeşitli deneysel amaçlara yönelik olarak tartışılmıştır.

Yüzey plazmon dispersiyon ilişkisi de analiz edilmiş ve literatürdeki genel kabulün aksine yüzey plazmon dispersiyon ilişkisinin çok daha zengin bir SPP mod içeriğine sahip olduğu gösterilmiştir. Bu tezde, kabul görmüş fiziksel çıkarımların öne sürdüğü koşullardan bağımsız, yalnızca problemin sınır koşullarının dayattığı matematiksel kısıtlamaları referans alan bir yaklaşım benimsenmiştir. Bu yaklaşım, SPP dispersiyon ilişkisinin sadece bir eğri değil, bir yüzey olarak üçüncü boyuta genişletilmesini mümkün kılarak, eşzamanlı karmaşık frekans ve karmaşık dalga vektörüne sahip SPP modlarının varlığını ispatlamaktadır. Dispersiyon yüzeyindeki SPP modları ile zamansal ve uzamsal sınır koşulları arasındaki bağlantı da kurulmuştur. Bu sonuçlar, plazmonik alanındaki iki popüler örneğe uygulanmıştır: Biri metal-dielektrik-metal plazmonik dalga kılavuzu, diğeri kırınım sınırının ötesinde çözünürlük sağlayan plazmonik süper lens. Bu örneklerle, görüntü çözünürlüğü, mod yayılma uzunluğu ve elektromanyetik alan lokalizasyonu gibi özelliklerin, geleneksel yaklaşımlarla karşılaştırıldığında, dispersiyon yüzeyi kullanılarak önemli ölçüde geliştirilebileceği gösterilmiştir.

## ACKNOWLEDGMENTS

First, I would like to thank my advisor M. İrşadi Aksun for all the time and help he provided during my PhD. He has been much more than a scientific advisor for me. Not only did he guide me in my academic journey, but he has also been extremely supportive of my other adventures during my PhD years, including my startup and my exposure to industry. I am indebted to him for creating an environment of learning, sharing and growing, not just in science but in many aspects of life.

I would also like to thank my thesis monitoring committee members Özgür Müstecaplıoğlu and Alper Erdoğan for providing valuable feedback on my PhD work. In addition, I would like to thank Kaan Güven for dedicating his time to attend my committee meetings and sharing his invaluable comments.

My lifelong friends Musa Murat Öz, Emre Doruk Önal, Alhun Aydın and Erdi Aktan have helped me in many ways throughout my PhD years. I highly treasure their friendship.

My family has always been supportive of my decisions at all stages of my life. This PhD is no exception. I dearly value the in-depth discussions we had together with my mother and father about plasmonics, metamaterials, and physics in general. They have also equipped me with the tools that help me become an honest and loving person, and only after that, a scientist.

Last but foremost, my dear wife Deniz has been a constant source of love, comfort and peace throughout my life. She has been the beacon that all of my endeavors lead to. All of this would be meaningless if it was not for her.

# TABLE OF CONTENTS

# LIST OF TABLES

# LIST OF FIGURES

# ABBREVIATIONS

| | |
|---|---|
| SPP | Surface Plasmon Polariton or Surface Plasmon |
| KRC | Kretschmann-Raether Configuration |
| MIM | Metal-Insulator-Metal |
| IMI | Insulator-Metal-Insulator |
| FDTD | Finite-Difference Time-Domain |

Chapter 1

# INTRODUCTION & FUNDAMENTALS OF PLASMONICS

## 1.1 Introduction

Plasmonics has been a promising field in electromagnetics that study the interaction of electromagnetic waves and metallic structures and nanoparticles. Solutions based on plasmonics have been proposed to tackle some of the most important problems that the world faces today in the fields of energy, health, imaging, electronics, and biotechnology. In the field of energy, plasmonic materials have been used to increase the efficiency of solar panels [1, 2]. In oncology, plasmonic nanoparticles have been proposed as a viable method to target tumor tissue and selectively kill the tumor cells, minimizing the damage to healthy tissue [3]. The clinical trials for such plasmonics-based cures are already in progress. In electronics, plasmonic transistors have been developed, forming the basis of computers essentially working with light [4, 5, 6]. Plasmonic sensors are already available commercially that significantly improve imaging and spectroscopy techniques [7, 8]. Plasmonic systems are also being utilized to improve biosensors and microfluidic devices [9]. Even though we have yet to see a practical realization of many of those solutions at scale, impressive amount of progress has already been done and roadmaps on how best to continue these efforts have been published [10, 11, 12, 13].

In this introductory chapter, we will cover the fundamentals of plasmonics in order to set the stage for more advanced discussions in the following chapters. The basics of electromagnetics will not be covered and it is assumed that the reader already has sound foundations in electromagnetics. In the case of unclarity on any of the topics in this chapter, the reader is referred to several textbooks that arguably serve as cornerstones for understanding electromagnetics and plasmonics [14, 15, 16, 17, 18]. However, it should be noted, as early as possible, that some of the results found in this thesis might seem contrary to what one might read in the books on plasmonics [14, 15]. This is indeed where the novelty of this thesis lies.

This thesis comprises of theoretical work on surface plasmon polaritons in layered media, supported by computational calculations and full-wave electromagnetic simulations. The main purpose of the thesis is to lay the theoretical foundations to enable researchers to engineer plasmonic devices and their dispersion for targeted applications. Although it is a common belief that there is very little undiscovered about the theory of surface plasmons, this thesis provides evidence to the contrary.

In Chapter 2, a complete description of SPPs and their features are provided. Studying electromagnetic modes in multi-layered media, we derive and explain how poles and zeros of the transfer function, i.e. the response of the media, come into play and manifest themselves by investigating their field and energy profiles in detail. We show that many modes, which are commonly discarded as unphysical, indeed have utmost relevance to experiments and influence the observations made in practical plasmonic applications. Furthermore, we prove that the salient features of SPPs such as local field enhancement and extinction of the incident wave are governed by related but distinct mechanisms. Finally, we provide methods to optimize plasmonic devices for different purposes using the independent parameters available in designing a plasmonic device.

In Chapter 3, a fundamentally unconventional but mathematically very simple approach for studying the surface plasmon polariton (SPP) dispersion is proposed. The novelty of this approach is that it opens up a plethora of new SPP modes which were previously undiscovered. This is achieved by bringing the commonly used dispersion curves to a whole new dimension in the complex domain. These new modes can be accessed by tapping into the time dimension of electromagnetic waves and has properties superior to conventional SPPs.

We start by noting some of the basic equations in electromagnetics, which will help us in later sections. Here we note the Maxwell's equations in differential form for macroscopic media and accompanying constitutive relations. In this thesis, we are dealing with macroscopic media at nanoscale whose electromagnetic response can be boiled down to effective permittivity and permeability. Such description of materials has been shown to hold down to several nanometers and slight modifications of macroscopic models can be used to even further this limit [19, 20].

*Maxwell's equations*

$$\nabla \cdot \mathbf{E} = \rho_{free} \tag{1.1a}$$

$$\nabla \cdot \mathbf{B} = 0 \tag{1.1b}$$

$$\nabla \times \mathbf{E} = -\frac{\partial \mathbf{B}}{\partial t} \tag{1.1c}$$

$$\nabla \times \mathbf{H} = J_{free} + \frac{\partial \mathbf{D}}{\partial t} \tag{1.1d}$$

*Constitutive relations*

$$\mathbf{D} = \epsilon\epsilon_0 \mathbf{E} \tag{1.2a}$$

$$\mathbf{H} = \frac{\mathbf{B}}{\mu\mu_0} \tag{1.2b}$$

And here, we write down the boundary conditions that apply to interfaces between macroscopic media, for reference later in the thesis. We do not derive any of these and refer the interested reader to the aforementioned references. Throughout this thesis, we use the $e^{j\omega t}$ convention to represent time dependence of plane waves, also known as the *engineer's convention.* As an example, a plane wave of the form $e^{j\omega t - j\mathbf{kr}}$ would be traveling in the $+\mathbf{k}$ direction.

*Boundary conditions*

$$E_1^{||} - E_2^{||} = 0 \tag{1.3a}$$

$$H_1^{||} - H_2^{||} = J_s \tag{1.3b}$$

$$D_1^{\perp} - D_2^{\perp} = \rho_s \tag{1.3c}$$

$$B_1^{\perp} - B_2^{\perp} = 0 \tag{1.3d}$$

### *1.1.1 Fresnel reflection coefficients*

Plane waves, which have the form of $e^{j\omega t - j\mathbf{kr}}$, are the natural solutions of the wave equation in Cartesian coordinates. The geometries that are studied in this thesis consist of only planar structures, i.e. thin films, that are parallel to each other. Such layered media has translational symmetry in the lateral directions, and each boundary condition (1.3) can easily be written down using only one of the three orthonormal directions $\mathbf{x}$, $\mathbf{y}$ and $\mathbf{z}$ in Cartesian coordinates. For these reasons, we will study plane waves travelling in layered media, which can be used to form the basis for any arbitrary electromagnetic wave.

A two-layered example is shown in Figure 1.1, where two transverse-magnetic (TM) planes waves are travelling in each layer. In a typical experimental scenario, there is a plane wave incident on the boundary between the two layers on one side ($H_1^+$), resulting in a reflected wave in the medium of incidence ($H_1^-$) and a transmitted wave in the other layer ($H_2^+$). We assume there are no incoming waves from the $+\mathbf{z}$ direction, hence $H_2^- = 0$.

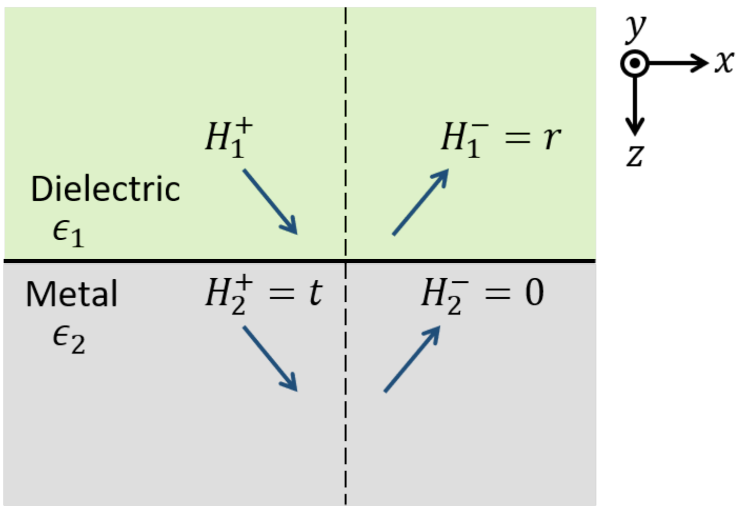


Figure 1.1: The steady-state TM fields in two semi-infinite media

The magnetic fields for these TM waves in the first and the second layers can be described as equations (1.4) and (1.5), respectively.

$$\mathbf{H}_1 = \hat{\mathbf{y}}(H_1^+ e^{-jk_{z1}z} + H_1^- e^{+jk_{z1}z})e^{-jk_x x} \tag{1.4}$$

$$\mathbf{H}_2 = \hat{\mathbf{y}} H_2^+ e^{-jk_{z2}z} e^{-jk_x x} \tag{1.5}$$

The normal ($\mathbf{z}$) component of the wave vector is defined as $k_{zi} = \sqrt{\epsilon_i k_0^2 - k_x^2}$ in medium $i$, where $k_0 = 2\pi/\lambda$ is the wave number and $\lambda$ is the wavelength in free space. The electric fields can further be written down as (1.6) and (1.7), using the Ampere's law (1.1d).

$$\begin{aligned}\mathbf{E}_1 = \Bigg[\hat{\mathbf{x}} \frac{k_{z1}}{\omega\epsilon_1\epsilon_0}&(H_1^+ e^{-jk_{z1}z} - H_1^- e^{+jk_{z1}z}) \\ &- \hat{\mathbf{z}} \frac{k_x}{\omega\epsilon_1\epsilon_0}(H_1^+ e^{-jk_{z1}z} + H_1^- e^{+jk_{z1}z})\Bigg] e^{-jk_x x}\end{aligned} \tag{1.6}$$

$$\mathbf{E}_2 = \left[\hat{\mathbf{x}} \frac{k_{z2}}{\omega\epsilon_2\epsilon_0} H_2^+ e^{-jk_{z2}z} - \hat{\mathbf{z}} \frac{k_x}{\omega\epsilon_2\epsilon_0} H_2^+ e^{-jk_{z2}z}\right] e^{-jk_x x} \tag{1.7}$$

In the absence of any external surface current density at the interface ($z = 0$), the electromagnetic boundary conditions (1.3a) and (1.3b) dictate that $\mathbf{H}_1 = \mathbf{H}_2$ and $\mathbf{y} \cdot \mathbf{E}_1 = \mathbf{y} \cdot \mathbf{E}_2$. Applying these conditions, we get

$$\begin{aligned} H_1^+ + H_1^- &= H_2^+ \\ \frac{k_{z1}}{\omega\epsilon_1}(H_1^+ - H_1^-) &= \frac{k_{z2}}{\omega\epsilon_2} H_2^+ \end{aligned}$$

Rearranging these equations, it is possible to define the reflection and transmission coefficients as below.

$$r^{TM} = \frac{H_1^-}{H_1^+} = \frac{\epsilon_2 k_{z1} - \epsilon_1 k_{z2}}{\epsilon_2 k_{z1} + \epsilon_1 k_{z2}} \tag{1.8a}$$

$$t^{TM} = \frac{H_2^+}{H_1^+} = \frac{2\epsilon_2 k_{z1}}{\epsilon_2 k_{z1} + \epsilon_1 k_{z2}} \tag{1.8b}$$

It is important to emphasize that these equations represent the *response* of the medium to an excitation with a unity amplitude ($H_1^+ = 1$). We will repeatedly rely on this interpretation when we investigate electromagnetic surface modes in plasmonic waveguides. It will prove vital to not lose sight of the fundamental intuitions we establish when analyzing more complicated structures or excitations.

One trivial but easy-to-miss remark should be made here. We already implicitly enforced the boundary conditions in writing down the expressions (1.4), (1.5), (1.6), (1.7); that is, we assumed that the tangential wave vector component $k_x$ for all plane waves is the same. The conservation of tangential wave vector is indeed a result of the boundary conditions, since, otherwise, it would be impossible for tangential fields on both sides of an interface to be equal. An elementary but useful discussion is given in Ref [17].

The derivations will not be provided here, however, for completeness, one can follow a similar procedure to obtain the Fresnel reflection and transmission coefficients for transverse electric (TE) waves (waves that have non-zero electric field only in the $\mathbf{y}$ direction).

$$r^{TE} = \frac{E_1^-}{E_1^+} = \frac{\mu_2 k_{z1} - \mu_1 k_{z2}}{\mu_2 k_{z1} + \mu_1 k_{z2}} \tag{1.9a}$$

$$t^{TE} = \frac{E_2^+}{E_1^+} = \frac{2\mu_2 k_{z1}}{\mu_2 k_{z1} + \mu_1 k_{z2}} \tag{1.9b}$$

In Figure 1.2, the TM reflection coefficient between vacuum ($\epsilon = 1$) and a glass with $\epsilon = 4$ is plotted. Specifically, we plot the *reflectance* ($R = |r|^2$), which is the reflected power, and the transmittance ($T = 1 - R$), which is the transmitted power. The derivations for these expressions are not provided here and can be found in any elementary textbook on electromagnetics.

Figure 1.2 (a) shows the reflection coefficient when the light is incident from the vacuum side. Note that the tangential component of the wave vector for propagating incident waves in vacuum cannot be larger than the free space wave number $k_0$. Also notice that there exists a certain angle of incidence at which the wave is completely transmitted into the glass, which is a typical feature of TM waves.

Figure 1.2 (b) shows the reflection coefficient when the light is incident from the glass side. In this case, propagating waves can have tangential wave vector components up to $2k_0$. Notice that the incident wave is completely reflected when $k_x > k_0$, a phenomenon that occurs when light is incident from a medium with a higher dielectric constant. As we will see in the following sections, this phenomenon plays an essential role in the excitation of surface plasmons.

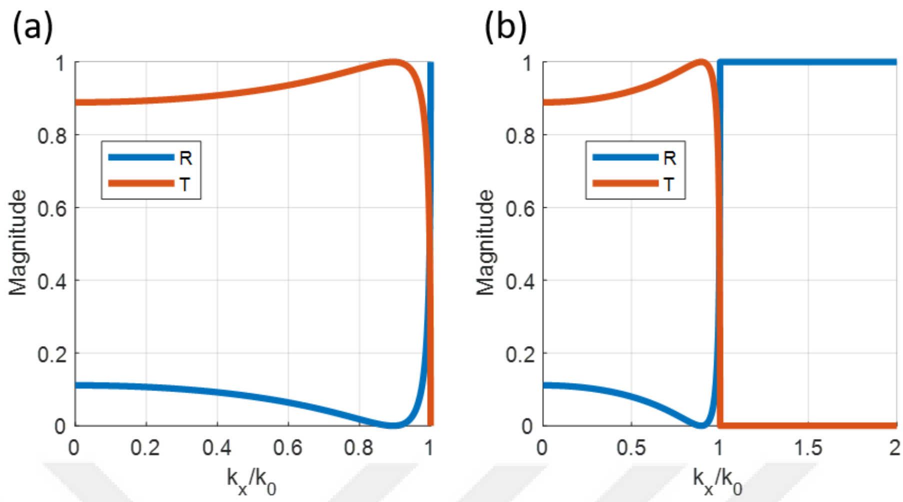


Figure 1.2: The Fresnel reflection and transmission coefficients for TM waves in two-layered media (see Figure 1.1) with (a) $\epsilon_1 = 1$, $\epsilon_2 = 4$ and (b) $\epsilon_1 = 4$, $\epsilon_2 = 1$.

## 1.2 Surface waves at an interface

In this section, we define the surface waves at an interface between two semi-infinite media. A surface wave is, by definition, bound to the surface and propagates along the surface. We leave how these surface waves may be excited to Section 1.5, however, once excited, we can assume that there are no incoming waves towards the interface, i.e. $H_1^+ = 0$ in Figure 1.1. The fields of the surface wave ($H_1^-$ and $H_2^+$), on the other hand, may extend into the media on either side of the interface as evanescent waves, or even leak in the form of propagating waves (see Figure 1.3).

Similar to our approach for calculating the Fresnel coefficients, we again start with the field expressions in both media.

$$\mathbf{H}_1 = \hat{\mathbf{y}} H_1^- e^{+jk_{z1}z} e^{-jk_x x} \tag{1.10}$$

$$\mathbf{H}_2 = \hat{\mathbf{y}} H_2^+ e^{-jk_{z2}z} e^{-jk_x x} \tag{1.11}$$

$$\mathbf{E}_1 = \left[ -\hat{\mathbf{x}} \frac{k_{z1}}{\omega \epsilon_1 \epsilon_0} - \hat{\mathbf{z}} \frac{k_x}{\omega \epsilon_1 \epsilon_0} \right] H_1^- e^{+jk_{z1}z} e^{-jk_x x} \tag{1.12}$$

$$\mathbf{E}_2 = \left[ \hat{\mathbf{x}} \frac{k_{z2}}{\omega \epsilon_2 \epsilon_0} - \hat{\mathbf{z}} \frac{k_x}{\omega \epsilon_2 \epsilon_0} \right] H_2^+ e^{-jk_{z2}z} e^{-jk_x x} \tag{1.13}$$

The first two equations (1.10) and (1.11) imply that $H_1^- = H_2^+$, and the continuity of

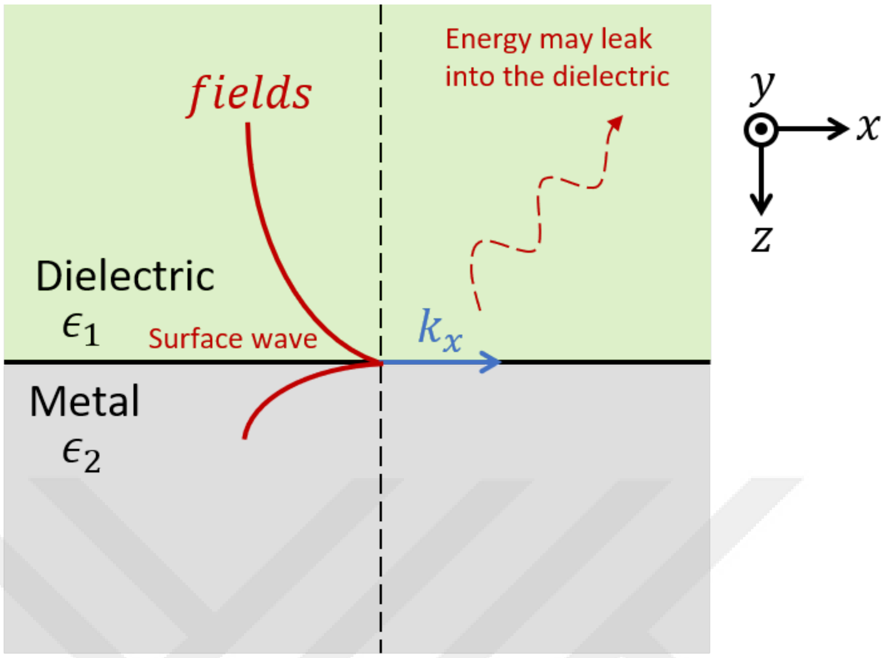


Figure 1.3: Depiction of a surface wave propagating at the interface between two dissimilar media. The surface wave is localized around the interface with decaying tails extending into the media. Depending on the composition of the layered media, a portion of the surface wave's energy may leak into the media. This leakage usually occurs in multi-layered media used in practical experimental configurations, as we will see in the next chapter.

the **x** component of the electric field, equations (1.12) and (1.13), gives the following condition.

$$\frac{k_{z1}}{\epsilon_1} + \frac{k_{z2}}{\epsilon_2} = 0 \tag{1.14}$$

Further simplifying this equation using $k_{zi} = \sqrt{\epsilon_i k_0^2 - k_x^2}$ and solving for the tangential component of the wave vector $k_x$, we get

$$k_x = k_0 \sqrt{\frac{\epsilon_1 \epsilon_2}{\epsilon_1 + \epsilon_2}} \tag{1.15}$$

where $k_0 = \omega / c$. The condition (1.15) we have just derived is the surface wave condition. Any surface at the interface between two semi-infinite media must satisfy this condition. This condition is also called the *dispersion relation*, describing the relationship between the frequency $\omega$ and the wave vector component $k_x$, since the frequency dependence of the materials are embedded into the relative permittivities

$\epsilon_1$ and $\epsilon_2$. We will investigate the dispersion relation for surface plasmons in more detail in Section 1.4.

Note that the results we just derived, especially the dispersion relation (1.15), are in no way specific to any material type, dielectric model, experimental configuration, or electromagnetic source. Even though the materials are labelled as *dielectric* and *metal* in Figures 1.1 and 1.3, we have not yet restricted our analysis to those materials. Moreover, we did not make any assumptions about the nature of the surface wave other than that it must be bound to the surface. Therefore, equation (1.15) describes any kind of surface wave, not only surface plasmons.

Before moving on to the details of the dispersion relation, there is one more key observation that we will rely on in the investigation of multi-layered structures. Rearranging equation (1.14) gives $\epsilon_2 k_{z1} + \epsilon_1 k_{z2} = 0$. This is indeed the denominator of the Fresnel reflection (1.8a) and transmission (1.8b) coefficients, which means that the reflection and the transmission coefficients blow up at the characteristic frequency and the wave vector values of surface waves. Although this might not look very meaningful at first sight, it actually provides us a powerful intuitive picture. In deriving the dispersion relation (1.15), we assumed there are no incoming waves ($H_1^+ = 0$), but there are outgoing waves ($H_1^- \neq 0$), so obviously the ratio of these two coefficients blows up. In other words, since a surface wave may be sustained without any input to the system, it intuitively makes sense that the amplitude of the surface wave diverges for any finite input. In conclusion, all of our observations nicely fit into a physical picture. We will later use this physical intuition and look for the poles of the reflection and/or transmission coefficients in order to identify the surface modes in more complex structures.

## *1.3 The Drude model for metals*

A surface plasmon is a type of electromagnetic wave that emerges due to the free electron density in metals or other materials with non-zero electric conductivity (e.g. doped semiconductors). However, we have yet to analyze the electromagnetic response of metals. In the previous section, we discussed the necessary conditions for a surface wave at the interface between two semi-infinite materials and arrived at equation (1.15) describing the relationship between the frequency, the wave vector and the relative permittivities. In this section, we will derive how metals behave under electromagnetic excitation, starting with the equation of motion for free electrons. After obtaining an expression for the relative permittivity for metals in frequency domain, we will calculate the surface plasmon dispersion relation and discuss its salient features in Section 1.4.

We assume that conductors contain a large number of free electrons, which are not bound to any of the atoms inside the material (that is why they are called *conductors* any way). These electrons can freely move in any direction inside the conductor in response to external forces. Figure 1.4 shows an illustration of this response, where an external electric is applied and free electrons move in the opposite direction of the external field. We can write the equation of motion for an electron

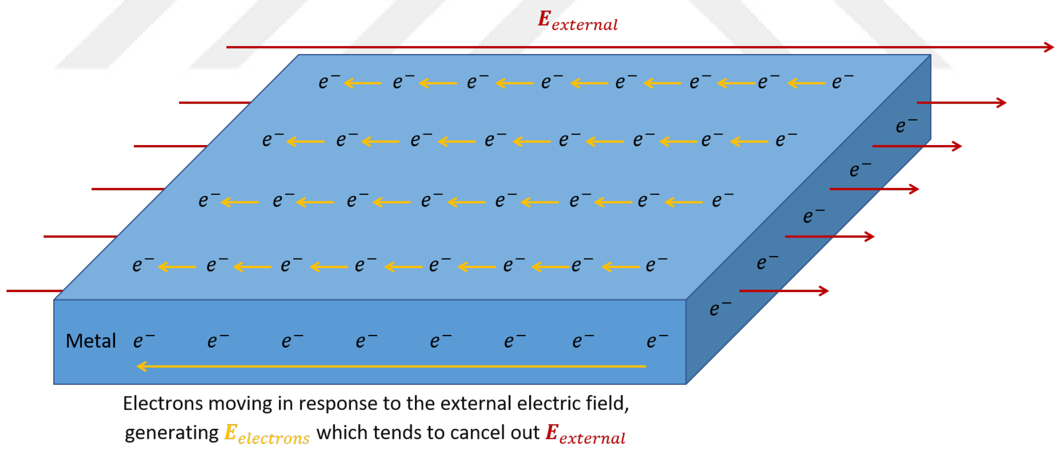


Figure 1.4: Free electrons in metal. An external electric field is applied to a metal. The electrons respond to the external field by moving in the opposite direction. The internal electric field generated by the electrons tends to cancel out the external field.

as follows.

$$m\ddot{x}(t) = -eE(t) - m\gamma\dot{x}(t) - m\omega_0^2 x(t) \tag{1.16}$$

where $x$ is the position, $m$ is the mass and $-e$ is the charge of the electron, single and double dots indicate the first and the second order derivatives with respect to time

$t$, respectively. The left-hand side represents the total force acting on the electron. The first term on the right-hand side is the force exerted on the electron by the external field. The second term is the dissipation acting in the opposite direction to the motion of electrons. This is represented by the dissipation constant $\gamma$, which is a phenomenological term accounting for all types of losses in the system. The last term would be the restoring force for particles bound to a stationary center (e.g. harmonic oscillator); however, since we are considering free electrons this term is zero ($\omega_0 = 0$).

We can apply the Fourier transform to equation (1.16) to get an expression in the frequency domain. Rearranging the terms to get an expression for the position $X(\omega)$,

$$X(\omega) = \frac{-e/m}{-j\omega^2 + j\omega\gamma} E(s) \tag{1.17}$$

The polarization density ($\mathbf{D}(w) = \epsilon_0 \mathbf{E}(w) + \mathbf{P}(w)$) can be defined as $P(\omega) = -neX(\omega)$ using the displacement equation (1.17), where $n$ is the electron density in the metal. Note that the electron density $n$ depends on the material's intrinsic properties, the larger it is the higher the conductivity. Using the constitutive relation (1.2a), we can write down the final expression for the relative permittivity, i.e. the response of the medium, as in equation (1.18).

$$\epsilon(w) = 1 - \frac{\omega_p^2}{\omega^2 - j\gamma\omega} \tag{1.18}$$

where $\omega_p^2 = \frac{ne^2}{m\epsilon_0}$ is defined as the plasma frequency. As we will see later, the plasma frequency is larger than any practical frequency value $\omega$.

Equation (1.18) is called the Drude permittivity model which describes the response of metals to electromagnetic waves. There are several features of the Drude model that deserves our attention:

- Permittivity at any frequency is complex-valued, implying that there is always some attenuation in the system. This is imposed by non-zero $\gamma$. There is no value in investigating the hypothetical and unrealistic lossless case with $\gamma = 0$, since this can lead to misinterpretation of results, or incorrect physical intuition may be prematurely formed based on results that cannot be generalized to lossy materials.

- At low frequencies, the permittivity is very large with a negative real part. At such frequencies, the material will be highly reflective and will not cause much power dissipation.

- At very high frequencies, the permittivity asymptotically approaches to the permittivity of free space due to quadratically increasing denominator in (1.18). In practice, these frequencies are not of any concern since the Drude model loses its validity long before those frequencies are reached, as shown in Figure 1.5.

- Depending on the material being modelled, the Drude model can be augmented with additional parameters taking into account the restoring force ($\omega_0 \neq 0$), which is not negligible at visible frequencies, or the background permittivity, i.e. the permittivity as $\omega$ approaches infinity.

Next, we look at how well the model represents a real metal by fitting the Drude parameters to the experimental data for gold [21]. A non-linear least squares fit is made to the experimental data for wavelengths between $12.5\mu m$ and $0.5\mu m$ using the Drude model to find that $\omega_p = 1.30 \times 10^{16}\ rad/s$ and $\gamma = 3.27 \times 10^{13}\ rad/s$. Figure 1.5 shows the experimental permittivity measurements for gold and a non-linear least squares fit to the experimental data using the Drude model. The main figure clearly shows that the model agrees with the experimental data at a wide range of frequencies from $12.5\mu m$ down to visible wavelengths. However, the inset shows that the model breaks down around $0.5\mu m$, after which a trend change in permittivity is observed due to interband transitions. This change is the main reason why the experimental data for wavelengths smaller than $0.5\mu m$ was not used in the fitting. It is also important to note that towards the high frequencies (see the inset in Figure 1.5) the model underrepresents the losses (the imaginary part) and exaggerates the real part of the permittivity.

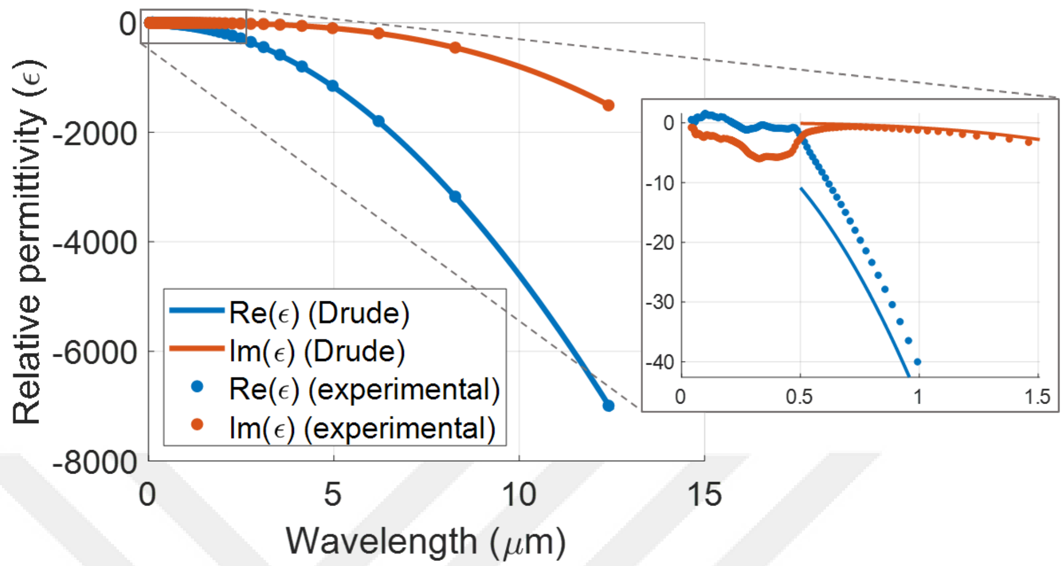


Figure 1.5: Drude model for Gold. The experimental data for gold is fitted to the Drude model in equation (1.18). The real and imaginary parts of the dielectric function are shown in blue and red, respectively. Dots show the experimental data while the curves show the fitted Drude model. The inset shows the values at small wavelengths. It is seen that the Drude model fails to correctly represent the metal at low wavelengths.

The reflection spectrum of a metal is significantly different from a dielectric (e.g. see Section 1.1.1). To see this difference, consider the case where the medium of incidence is a dielectric with $\epsilon = 4$ and the transmission medium is either vacuum ($\epsilon = 1$) or the gold used in Figure 1.5. The reflection spectrum is shown in Figure 1.6. Notice that the reflection is very close to unity and insensitive to the angle of incidence. There is also no total internal reflection, unlike reflection between two dielectrics.

The waves transmitted into the metal are eventually absorbed by the medium as they propagate through the metal layer. Unlike in the dielectric case where the transmitted waves travel without any attenuation, these transmitted waves are completely lost, so we do not show them as *transmitted* in Figure 1.6. However, as we will see in Chapter 2, if the thickness of the metal layer is finite, the waves can emerge from the other side of the metal with significant field amplitudes.

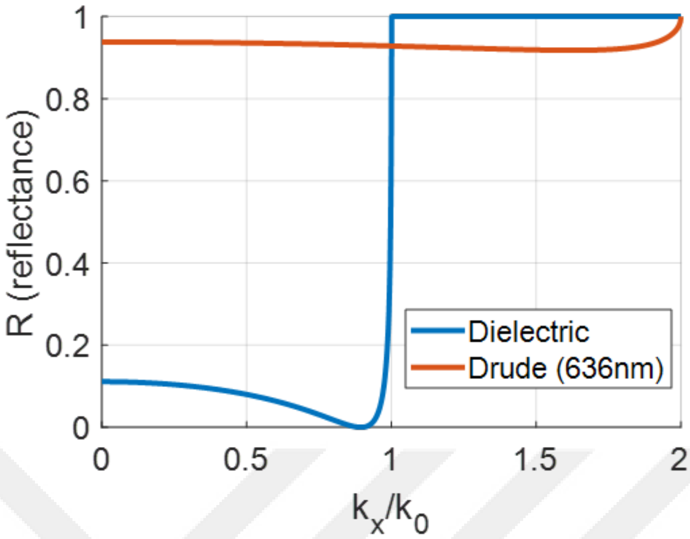


Figure 1.6: Reflections from a Drude metal and a low permittivity material. The red curve shows the reflection between glass ($\epsilon_{glass} = 4$) and a drude metal. The reflection is close to unity and insensitive to the angle of incidence. The blue curve shows the reflection between glass and air ($\epsilon_{air} = 1$). The reflection is strongly dependent on the angle of incidence and total internal reflection is observed for $k_x > k_0$. These two reflection examples play an important role in the excitation of surface plasmons in thin metal films.

Various modifications of the Drude model exist. A modification that will be useful to us is the one in equation (1.19), where $\epsilon_\infty$ replaces the free space .

$$\epsilon(w) = \epsilon_\infty - \frac{\omega_p^2}{\omega^2 - j\gamma\omega} \tag{1.19}$$

Let us also put a reminder here that we will revisit the Drude model in Chapter 3, where we will analyze response of metals to more complex excitations.

### *1.4 SPP dispersion relation at a dielectric-metal interface*

We finally combine the results from Sections 1.2 and 1.3 to obtain the dispersion for surface plasmon waves at an interface between a dielectric and a metal. We start with the dispersion relation (1.15)

$$k_x = k_0\sqrt{\frac{\epsilon_1\epsilon_2}{\epsilon_1 + \epsilon_2}} = k_1\sqrt{\frac{\epsilon_2}{\epsilon_1 + \epsilon_2}}$$

where the medium of incidence $\epsilon_1$ is a dielectric, $\epsilon_2$ is metal, and $k_1$ is the wave number in the dielectric. We have seen in the previous section that metals have permittivities with a negative real part, i.e. $\epsilon_2' < -1$, where single and double primes denote the real and imaginary parts, respectively. This implies that the square root in the dispersion relation is larger than one, and therefore, tangential wave vector component $k_x$ is larger than the wave number in the dielectric. In turn, the normal wave vector components become imaginary, making the fields decay away from the interface. All of these qualitative observations are in accordance with the assumptions we made in Section 1.2.

Next, we substitute the Drude model 1.18 for $\epsilon_2$ in the dispersion relation and plot the tangential wave vector $k_x$ as a function of frequency, as shown in Figure 1.7. We use vacuum for the dielectric region. The dispersion curve in Figure 1.7 is a textbook example of a dispersion relation using a lossy Drude model. At low frequencies, the surface plasmon modes start very close to but beyond the lightline. The wave vector grows dramatically as frequency increases until the back-bending point. Near the back-bending region, the tangential wave vector is very large, implying that the fields are very tightly confined to the interface (i.e. the fields decay extremely fast away in the normal direction to the interface). One issue though is that the imaginary part of $k_x$ also grows towards the back-bending point and therefore these SPP modes cannot propagate much further. In the region above the back-bending, the wave vector becomes smaller than the vacuum wavelength and the wave is no longer confined to the interface.

Next, we look at more realistic scenarios using real metal permittivity values for aluminum, gold, silver and copper [21, 22]. Figure 1.8 shows the dispersion curves for all of these metals. It is clearly seen that all of our observations originating from the Drude model hold. However, also notice in the dispersion curve for gold that the increase in the wave vector towards the back-bending region is much smaller compared to the Drude model. This is because the Drude model already starts to deviate from the true experimental values. Therefore, the confinement and field enhancement features of SPPs will be less dramatic in practice than the predictions

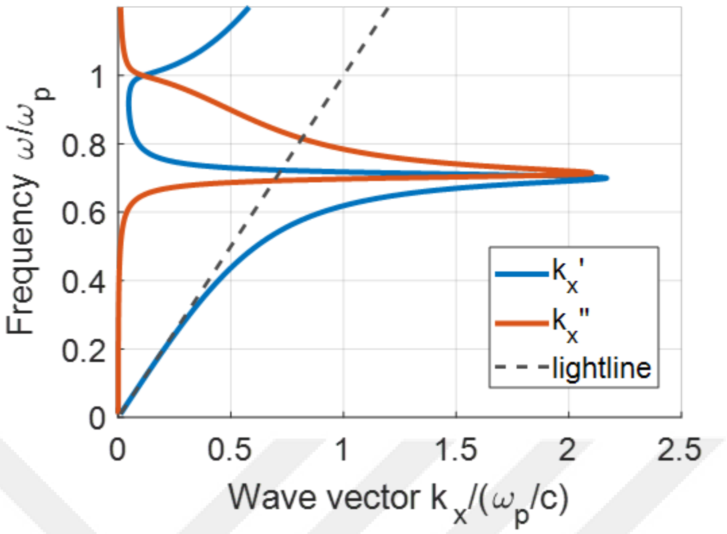


Figure 1.7: Surface plasmon dispersion at a single interface between a dielectric and a Drude metal. The dielectric region is taken to be vacuum with $\epsilon_1 = 1$. The Drude model uses the parameters calculated for gold in Section 1.3. The real and the imaginary parts of the tangential wave vector component are shown in blue and red, respectively.

of the Drude model.

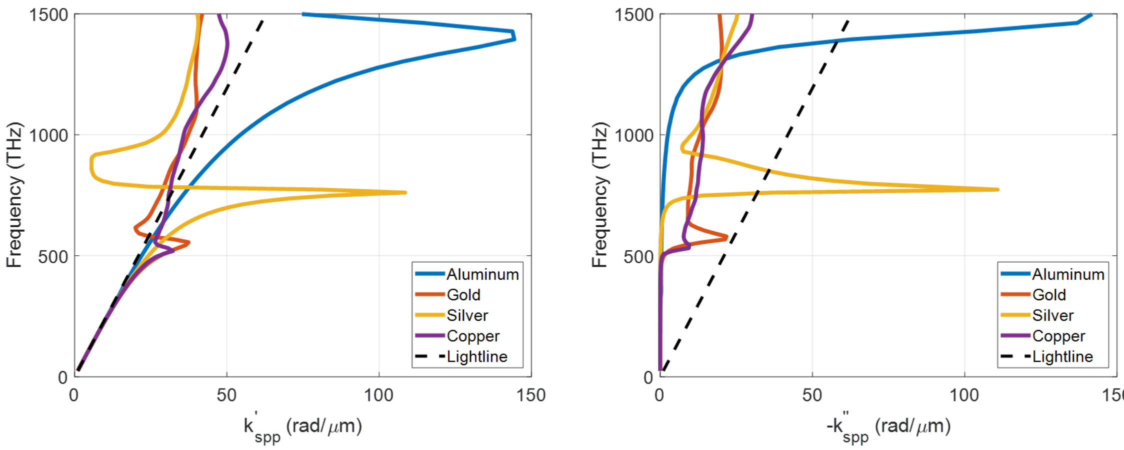


Figure 1.8: Surface plasmon dispersion at a single interface between a dielectric and various metals. The dielectric region is taken to be a glass material with $\epsilon_1 = 4$. The real and the imaginary parts of the tangential wave vector component are shown in blue and red, respectively.

## 1.5 Experimental configurations to excite SPPs

### 1.5.1 Kretschmann-Raether configuration

The Kretschmann-Raether configuration (KRC) is a very common experimental setup used to excite SPPs at metal surfaces [23]. An illustration is shown in Figure 1.9. The KRC consists of three layers: A thin metal film, a glass prism that is placed on top of a thing metal film, and air on the other side of the metal film. Air can be another dielectric material whose permittivity is lower than the glass prism. The structure is illuminated from within the glass prism. As we have seen in Figures 1.7 and 1.8, the SPP has a tangential wave vector that is outside the light cone of air. Illuminating the structure from the glass side provides the means to generate a plane wave with a large enough wave number required to excite SPPs. The three-layered KRC will further be scrutinized in later chapters as it constitutes a basic model whose results can be generalized to more complicated plasmonic structures.

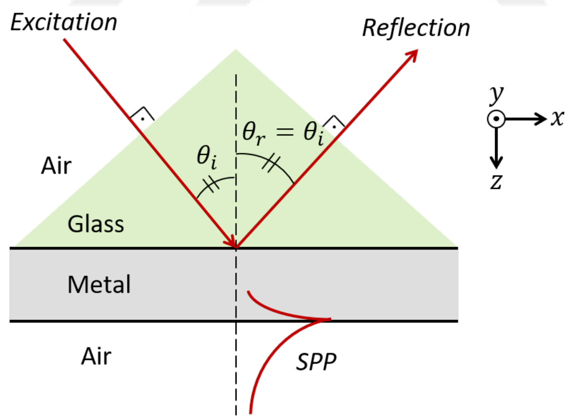


Figure 1.9: The Kretschmann-Raether configuration (KRC). The basic KRC consists of three layers: glass-metal-air. A large tangential wave vector component outside the light cone of air can be generated in the glass medium with higher dielectric constant. The resultant wave can penetrate the metal film and couple to the SPP at the metal-air interface.

### *1.5.2 Otto configuration*

The Otto configuration is very similar to the KRC [24]. It contains the same glass prism which is used to illuminate the structure. The glass prism is suspended on top of a thick metal block (a semi-infinite medium in theoretical considerations). Usually, a dielectric with a permittivity smaller than that of glass is used as a spacer between the metal and the glass prism. The wave incident on the glass-air interface becomes evanescent in the air because the tangential component of its wave vector is larger than the free space wave number. This tail of this evanescent wave couples to the air-metal interface on the other side of the gap, exciting an SPP mode.

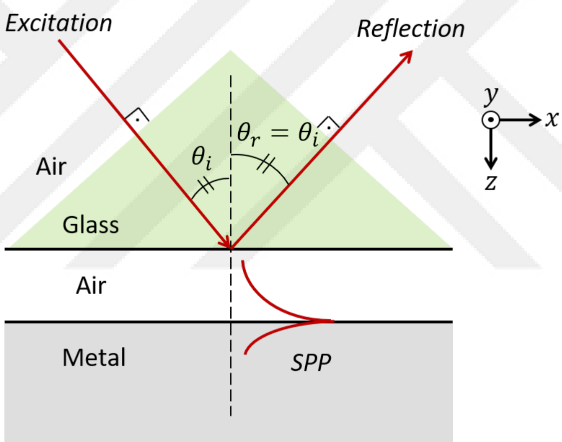


Figure 1.10: The Otto configuration. This configuration is very similar to the KRC (see Figure 1.9) and consists of glass-air-metal layers. A propagating wave in the glass prism with a tangential wave vector outside the light cone of air can evanescently penetrate the air gap and couple to the air-metal interface to excite SPPs.

### *1.5.3 Grating coupler*

Another method to excite an SPP is to use a grating coupler on the surface of a metal to generate a range of large tangential wave vector components, one of which matches the wave vector of the SPP and excites the SPP [25]. The range of wave vectors generated by a periodic diffraction grating, as shown in Figure 1.11, is given by the following equation [26].

$$k_x^{scattered} = k_x^{incident} + \frac{2\pi}{a}n \tag{1.20}$$

where $a$ is the period of the grating structure and $n$ is the order of diffraction (see Figure 1.11). In other words, the grating adds/subtracts a multiple of $2\pi/a$ to the tangential wave vector component of the incident wave. Designed properly, one of these diffraction orders will match the wave vector $k_{spp}$ of the SPP modes supported at the air-metal interface, and, as a result, an SPP mode will be excited. It has been shown that plasmonic structures using a grating coupler are less sensitive to frequency changes than dielectric prism based coupler such as the KRC and Otto configuration, while they have similar sensitivity with respect to the angle of incidence [27]. Note that, even though the period of the grating is the determining factor on whether an SPP can be excited or not, other design parameters such as grating depth, groove shape, fill-ratio are shown to play an important role in controlling the efficiency of grating couplers [28].

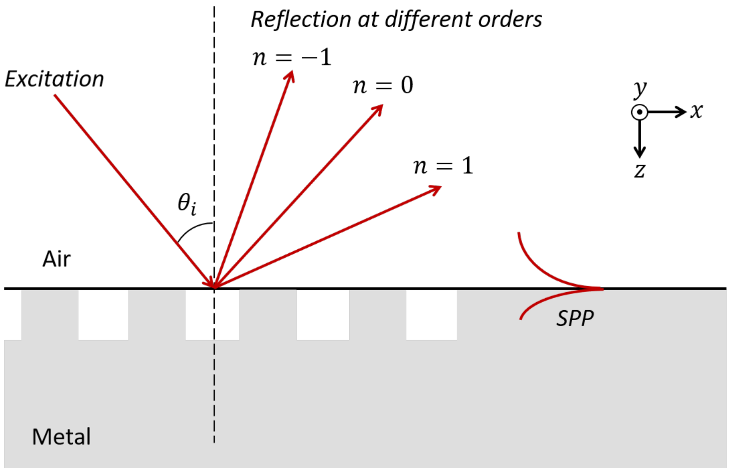


Figure 1.11: Grating coupler. A wave incident on the grating structure is scattered into discrete orders of diffraction as shown by the red arrows marked with orders $n$. The tangential wave vector components of the scattered waves can be calculated via equation (1.20). One of the scattering orders with a matching wave vector to the SPP's wave vector can excite the SPP at the air-metal interface.

### *1.5.4 Structural discontinuity*

Another method of SPP excitation is using a structural discontinuity that is illuminated by a propagating wave. An example of such a structural discontinuity is the nano slit shown in Figure 1.12. When illuminated by an incident wave, the nano slit acts as a point source that generates a continuum of waves with a wide spectrum of wave vectors [29]. One of the wave vector components from this spectrum matches the SPP wave vector at the air-metal interface as defined by equation (1.15) and excites the SPP. Unlike the grating coupler which generates only a discrete number of wave vectors, a discontinuity is less selective and creates a continuous range of wave vectors in the spectral domain.

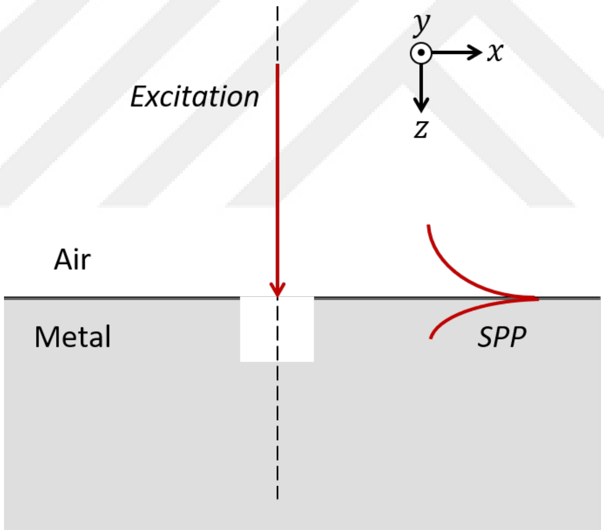


Figure 1.12: Structural discontinuity. When illuminated by a light source, a structural discontinuity such as a nano slit generates waves with a wide spectrum of wave vector components. An SPP can be excited if the wave vector of the SPP falls inside the k-spectrum generated by the discontinuity.

### *1.5.5 Vertical electron beam*

All of the methods discussed in the previous sections involved an optical excitation of the plasmonic structure to generate SPP waves. Another commonly used technique is to use an electron beam instead. One of the first experimental studies indeed used electron beams to excite SPPs on metal films and observed signature of SPP excitation in the energy loss or the diffraction spectrum [30, 31, 32]. One of the main advantages of these electron beam techniques is that they do not require a coupling prism or a grating structure. Highly energetic electrons can easily penetrate the metal film and excite SPPs in the process.

There are mainly two types of electron beam excitation methods: Vertical and horizontal beams. The vertical electron beam is illustrated in Figure 1.13. In this configuration, electrons, which are normally incident on the metal's surface, penetrate the metal film and scatter before they exit from the other side. Due to the conversation of momentum, when an electron leaves the metal film with a non-zero horizontal momentum, an SPP wave is generated in the opposite direction with a matching horizontal wave vector [33].

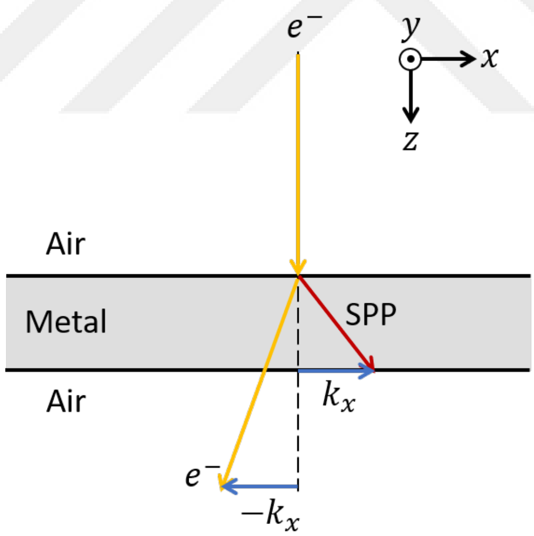


Figure 1.13: Vertical electron beam method. An electron beam is normally incident on the metal film. Conservation of momentum dictates that electrons scattering in the horizontal direction generate SPP waves in the opposite direction.

### *1.5.6 Horizontal electron beam*

The other type of electron beam excitation is the horizontal beam shown in Figure 1.14. In this scenario, the velocity of the electrons in the electron beam dictate the velocity, i.e. the $\omega/k_x$ ratio, of the induced surface wave at the air-metal interface [33, 34]. Such an electron beam can excite SPP at the point where the $u_0 = \omega/k_x$ line intersects with the SPP dispersion curve in Figure 1.7 or 1.8.

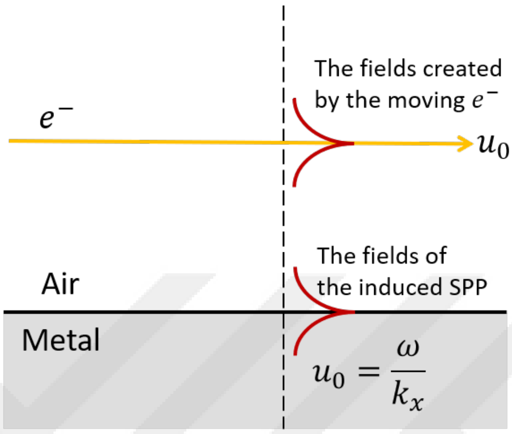


Figure 1.14: Horizontal electron beam method. An electron beam is parallel to a metal film inducing charge oscillations near the surface of the metal. The velocity of the electrons dictate a constant value for the frequency to wave vector ratio $\omega/k_x$. An SPP is excited at a point on the air-metal SPP dispersion curve, which satisfies this frequency to wave vector ratio.

### *1.5.7 Other advanced methods*

There are also other more advanced methods of exciting SPPs such as using metamaterials [35] and metasurfaces [36, 37]. The main purpose of these more advanced methods is to be able to increase the excitation-to-SPP conversion efficiency and fine tune the properties of the generated SPPs. Such methods are not the subject matter of this thesis.

Chapter 2

# COMPLETE DESCRIPTION OF SURFACE PLASMONS POLARITONS

## 2.1 Introduction

This chapter is dedicated to providing a complete description of SPPs in plasmonic structures. We investigate the nature of SPP modes in layered media and discuss how they manifest themselves in experimental configurations. In the previous chapter, we established an intuition that the electromagnetic modes of a structure can be determined by finding the poles of the Fresnel reflection or transmission coefficient. This can be extended to multi-layered structures and will form the basis of our modal analysis. This is actually a very common approach in the study of electromagnetic modes. As the transfer function, i.e. the electromagnetic response of these layered plasmonic structures, is indeed a multi-valued function, we investigate all Riemann sheets and show the importance of all modes on these Riemann sheets. We identify all extrema of the generalized reflection and transmission coefficients, interpret their field and power profiles in detail and discuss their connection to experimental observations. The novelty of this chapter lies in the detailed analysis the extrema on these Riemann sheets. We identify previously undocumented features which are useful in understanding how SPP modes depend on frequency, wave vector and other structural parameters. The salient features of SPPs such as local field enhancement and extinction of the incident wave are shown to be related to, not only the pole commonly associated with the SPP mode, but also several other poles and zeros on the complex wave vector domain. Furthermore, we provide a direct correspondence between experiments and theoretical calculations, which seems to be missing in the current literature.

One of the problems we aim to settle in this chapter is that, when it comes to finding SPP modes in plasmonic structures, there is an apparent disagreement (or confusion) in the scientific community as evidenced by the conflicting results of various studies. In order to find the angle of incidence $\theta$ and the frequency $\omega$ at which the excitation source best couples to the SPPs, one usually measures the reflectance $|\tilde{r}|^2$: A minimum in the reflectance is associated with the maximum coupling to an SPP mode because the energy is expended to excite the SPP mode and does not return back to the source medium. This maximum coupling point is also where the highest field enhancement is expected. Although this interpretation has been extensively used to find the SPP modes in layered media such as the Kretschmann-Raether configuration (KRC), several recent studies claimed that the minimum in the reflectance did not indeed correspond to the SPP excitation and that the conventional use of the KRC failed to efficiently couple propagating plane waves to SPPs [38, 39, 40]. The interpretations of the reflectivity minimum in these studies are different; it was attributed to the increased absorption within the metal [38], or to the "Brewster angle" [39], or to a new electromagnetic mode (referred to as *perfectly absorbing mode*) [40]. It has been even claimed that the Fresnel coefficients are incapable of expressing the effects of SPP modes [38]. Indeed, similar observations were reported decades ago [41, 42], where a difference between the angles of incidence corresponding to the reflectance minimum and to the enhancement of the electric field at the metal-air interface was recorded. The results presented in this chapter will clarify the issues around these discussions and provide a definitive answer as to the nature of SPP modes and related phenomena.

Enabled by the aforementioned analysis, an SPP mode's dependence on experimental design parameters will be discussed, and as a result, various optimization approaches for different SPP features such field enhancement and absorption will be presented. Since the study of SPP dispersion in plasmonic waveguides, which is the subject matter of the next chapter (Chapter 3), is mainly based on the information of zeros and poles of transfer functions, i.e., the generalized reflection and transmission coefficients, this chapter will prove invaluable in understanding the characteristics of the electromagnetic response of plasmonic systems.

## 2.2 Fields in multi-layered media

In this section, we comprehensively study plane electromagnetic waves in layered media, their field distribution and power flow. We carefully investigate the electromagnetic modes supported by multi-layered structures and describe the properties of the modes on different regions of the Riemann sheet (note that "multi-layered media", "layered media", "stratified media" are used interchangeably; they have the same meaning for the purposes of this thesis). We establish a mathematical relationship between the proper and improper Riemann sheets, which, in turns, provides an intuitive correspondence between the theoretical results and the experimental configurations used to excite SPPs.

### *2.2.1 Generalized reflection and transmission coefficients*

The Fresnel reflection and transmission coefficients (1.8a) and (1.8b) derived in Chapter 1 describe how a uniform plane wave is reflected/transmitted at a single interface between two media. However, when there are multiple layers as in Figure 2.1, the waves will get reflected infinitely many times as they propagate inside the intermediate layers, leaking a portion of their energy to the outermost layers with each reflection. This process is visualized in Figure 2.1 with diminishing arrow lengths. Note that, in reality, the incident plane wave covers the entire upper medium; only a small portion is shown here. Due to the electromagnetic boundary conditions, the tangential component of the wave vector $k_x$ is conserved in all layers, and therefore, the system has translational symmetry in the lateral direction (the $\mathbf{x}$ direction). As a result, all reflected fields at a single point on the interface ($z = 0$) can be summed up to obtain the generalized reflection coefficient. The same procedure can be used on the bottom interface ($z = d$) to obtain the generalized transmission coefficient.

It is also important to realize that, in steady-state, all fields in the middle layer can be represented as two plane waves, each propagating in opposite vertical ($\mathbf{z}$) directions, as shown in Figure 2.2. This steady-state picture can also be used directly

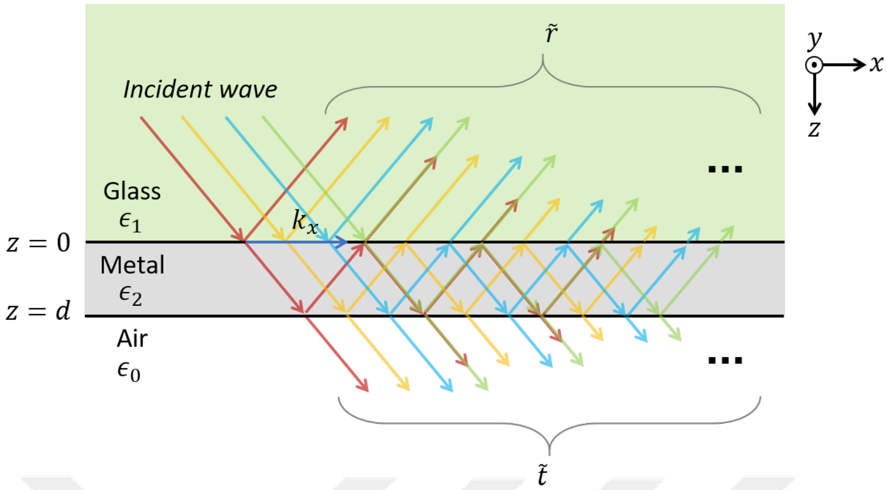


Figure 2.1: Illustrative ray picture in layered media. Different light rays and their interaction with the media intuitively show how steady-state fields are formed as a result of infinitely many reflections from the layered media.

to calculate the generalized reflection and transmission coefficients by matching the fields at the boundaries (this is called the transfer matrix method).

In general, fields for TM waves in any layer $m$ can be written as

$$\mathbf{H}_m = \hat{\mathbf{y}}(H_m^+ e^{-jk_{zm}z} + H_m^- e^{+jk_{zm}z})e^{-jk_x x} \tag{2.1}$$

$$\begin{aligned}\mathbf{E}_m = {} & \hat{\mathbf{x}}\frac{k_{zm}}{\omega\epsilon_m\epsilon_0}(H_m^+ e^{-jk_{zm}z} - H_m^- e^{+jk_{zm}z})e^{-jk_x x} \\ & - \hat{\mathbf{z}}\frac{k_x}{\omega\epsilon_m\epsilon_0}(H_m^+ e^{-jk_{zm}z} + H_m^- e^{+jk_{zm}z})e^{-jk_x x}\end{aligned} \tag{2.2}$$

where the magnetic field $\mathbf{H}_m$ is used in Ampere's law (1.1d) to obtain the electric field. Imposing the boundary conditions at the first interface for the magnetic field and the tangential component of the electric field, we get

$$H_1^+ + H_1^- = H_2^+ e^{jk_{z2}d} + H_2^- e^{-jk_{z2}d} \tag{2.3}$$

$$\frac{k_{z1}}{\omega\epsilon_1}(H_1^+ - H_1^-) = \frac{k_{z2}}{\omega\epsilon_2}(H_2^+ e^{jk_{z2}d} - H_2^- e^{-jk_{z2}d}) \tag{2.4}$$

Substituting $r_2 H_2^+$ for $H_2^-$ and eliminating $H_2^+$, we obtain the generalized reflection coefficient

$$\tilde{r} = \frac{H_1^-}{H_1^+} = \frac{r_1 + r_2 e^{-jk_{z2}2d}}{1 + r_1 r_2 e^{-jk_{z2}2d}} \tag{2.5}$$

where $r_1$ and $r_2$ are the Fresnel reflection coefficients at the first and the second interfaces, respectively, as defined in equation (1.8a). Furthermore, using $H_3^+ = H_2^+ + H_2^-$, we obtain the generalized transmission coefficient.

$$\tilde{t} = \frac{H_3^+}{H_1^+} = \frac{(1 + r_1 + r_2 + r_1 r_2)e^{-jk_{z2}d}}{1 + r_1 r_2 e^{-jk_{z2}2d}} \tag{2.6}$$

The generalized reflection and transmission coefficients representing the steady-state fields in layered-media are schematically shown in Figure 2.2.

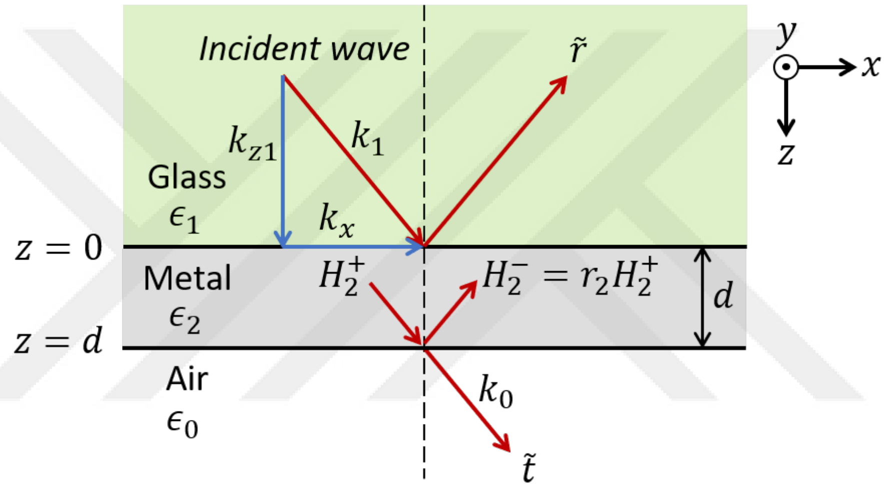


Figure 2.2: The steady-state TM fields in three-layered media: Dielectric-Metal-Air configuration. Red arrows show the direction of the plane waves, i.e. the wave vectors. $\tilde{r}$ and $\tilde{t}$ represent the generalized reflection and transmission coefficients, respectively.

Before analyzing these expressions in detail, we extend them to also represent the generalized reflection and transmission coefficients in structures with any number of layers, as seen in Figure 2.3. In this case, the reflections from all layers below the incidence medium will contribute to the generalized reflection coefficient $\tilde{r}$. However, instead of trying to derive $\tilde{r}$ by accounting for all the reflections, we can start from the bottom layer to iteratively work our way up to the first layer, noting that there is no incident wave (travelling in $-\mathbf{z}$ direction) in the bottom medium. The reflection in the $(n-1)^{th}$ layer (the layers are numbered with respect to their permittivity index) is always given by the Fresnel equation (1.8a). Then, for layer $n-2$, we can use the generalized reflection coefficient in equation (2.5) to calculate the reflection from the layers below $n-2$. Finally, we repeat the same procedure for each layer by replacing $r_2$ in (2.5) with the generalized reflection coefficient from the layer immediately below the current layer. In summary, substituting $\tilde{r}_2$ (see Figure 2.3) for $r_2$ in equation (2.5) will be sufficient to obtain the generalized reflection coefficient in the medium of incidence (the first layer).

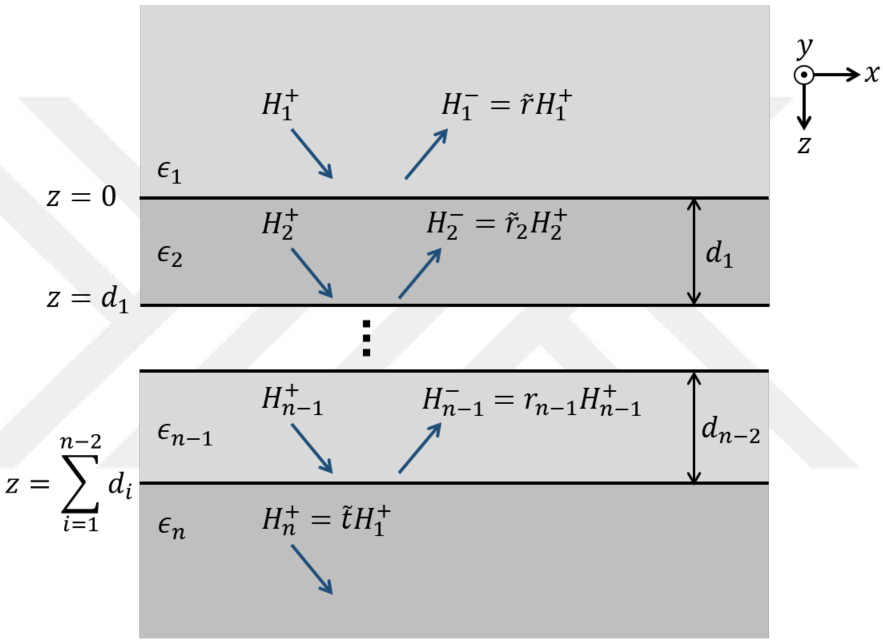


Figure 2.3: The steady-state TM fields in multi-layered media. The fields amplitudes are defined at the bottom interface of each layer except for the last/transmission layer, which is defined at $d = d_i$ (i.e. the top interface of the last layer).

We used our intuition to show that equation (2.5) holds for all layered structures with a small substitution. Nevertheless, several different ways of deriving the generalized reflection and transmission coefficients (some more algebraic than others) can be found in these references [43, 16, 44, 45].

### *2.2.2 The Poynting vector*

Next, we derive the expression for the power flow, i.e. the Poynting vector, for the fields in layered-media shown in Figures 2.3. These expressions will prove invaluable for figuring out where the energy of an SPP goes and what kind of experimental conditions are required to sustain an SPP.

Let us split the real and imaginary parts of the wave vector as follows.

$$
\begin{aligned}
k_x &= k'_x + jk''_x \\
k_z &= k'_z + jk''_z
\end{aligned}
$$

Single and double primes denote the real and imaginary parts, respectively. The same notation is used throughout this thesis for all variables and parameters (e.g. $\omega$, $\epsilon$).

The time-averaged Poynting vector is defined as $\langle \mathbf{S} \rangle = \frac{1}{2} Re(\mathbf{E} \times \mathbf{H}^*)$ [44]. For TM waves, the stationary electric and magnetic fields in any layer $m$ of a stratified medium are defined in equations (2.1) and (2.2) (using the $e^{j\omega t}$ convention). Using these expressions, the Poynting vector can be calculated as

$$
\begin{aligned}
\langle \mathbf{S}_m \rangle = \frac{1}{2} Re \Bigg\{ & \hat{\mathbf{x}} \frac{k_x}{\omega \epsilon_m \epsilon_0} e^{-2k''_x x} \Big[ |H_m^+|^2 e^{-2k''_{zm} z} + |H_m^-|^2 e^{+2k''_{zm} z} \\
& \qquad H_m^+ H_m^{-*} e^{-j2k'_{zm} z} + H_m^- H_m^{+*} e^{+j2k'_{zm} z} \Big] \\
& + \hat{\mathbf{z}} \frac{k_{zm}}{\omega \epsilon_m \epsilon_0} e^{-2k''_x x} \Big[ |H_m^+|^2 e^{-2k''_{zm} z} - |H_m^-|^2 e^{+2k''_{zm} z} \\
& \qquad + H_m^+ H_m^{-*} e^{-j2k'_{zm} z} - H_m^- H_m^{+*} e^{+j2k'_{zm} z} \Big] \Bigg\}
\end{aligned} \tag{2.7}
$$

The field amplitudes for waves moving in positive and negative $z$ directions are indicated with the superscripts as defined in Figure 2.3. When one is solving for the natural electromagnetic modes supported by the layered medium, this lengthy expression is greatly simplified in the incidence (the first) and the transmission (the last) layers because the field amplitudes $H_1^+$ and $H_n^-$ are set to zero. Assuming the incidence and transmission layers are lossless, which is almost always the case for any realistic scenario, we get

$$
\langle \mathbf{S}_1 \rangle = (\hat{\mathbf{x}} k'_x - \hat{\mathbf{z}} k'_{z1}) \, e^{2k''_x x - 2k''_{z1} z} \frac{|H_1^-|^2}{\omega \epsilon_1 \epsilon_0} \tag{2.8}
$$

$$
\langle \mathbf{S}_n \rangle = (\hat{\mathbf{x}} k'_x + \hat{\mathbf{z}} k'_{zn}) \, e^{2k''_x x + 2k''_{zn} z} \frac{|H_n^+|^2}{\omega \epsilon_n \epsilon_0} \tag{2.9}
$$

Notice that the direction of the Poynting vector is determined by the signs of the *real parts* of the wave vectors $k_x$ and $k_z$. This is the direction of the power flow: in other words, where the electromagnetic energy is moving towards. On the other hand, the direction of the *decay* of the power flow is given by the signs of the imaginary parts of the wave vectors. This shows where the power flow is smaller. These two directions, namely the directions of power flow and power decay, are not necessarily the same. Our intuition on plane waves travelling in uniform and lossy medium might rightfully say that the wave will surely decay in the direction of propagation (or power flow). However, SPPs are surface modes that exist only when certain materials with contrasting permittivities (metals and dielectrics) come together. Therefore, their properties are slightly different, as we will discover in the following sections.

## 2.3 The nature of surface plasmons

In this section, we investigate in detail the nature of SPP modes in layered media. We will specifically focus on passive material configurations that exclusively support SPPs with other lossy modes spectrally located far away from the SPP modes. The simplest of those structures are the three-layered media that contain either one (dielectric-metal-dielectric) or two layers (metal-dielectric-metal) of metals, both of which will be studied in this section.

In Chapter 1 and the previous section, the definition $k_z = \sqrt{\epsilon k_0^2 - k_x^2}$ was used without much a posteriori thought. The square root produces one positive and one negative solution, and it is usually expected that one will be able to easily discern the unphysical solution from the imaginary part of the wave vector $k_z$: If the imaginary part is positive (remember that a plane wave travelling in $+z$ direction is represented with $e^{j\omega t - j\mathbf{kr}}$), then this is an unphysical solution because the wave is growing in the propagation direction. This *recipe* (yes, a recipe - after all, this is based on intuition and not physical facts) is misleading as it only applies to a few special cases and ignores the plethora of electromagnetic modes that influence the outcome of theoretical predictions and experiments.

Therefore, the simple equation $k_z = \sqrt{\epsilon k_0^2 - k_x^2}$ will be placed under scrutiny. This will lead to an investigation of all possible modes on all Riemann sheets, *proper* or *improper*. We will see that even improper modes significantly affect the observations in the proper domain. We refrain from labelling electromagnetic modes as physical or unphysical and instead use proper or improper because the word "unphysical" gives the wrong impression of being irrelevant to real experiments while the truth is contrary.

A direct mapping between certain paths on the Riemann sheets and experimental configurations will also be derived. This connection, which is currently missing in the current literature, provides an insight into how experimental results should be interpreted and compared with theoretical calculations.

Finally, it should be noted that the analyses and most conclusions in this Section apply to any layered media with any types of electromagnetic mode.

### *2.3.1 Branch cuts and Riemann sheets*

In the evaluation of the normal component of the wave vector in $k_z = \sqrt{\epsilon k_0^2 - k_x^2}$, there are two possible solutions $\pm k_z$. As we will see later, both of these solutions play important roles in the reflection and transmission spectra of configurations that support SPP modes (see Section 1.5 for multiple examples). We are particularly interested in the solutions for the wave vector $k_{z1}$ in the medium of incidence. In the theoretical calculation of the SPP modes, it is assumed that there are no incident waves. However, in practical configurations such as the KRC, an incident wave is needed to excite the SPP. As a result, there are both incoming and outgoing waves in the medium of incidence, which is the main physical reason why both proper and improper modes need to be taken into account in describing the SPP mode.

We define the $+k_z$ solution as having a negative imaginary part and label it as the proper solution.

$$k_z = \begin{cases} +k_z \text{ such that } Im(k_z) \leq 0, & \text{proper Riemann sheet} \\ \\ -k_z \text{ such that } Im(k_z) > 0, & \text{improper Riemann sheet} \end{cases} \tag{2.10}$$

Mathematically speaking, if we let $k_z^2 = |k_z|^2 e^{-j2\phi}$ in polar form,

$$k_z = \begin{cases} \sqrt{|k_z|^2 e^{-j2\phi}} = |k_z| e^{-j\phi}, & \text{proper Riemann sheet} \\ \\ \sqrt{|k_z|^2 e^{-j(2\phi+2\pi)}} = |k_z| e^{-j(\phi+\pi)}, & \text{improper Riemann sheet} \end{cases} \tag{2.11}$$

Note that this definition is completely arbitrary. One can define any branch cut on the Riemann sheet. For example, the sign of the real part of $k_z$ could be chosen instead of the imaginary part and the results would be equally valid albeit more difficult to assign a physical interpretation. We make such a choice since it lends itself into easily identifiable subregions with distinct features, as we will see later in this section.

The evaluation of $k_z$ in different Riemann sheets is illustrated in Figure 2.4. The wiggly blue line shows the branch cut on (or just above) the positive real axis. The orange and green arrows are examples of how the square root is evaluated in the proper and improper sheets. The angle $\phi$ is defined in equation (2.11). The dashed arcs show how the phase changes before and after the square root.

The left panel in Figure 2.4 shows the proper Riemann sheet. The branch cut is on (or just above) the positive real axis which is included in the proper domain, i.e. $k_z$ is can become purely real and positive. The phase of $k_z$ is always between 0 and $\pi$, namely $0 \leq \phi < \pi$, ensuring that the imaginary part of $k_z$ is always negative. Note that a negative imaginary part means attenuation of the fields in the positive (negative) $z$ direction for a plane wave propagating in the $+z$ $(-z)$ direction (a more correct statement would read: a negative imaginary part means attenuation of the fields in the direction of the phase velocity). This is the main reason why this sheet is commonly called the *physical* Riemann sheet. However, this statement contains one implicit assumption that may not be obvious initially, and does not hold true for surface waves such as SPPs that exist between media with positive and negative permittivities. The assumption is that $k_z^2$ is always in the third quadrant and therefore $k_z$ is always in the fourth quadrant for passive and lossy media. Considering the equation $k_z = \sqrt{\epsilon k_0^2 - k_x^2}$, one might reasonably claim that $\epsilon$ has a negative imaginary part (passive, lossy), $k_0$ and $k_x$ are real, then the assumption holds. However, for SPPs, $k_x$ is not real but a complex number with a negative imaginary part, as seen in Chapter 1 for two semi-infinite media. This throws off $k_z^2$ into the second quadrant and, as a result, $k_z$ lands in the third quadrant with a *negative* real part. And there is a very good reason for this. SPPs have most of their energy concentrated near the metal's surface, which is, in time, absorbed by the metal film. In other words, *the fields are growing in the direction of the power flow*, which is exactly the opposite of what one would expect for a plane wave in a uniform medium.

The right panel in Figure 2.4 shows the improper Riemann sheet. The positive real axis is no longer included in the values that $k_z$ can obtain. If $k_z^2$ is purely real and positive, then $k_z$ coincides with the negative real axis, as shown by the green example. The phase of $k_z$ is always between $\pi$ and $2\pi$, namely $\pi \leq \phi < 2\pi$, so that the imaginary part of $k_z$ is always positive. This is commonly referred to as the *unphysical* Riemann sheet for the reasons just explained above. We will refer to this as the improper sheet because calling it unphysical gives the false impression that modes on this sheet has no relevance to physical outcomes, which is incorrect.

Note that the Riemann sheets in Figure 2.4 are plotted with respect to the real and imaginary parts of $k_z$, i.e. the axes correspond to the real and imaginary parts of $k_z$. This places the branch point right in the origin of the coordinate system. When representing the modes of layered media, the tangential component $k_x$ of the wave vector will be used. Although this is not mandatory, it makes our lives easier because $k_x$ is a conserved quantity in all layers and characteristically defines the modes. Therefore, we will later switch to representing the Riemann sheets with respect to $k_x$.

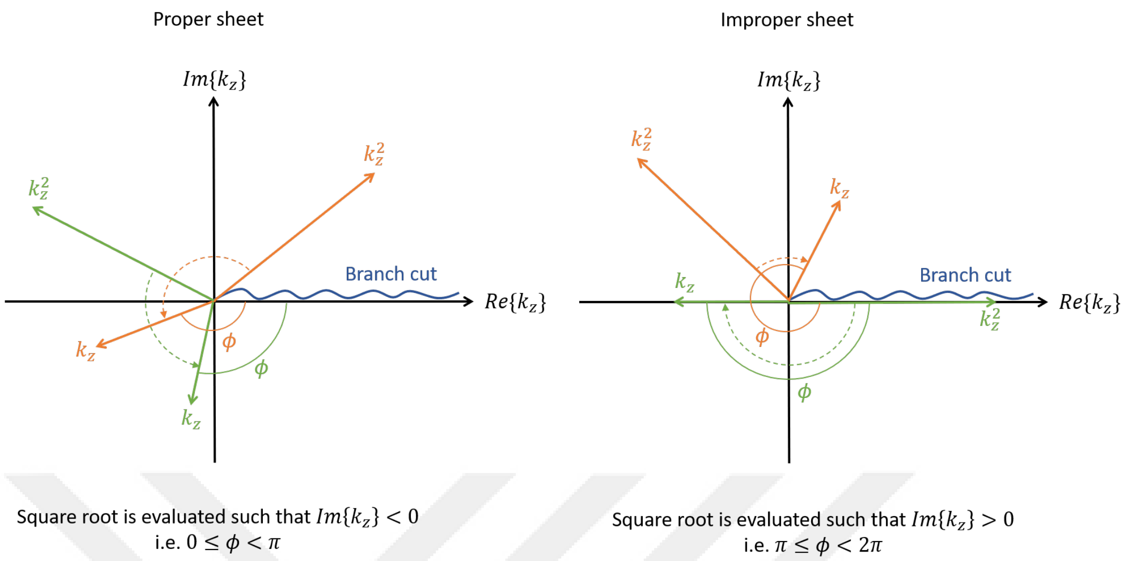


Figure 2.4: The branch cuts in the evaluation of the normal component of the wave vector. The expression for the normal component $k_z$, given in equation (2.11), leads to two different choices due to the multi-valued nature of the square root function. The left and right panels represent these choices as the proper and the improper sheets, respectively. On the proper sheet, $k_z$ has a negative imaginary part (including the positive real axis). On the improper sheet, $k_z$ has a positive imaginary part (including the negative real axis). Orange and green arrows show two examples of $k_z^2$ values and how their square roots are evaluated.

Now that the branch cut and the two Riemann sheets are clearly defined, the reflection and transmission coefficients can be explicitly expressed in both the proper and improper sheets. As mentioned earlier, we are interested in the Riemann sheets that arise in the evaluation of $k_{z1}$, the normal component of the wave vector in the incidence medium, since, for any realistic scenario, there will be both incoming and outgoing waves in this first layer. In the last layer (transmission layer), it can be easily ensured by experimental design that there are no incoming waves towards the waveguide. We will also prove that the choice of branch for intermediate layers does not affect any of the results (see Appendix A).

Starting with the Fresnel reflection coefficient (1.8a), one can simply substitute $+k_{z1}$ and $-k_{z1}$ for $k_{z1}$ and get the expressions for the proper and improper sheets, respectively.

$$r_1 = \begin{cases} \dfrac{\epsilon_2 k_{z1} - \epsilon_1 k_{z2}}{\epsilon_2 k_{z1} + \epsilon_1 k_{z2}} = r_1^p, & \text{proper Riemann sheet} \\ \\ \dfrac{-\epsilon_2 k_{z1} - \epsilon_1 k_{z2}}{-\epsilon_2 k_{z1} + \epsilon_1 k_{z2}} = \dfrac{1}{r_1^p}, & \text{improper Riemann sheet} \end{cases} \tag{2.12}$$

where the superscript $p$ stands for *proper*. Using this result in generalized reflection and transmission coefficients, equations (2.5) and (2.6) become

$$\tilde{r} = \begin{cases} \dfrac{r_1^p + r_2 e^{-jk_{z2}2d}}{1 + r_1^p r_2 e^{-jk_{z2}2d}} = \tilde{r}^p, & \text{proper Riemann sheet} \\ \\ \dfrac{\frac{1}{r_1^p} + r_2 e^{-jk_{z2}2d}}{1 + \frac{1}{r_1^p} r_2 e^{-jk_{z2}2d}} = \dfrac{1}{\tilde{r}^p}, & \text{improper Riemann sheet} \end{cases} \tag{2.13}$$

$$\tilde{t} = \begin{cases} \dfrac{(1 + r_1^p + r_2 + r_1^p r_2) e^{-jk_{z2}d}}{1 + r_1^p r_2 e^{-jk_{z2}2d}} = \tilde{t}^p, & \text{proper Riemann sheet} \\ \\ \dfrac{\left(1 + \frac{1}{r_1^p} + r_2 + \frac{1}{r_1^p} r_2\right) e^{-jk_{z2}d}}{1 + \frac{1}{r_1^p} r_2 e^{-jk_{z2}2d}} = \dfrac{\tilde{t}^p}{\tilde{r}^p}, & \text{improper Riemann sheet} \end{cases} \tag{2.14}$$

One of the striking results here is that the generalized reflection coefficients on the proper and improper sheets are the inverse of each other. This implies that the modes (i.e. poles) on the proper sheet become zeros in the improper sheet, and vice versa. Another striking result is that all modes on the proper sheet of $\tilde{t}$ disappear in the improper sheet because $\tilde{r}$ and $\tilde{t}$ share all of their poles in the proper sheet. Instead, the zeros of $\tilde{r}$ become poles in the improper sheet of $\tilde{t}$. The importance of these observations will be clear in the following sections when we investigate SPP modes and how various experimental configurations influence the excited SPP.

These results are not unknown. On the contrary, detailed investigations of branch cuts, Riemann sheets, poles and zeros have already been available in the literature for a long time [46, 47, 43]. However, these results are usually overlooked or completely forgotten especially in emerging fields. Properly accounting for these fundamental relationships in the investigation of SPPs not just expands our understanding and intuition around the topic, but also reveals new methods that can be utilized to further refine and improve the design of plasmonics devices. In this study, we investigate these expressions in detail and see that they provide valuable insights and tools to tailor surface plasmons.

### *2.3.2 SPP modes on the Riemann sheet*

One of the simplest structures that can support an SPP mode is a thin metal film surrounded by air on both sides (e.g. Figure 1.13). We start with this structure and discuss the properties of SPPs. Let's assume the metal film has a thickness $d = 50nm$, whose permittivity is represented by the Drude model in equation (1.19), which is discussed in Section 1.3, with the following parameters: $\omega_p = 1.04 \times 10^{16}\ rad/s$, $\gamma = 6.15 \times 10^{14}\ rad/s$, $\epsilon_{inf} = 4$. The system is excited at a free space wavelength of 490 $nm$. The generalized reflection and transmission coefficients are calculated using equations (2.13) and (2.14), respectively, and the values on both the proper and the improper Riemann sheets are plotted in Figure 2.5. The figure shows two surfaces in three dimensions: one for $\tilde{r}$ and the other for $\tilde{t}$. The $x$ and $y$ axes are the real and the imaginary parts of the normalized tangential wave vector $k_x/k_0$, respectively. The reflection and transmission coefficients are mapped onto the surfaces for each value of $k_x$ using the color axis (bright/yellow colors show high and dark/blue colors show low values). The $z$ axis shows the phase of the normal component of the wave vector $k_{z1}$. As discussed Section 2.3.1, the upper portion defined by $0 \leq \phi < \pi$ is the proper Riemann sheet, and the lower portion ($\pi \leq \phi < 2\pi$) is the improper sheet. The branch cuts for the first and the last medium are shown with red and purple lines, respectively. The branch points are also shown as circles with the same color. Note that the branch cuts and branch points for both of these layers are the same, since they are the same material.

In the proper sheet of either $\tilde{r}$ or $\tilde{t}$, two poles can be identified. Note that the poles in the proper sheet are at the same $k_x$ value for $\tilde{r}$ and $\tilde{t}$, since the denominators of equations (2.13) and (2.14) are exactly the same. Since the waveguide material is

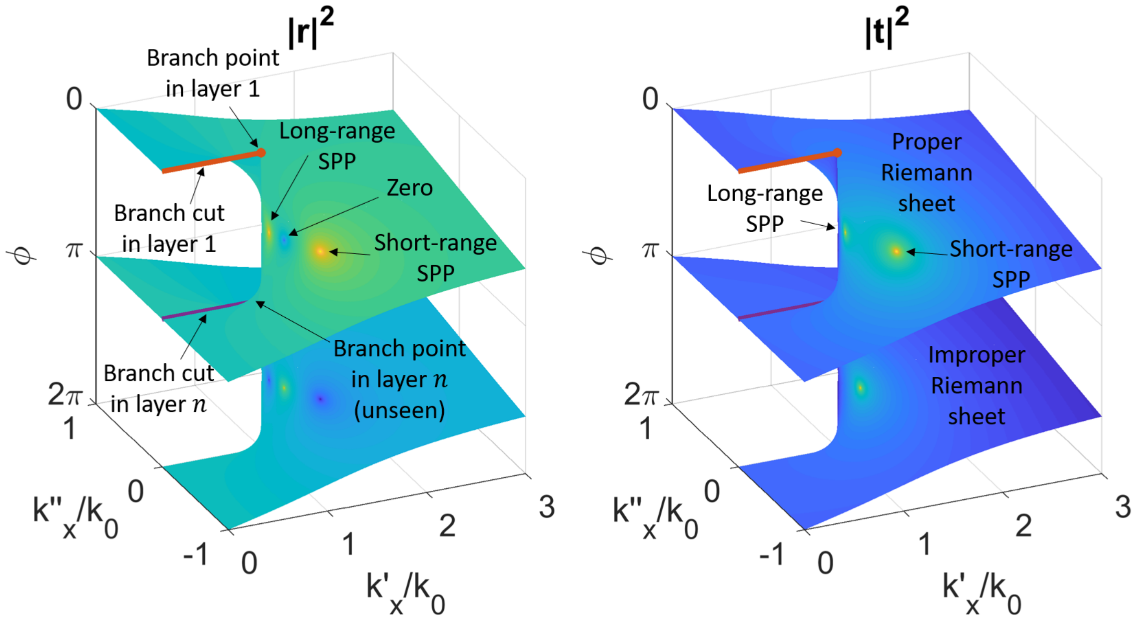


Figure 2.5: Generalized reflection and transmission coefficients for the air-metal-air structure evaluated on the complex $k_x$ domain for both the proper and improper Riemann sheets. The $x$ and $y$ axes show the real and imaginary parts of $k_x$. The $z$ axis is the phase of the $k_z$ in phasor representation, as described in equation (2.11) and in Figure 2.4. The magnitude square of the coefficients are mapped onto the Riemann sheets as the color. Specifically, $(0, \infty)$ range is mapped to the (dark blue, light yellow) color range. Dark blue and light yellow circles indicate the locations of the zeros and the poles of equations (2.13) and (2.14), respectively. The left figure shows the generalized reflection coefficient $\tilde{r}$ and the right figure shows the generalized transmission coefficient. Red and purple lines show the branch cuts in air.

a metal, both of these poles are SPP modes; or otherwise we would not be able to observe any poles in this region. The mode with smaller $k_x''$ is labelled the *long-range SPP* because it can travel much further than the other SPP mode, named the *short-range SPP*, with larger $k_x''$. The conventional approach for naming these two SPP modes observed in dielectric-metal-dielectric structures is to look at the symmetry of their $E_x$, $E_z$ and $H_y$ field distributions with respect to the $x$ axis (along the center of the waveguide) and call them even or odd depending on whether distributions are symmetric or antisymmetric [48, 15]. That convention is not preferred in this thesis because, first, it is non-intuitive and there are conflicting definitions in the current literature [49, 50] and second, as soon as the dielectric regions around the waveguide differ from each other (e.g. glass-metal-air waveguide), the symmetry is lost. On the other hand, long-range and short-range terms have a direct correspondence with the parameter $k_x$, which is characteristically used to define surface modes (this type of definition is also used in the literature [14, 51]). Notice that both SPP modes are beyond the branch point $k_x = k_0$, meaning that these SPP modes have complex $k_z$ values in the outermost layers. As a result, they are confined to the metal waveguide and decay away from the waveguide.

In agreement with the observations made on equations (2.13) and (2.14), the poles and zeros in the proper sheet of $\tilde{r}$ are reversed in the improper sheet. The poles in $\tilde{r}$ and $\tilde{t}$ are shared on both the proper and the improper sheets, while, unlike $\tilde{r}$, $\tilde{t}$ does not have zeros. The zero between the two SPP modes will be investigated in detail later for the glass-metal-air waveguide, but we should note that this zero becomes a pole in the improper sheet of $\tilde{t}$, as seen in the right panel of Figure 2.5. This will play an important role in the experimental results obtained in the KRC.

We now look at the field and power distribution of these two SPP modes. The distributions for the long-range SPP are given in Figure 2.6 (detailed field distributions for all components of **H**, **E** and **S** are given in Appendix B.1). The interfaces are shown by horizontal dashed lines with respect to the coordinate system defined in Figure 2.2. It is seen that the wave is confined to the metal film and decay almost to zero within a distance of one wavelength in **z** direction. The fields are symmetric around the waveguide. We pay more attention to the Poynting vector, as it will play a key role in explaining the electromagnetic response in experimental configurations. The tangential component **x** of the Poynting vector is in the positive direction in the dielectric regions; however, it points in the negative direction within the metal film. This is indeed a result of the attenuation that the SPP mode experiences as it propagates along the waveguide. If the mode profile is integrated over the entire **z** axis, it can be seen that the average power flow is always in the positive **x** direction. The vertical component $S_z$ always points towards the metal film in the outer dielectric regions, implying that the metal film absorbs energy.

The field profiles for the short-range mode in the air-metal-air structure is shown

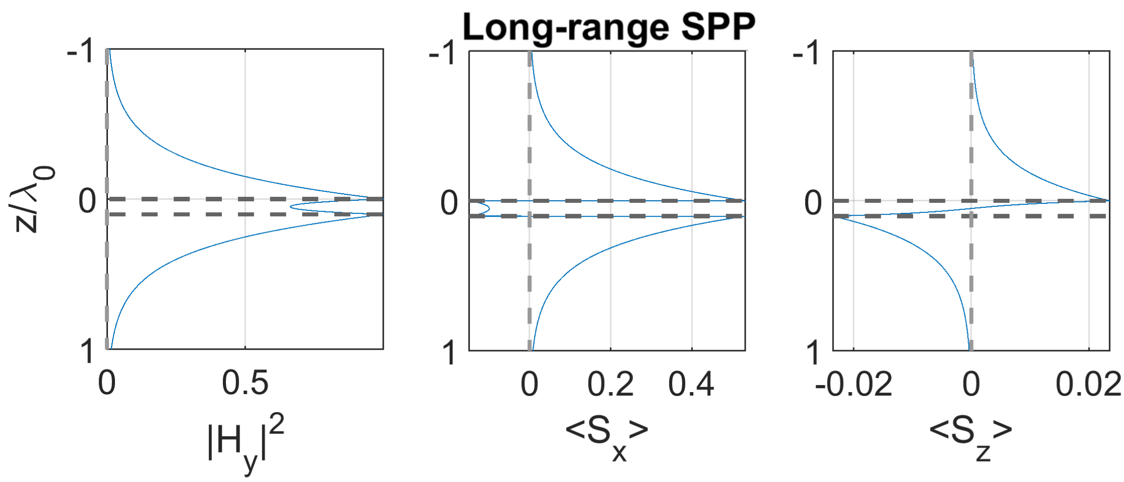


Figure 2.6: The field and time-averaged Poynting vector distributions for the long-range SPP mode in the air-metal-air structure as shown in Figure 2.5. The fields are localized near the metal interfaces and symmetric around the waveguide. The normal component of the Poynting vector $S_z$ points towards the waveguide in the dielectric regions as a result of the absorption in the metal film. Similarly, the tangential component $S_x$ points in the negative direction within the metal film.

in Figure 2.7. The short-range SPP is more tightly confined around the metal surfaces and decay more swiftly away from the metal due to the large tangential wave vector $k'_x$. Even though these are usually desired features, this SPP mode also has a larger propagation loss due to a larger imaginary part $k''_x$, hence the label *short-range*. The symmetry properties and the direction of the power flow are the same as the long-range SPP mode. The fact that the short-range SPP mode is farther from the real axis on the Riemann sheets in Figure 2.5 makes it a more difficult mode to excite in an experimental configuration. As we will see later, when the top and bottom dielectric regions are not identical, the short-range mode becomes even more inaccessible. However, we will also see in Chapter 3 that this is the mode mainly responsible for the enhanced resolution in Veselago's lens (also known as Pendry's lens or the Superlens).

Next, we study the glass-metal-air structure (see Figure 2.2), which is more representative of experimental setups such as the KRC (Kretschmann-Raether configuration) and Otto configuration. The glass is the medium of incidence. For this

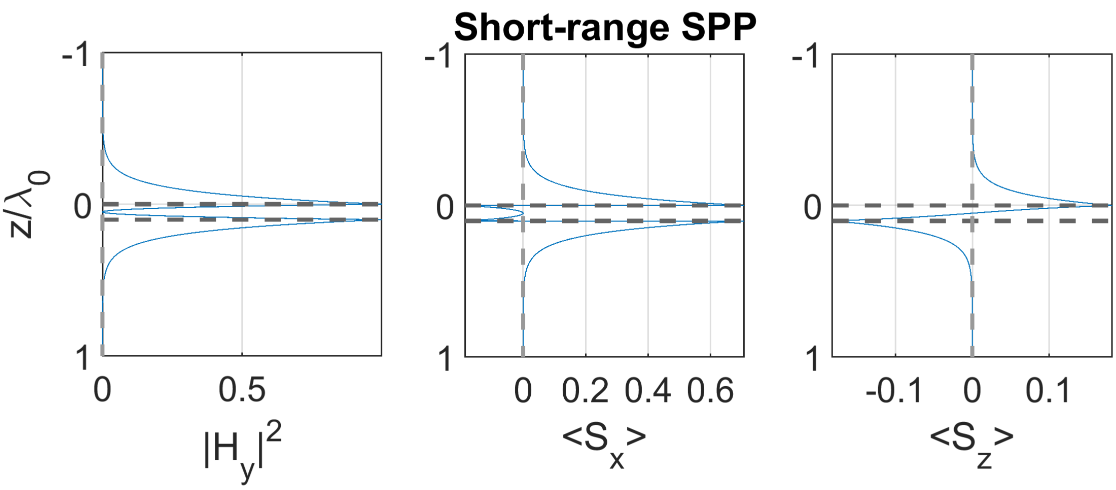


Figure 2.7: The field and time-averaged Poynting vector distributions for the short-range SPP mode in the air-metal-air structure as shown in Figure 2.5. The fields are more tightly confined near the metal interfaces compared to the long-range SPP mode due to the large tangential wave vector component $k'_x$. The short-range SPP mode also decays faster in the propagation direction $\mathbf{x}$ because of its larger imaginary part $k''_x$.

structure, we assume that the glass has a dielectric constant of 4, i.e. $\epsilon_1 = 4$. The Drude metal parameters are the same as in the air-metal-air structure that was previously analyzed, and the system is excited with the same free space wavelength of 490 $nm$. The generalized reflection and transmission coefficients on both Riemann sheets are shown in Figure 2.8. Since the incidence and transmittance media have different dielectric constants, their distinct branch cuts and branch points are easily visible on the Riemann sheet. The branch points for glass and air are, respectively, at $k'_x/k_0 = 2$ (orange) and $k'_x/k_0 = 1$ (purple). The long-range SPP is beyond the branch point of air but smaller than the branch point of glass, implying that propagating waves in glass can couple to this SPP mode. This is indeed the main purpose of using material with a higher dielectric constant as the medium of incidence in experimental setups such as the KRC. The short-range SPP is located at large $k'_x$ and $k''_x$ values, outside the plotted $k_x$ range on the Riemann sheets as shown by the arrow in Figure 2.8. The reason for this further separation of long and short range SPP modes as compared to the air-metal-air waveguide (c.f. Figure 2.5) will be clear when the field distributions of these SPPs are investigated below. Again, in

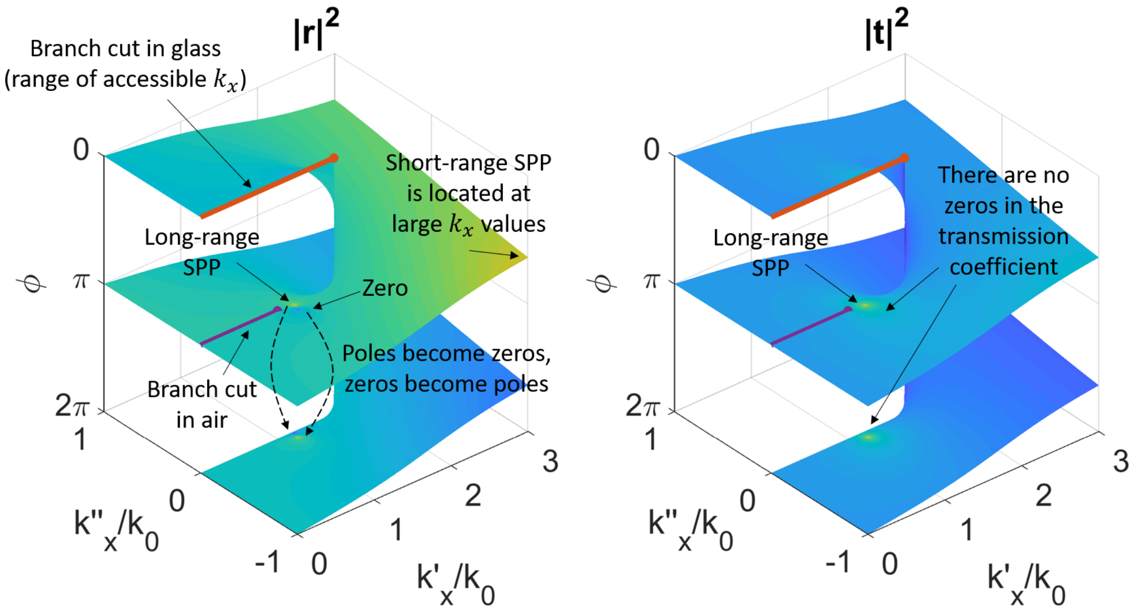


Figure 2.8: Generalized reflection and transmission coefficients for the glass-metal-air structure evaluated on the complex $k_x$ domain for both the proper and improper Riemann sheets. The $x$ and $y$ axes show the real and imaginary parts of $k_x$. The $z$ axis is the phase of the $k_z$ in phasor representation, as described in equation (2.11) and in Figure 2.4. The magnitude square of the coefficients are mapped onto the Riemann sheets as color (see detailed explanation in Figure 2.5). Red and purple lines show the branch cuts in glass and air, respectively. The long-range SPP is located between the branch points in air and glass. The short-range SPP is located at a very large $k_x$ value (not seen in the figure). As expected from equation (2.13), the poles and zeros in the proper sheet of $\tilde{r}$ become zeros and poles in the improper sheet, respectively. There are no zeros in $\tilde{t}$ (except for the branch point), in line with equation (2.14).

accordance with equations (2.13) and (2.14), the poles and zeros in the proper sheet $\tilde{r}$ respectively turn into zeros and poles in the improper sheet. For $\tilde{t}$, there are no zeros except for the trivial zero at $k_x = \sqrt{\epsilon_1}k_0 = 2k_0$, i.e. grazing incidence angle of 90°.

There are two poles in the transmission coefficient: one in the proper, another in the improper sheet, which we simply skipped over when we were analyzing air-metal-air structure. We already know that these poles are located at different $k_x$ values (see eq. (2.14)). This fact begs the following question: Which of these poles is the true SPP mode? To answer this question, we will prove the items below one by one and consequently show that both of these poles play an important role in the description of phenomena associated with SPPs.

1. The field profiles of these two modes are completely different in the incidence medium. For the mode in the proper sheet, the fields decay away from the metal film, while they grow for the mode in the improper sheet. However, this does not mean that the mode on the improper sheet is inconsequential for real-life scenarios.

2. Any given mode/pole in one Riemann sheet of $\tilde{r}$ have exactly the same field profile as its counterpart zero on the opposite Riemann sheet at the same $k_x$ value. This is true for any pole or zero.

3. The existence of a pole (an SPP mode) in $\tilde{r}$ necessitates the existence of a zero nearby in the complex $k_x$ plane, which manifests itself as a pole in the opposite Riemann sheet. Therefore, all poles and zeros seen in both Riemann sheets in Figure 2.8 are the result of the surface plasmon resonance.

4. In the experimental setups such as the KRC, a plane wave excitation can only satisfy the conditions at $\phi = 0$, well away from $\phi = \pi$ (see the proper branch in Figure 2.4 and the orange line in Figure 2.8). This implies that the response observed in experimental setups is due to the pole and the zero in the improper sheet, not due to those in the proper sheet. Since the salient features of SPPs are generally calculated using only the proper sheet, this distinction must be taken into account in the interpretation of experimental results.

5. The dip in the reflectance spectra observed in experimental setups (i.e. the extinction of the incidence wave by the plasmon resonance) is due to the manifestation of the pole in the proper sheet as a zero in the improper sheet. The maximum observed in the transmission spectra (i.e. the field enhancement) is

due to the manifestation of the zero in the proper sheet as a pole in the improper sheet. As a result, there is a difference between the incidence angles at which the reflectance minimum and the transmission maximum are observed.

### *2.3.3 SPP mode profiles*

We start by looking at the field profiles of the poles and the zero in the proper sheet of $\tilde{r}$ in Figure 2.8. The field profile of the long-range SPP is shown in Figure 2.9. As noted earlier, due to the asymmetry between the dielectric constants of the regions surrounding the metal layer, the field profile is no longer symmetric (that's why we prefer to use *long/short-range* instead of *symmetric/asymmetric* to label the two SPP modes that exist in metal films). The fields are concentrated around the interface between the air and the metal layers. This implies that the long-range SPP is mainly associated with the air-metal interface. In other words, the SPP mode associated with the lower index dielectric medium always travels farther because the characteristic wave number $k_x$ of the mode is smaller (both real and imaginary parts). This will also be evident from the film thickness dependence of SPP modes, which is discussed in later sections (see Figure 2.26 in Section 2.4.3). The mode has a very low decay rate in the glass, and therefore, it is only weakly confined in this region. This confinement is the results of the non-zero imaginary part of $k_x$. Otherwise, the mode would be completely unconfined, or propagating, in glass because the real part of $k_x$ is smaller than the branch point in glass $\sqrt{\epsilon_{glass}}k_0$.

The field profile of the short-range SPP is given in Figure 2.10. It is observed that this mode is associated with the glass-metal interface. Since the short-range SPP has a wave vector $k_x$ that is larger than the branch point in glass, the short-range SPP is tightly confined to the interface, but does not travel far. For the same reason, this mode cannot be excited using plane waves in the glass region, unlike the long-range SPP.

Figure 2.11 shows the field distribution at the location of the zero in the proper sheet of $\tilde{r}$. Notice how the fields grow in the $-\mathbf{z}$ direction in the glass away from the metal film. Although the pole corresponding to the long-range SPP and the

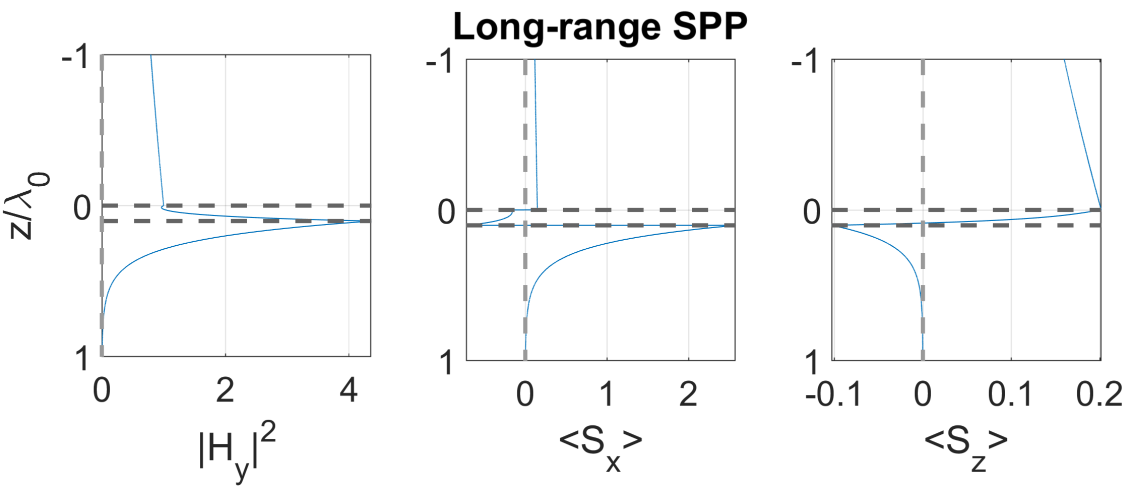


Figure 2.9: The field and time-averaged Poynting vector distributions for the long-range SPP mode in the glass-metal-air structure as shown in Figure 2.8. The fields are localized near the bottom interface between metal and air. The fields decay at a much slower rate in glass than in air; therefore, the SPP is only weakly confined on the glass side.

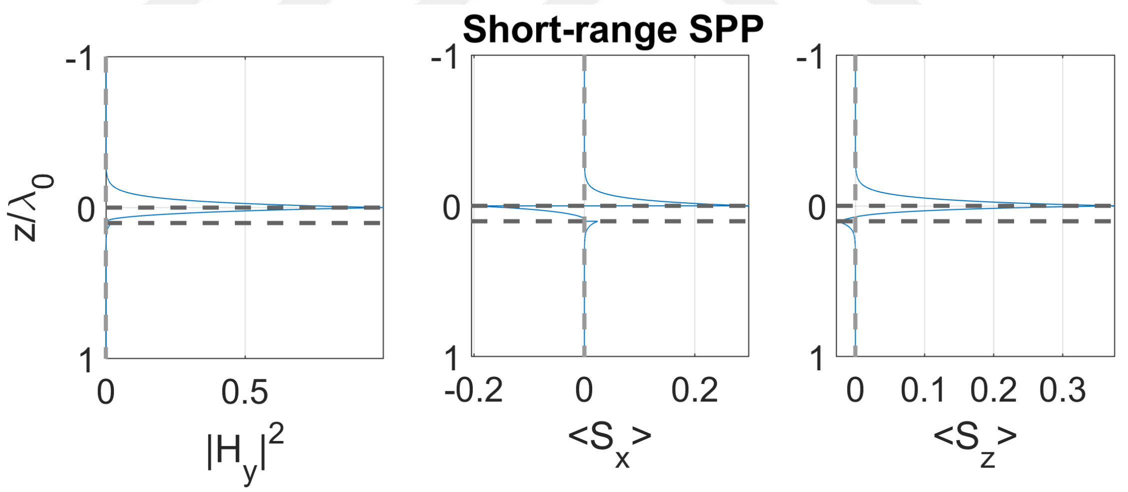


Figure 2.10: The field and time-averaged Poynting vector distributions for the short-range SPP mode in the glass-metal-air structure as shown in Figure 2.8. The fields are localized near the top interface between glass and metal. The fields decay at a fast rate on both sides of the metal waveguide, and therefore, the SPP is tightly confined.

zero are very close to each other on the complex $k_x$ plane, their field profiles are completely different in the incidence layer. Local field enhancement can still be observed at the interface between the air and the metal. At first sight, this looks as if an incoming field decaying in the $+\mathbf{z}$ direction is impinging on the glass-metal interface and exciting the SPP mode on the air-metal interface. However, a more careful look at the Poynting vector profile clearly shows that the power flow is in the $-\mathbf{z}$ in all three layers, i.e. the energy is emerging from the metal, propagating in the unbounded glass region and simultaneously growing in the direction propagation. This picture, of course, violates the radiation condition for plane waves in unbounded media. However, even though we cannot relate the field distribution to a physical picture, we will see, in the upcoming sections, that this zero plays an important role and is a consequence of the long-range SPP mode.

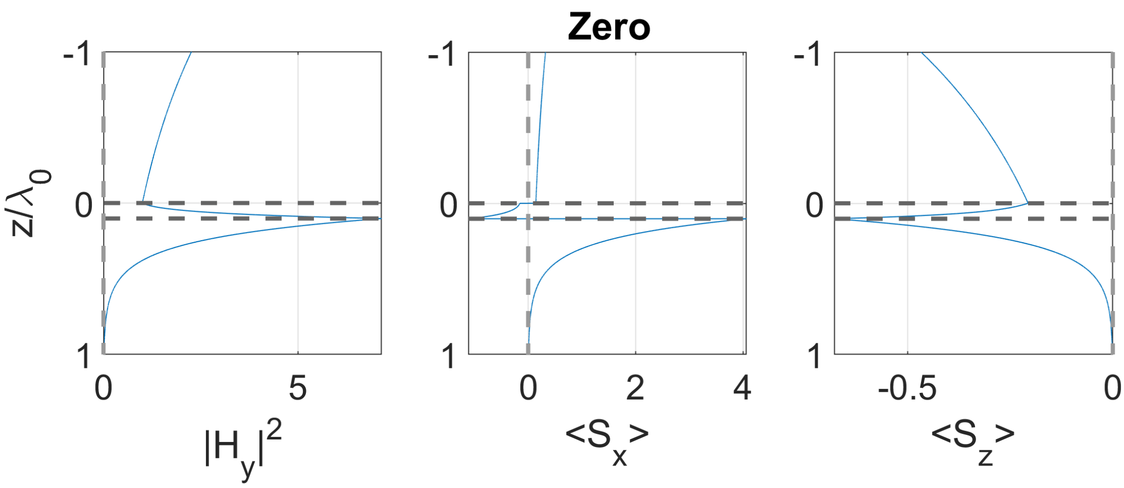


Figure 2.11: The field and time-averaged Poynting vector distributions for the zero in the glass-metal-air structure as shown in Figure 2.8. The fields and the Poynting vector in the medium of incidence are growing in the $-\mathbf{z}$ direction, away from the metal film. The Poynting vector also points away from the metal film. Although this looks unphysical at first sight, we will see in the forthcoming sections that this zero plays an important role in the response of plasmonic structures.

### *2.3.4 Pole-zero relationship on opposite Riemann sheets*

The relationship between the proper and the improper sheets has been established in equations 2.13 and 2.14. As discussed previously, the most striking observation is perhaps that the modes/poles on one sheet of the generalized reflection coefficient $\tilde{r}$

become zeros on the other sheet at exactly the same tangential wave vector value. In previous sections, we showed the field distribution for the poles/zeros in the proper sheet only. Now, we investigate the field distributions of these poles and zeros and establish a more detailed connection between their field distributions.

The fields in the second layer can be expressed in terms of the fields in the first layer as in equation (2.15). This is valid for any Riemann sheet; the specific sheet is determined by the branch cut in $k_{z1}$.

$$H_2^+ = \left[\frac{H_1^+}{2}\left(1+\frac{\epsilon_2 k_{z1}}{\epsilon_1 k_{z2}}\right)+\frac{H_1^-}{2}\left(1-\frac{\epsilon_2 k_{z1}}{\epsilon_1 k_{z2}}\right)\right]e^{-jk_{z2}d_1} \tag{2.15}$$

$$H_2^- = \left[\frac{H_1^+}{2}\left(1-\frac{\epsilon_2 k_{z1}}{\epsilon_1 k_{z2}}\right)+\frac{H_1^-}{2}\left(1+\frac{\epsilon_2 k_{z1}}{\epsilon_1 k_{z2}}\right)\right]e^{jk_{z2}d_1} \tag{2.16}$$

Now, consider the fields in layer 1 of Figure 2.3 for a pole/mode on the proper Riemann sheet. In this case, the amplitude of the incident field needs to be set to zero, i.e. $H_1^+ = 0$. As usual, we indicate the proper solution for $k_{z1}$ with $+k_{z1}$ with a negative imaginary part, decaying away from the interface. The improper solution is obtained by replacing $k_{z1}$ with $-k_{z1}$. Using equation (2.15), the fields in the second layer become

$$\begin{aligned} H_2^+ &= \frac{H_1^-}{2}\left(1-\frac{\epsilon_2 k_{z1}}{\epsilon_1 k_{z2}}\right)e^{-jk_{z2}d_1} \\ H_2^- &= \frac{H_1^-}{2}\left(1+\frac{\epsilon_2 k_{z1}}{\epsilon_1 k_{z2}}\right)e^{jk_{z2}d_1} \end{aligned} \tag{2.17}$$

with the field $H_1 = H_1^- e^{jk_{z1}z}$ in the first layer. On the improper sheet, however, the pole becomes a zero according to equation (2.13); and therefore, the reflection must be zero, i.e. $H_1^- = 0$. The improper solution is denoted by $-k_{z1}$ with a positive imaginary part, growing away from the interface. Substituting this into (2.15), the fields in the second layer become

$$\begin{aligned} H_2^+ &= \frac{H_1^+}{2}\left(1-\frac{\epsilon_2 k_{z1}}{\epsilon_1 k_{z2}}\right)e^{-jk_{z2}d_1} \\ H_2^- &= \frac{H_1^+}{2}\left(1+\frac{\epsilon_2 k_{z1}}{\epsilon_1 k_{z2}}\right)e^{jk_{z2}d_1} \end{aligned} \tag{2.18}$$

with the field $H_1 = H_1^+ e^{jk_{z1}z}$ in the first layer, where all $k_{z1}$'s are replaced with $-k_{z1}$. Notice that equations (2.17) and (2.18) are indeed the same except for the arbitrary coefficients $H_1^-$ and $H_1^+$. This implies that the fields in the first and the second layer are exactly the same in both cases: 1) at the pole in the proper sheet and 2) at the corresponding zero with the same $k_x$ in the improper sheet. It follows that the fields in the rest of the layers (layers 3 and above) are also the same in both cases because they are dependent on the fields in the second layer through the boundary conditions.

The conclusion to be derived from this equivalence is that the poles and zeros on opposite Riemann sheets are the results of the same electromagnetic mode. They are the manifestations of the same mode in the proper and the improper Riemann sheets, so they both should be taken into account when the response from such a plasmonic structure is interpreted. Note that this equivalence of field distributions on opposite Riemann sheets is valid only for poles and zeros. Any other point where there is both an incident wave and a non-zero reflection, the fields on opposite Riemann sheets will not be equivalent.

### *2.3.5 Extrema describing surface plasmon resonance*

The field profiles for the poles and the zero in the proper sheet (see Figure 2.8) was investigated in Section 2.3.3. The pole corresponding to long-range SPP and the zero nearby are both the consequences of surface plasmon resonance. To prove that, we show that the existence of one necessitates the existence of the other.

The zero of the reflection coefficient in the proper sheet implies that there is a $k_x$ value for which the energy reflected back into the incidence medium is zero. Such a $k_x$ value always exists for dielectric-metal-dielectric plasmonic structures, regardless of what the Drude model parameters are selected or what excitation frequency is used. This is evident from the generalized reflection coefficient (2.13): The poles of $\tilde{r}$ are located at $r_2 = -e^{jk_{z2}2d}/r_1^p$, while its zeros are located at $r_2 = -e^{jk_{z2}2d}r_1^p$. The Fresnel reflection $r_1^p$ from a Drude metal is relatively constant for a large range of frequencies, especially low frequencies (see Figure 2.12). Therefore, for each pole at $r_2 = C$, where $C$ is some complex number, there must be a zero nearby the pole approximately at $r_2 = \tilde{u}C$, where $\tilde{u}$ is a complex number close to unity. This approximation holds true as long as the Fresnel reflection coefficient $r_1^p$ is slowly changing with frequency. This is usually true for metals at relatively low frequencies. The reflection at the glass with $\epsilon = 4$ to the Drude metal, i.e. $r_1^p$, is shown in Figure 2.12. The yellow region shows the frequencies at which the approximation holds. It is seen that the reflection $r_1^p$ is a slowly-changing function of frequency, as expected. This implies that the long-range SPP and the zero occur as pairs close to each other on the complex $k_x$ plane and they are mainly associated with the interface between the air and the metal.

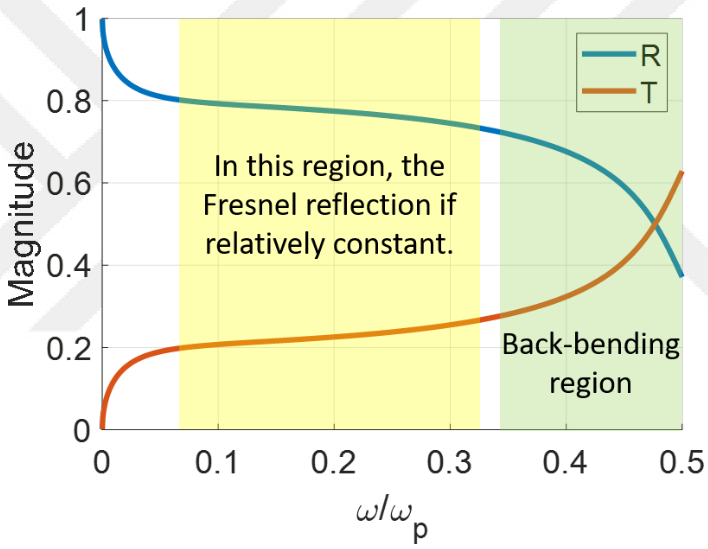


Figure 2.12: Reflection from a Drude metal for a plane wave traveling in a dielectric with $\epsilon = 4$. The same Drude model as in Section 2.3.2 is used. The Fresnel reflection coefficient is calculated for a range of frequencies. In the yellow region, the reflection is relatively constant. The green region marks the frequencies at which the back-bending in the SPP dispersion is observed.

### *2.3.6 Nature of modes on different regions of the Riemann sheet*

In this section, we put together all of the findings in the previous sections to draw a complete picture of the SPP modes on various regions of the Riemann sheet. Clearly describing the nature of the fields and the Poynting vector distinct regions of the Riemann will provide insight into the nature of the SPP modes and how they relate to the experimental observations. We study the glass-metal-air structure used in the previous sections with the metal described by the Drude model in equation (1.19), as an example. However, the results are applicable to any material combination and structures with any number of layers.

The generalized reflection coefficient for the aforementioned structure is shown in Figure 2.13. To understand the properties of the fields, we will look at the signs of the real and imaginary parts of the wave vector components. We split both the proper and improper Riemann sheets into two by using lines going through the $k_x'' = 0$ paths on which $k_x$ is purely real (shown as the black dashed lines in Figure 2.13). Note that there are two $k_x'' = 0$ lines on the Riemann sheet: one at $\phi = 0$ (or equivalently $\phi = 2\pi$) and another at $\phi = \pi$, which also correspond to the branch cuts. These lines are chosen on purpose because a change in the sign of the imaginary part of $k_x$ causes a series of sign changes in both $k_{z1}$ and $k_{z3}$. These four regions are labelled as A (upper half of the proper sheet), B (lower half of the proper sheet), C (upper half of the improper sheet) and D (lower half of the improper sheet). The evaluations of $k_{z1} = \sqrt{\epsilon_1 k_0^2 - k_x^2}$ and $k_{z3} = \sqrt{\epsilon_3 k_0^2 - k_x^2}$ determine how fields behave in the outermost regions of the structure. The branch cut for $k_{z1}$ leads to the proper and improper Riemann sheets, which we have been studying throughout this chapter. The branch cut for $k_{z3}$ is always chosen such that the fields decay away from the metal film (in the $+z$ direction), i.e. $k_{z3}'' < 0$, which complies with the radiation condition. This choice is justified by the fact that there is no incoming wave or a source anywhere in the last layer. Without loss of generality, we assume that the incident wave is in the first layer only. Taking all of these into account, we can determine the signs of the wave vector components in all four regions as follows.

| | | | |
|---|---|---|---|
| A | $k_{z1}' > 0,$ | $k_{z1}'' < 0,$ | $k_{z3}' > 0$ |
| B | $k_{z1}' < 0,$ | $k_{z1}'' < 0,$ | $k_{z3}' < 0$ |
| C | $k_{z1}' < 0,$ | $k_{z1}'' > 0,$ | $k_{z3}' > 0$ |
| D | $k_{z1}' > 0,$ | $k_{z1}'' > 0,$ | $k_{z3}' < 0$ |

where $k''_{z3} < 0$ always. These four regions are annotated with the corresponding wave vector signs in Figure 2.13.

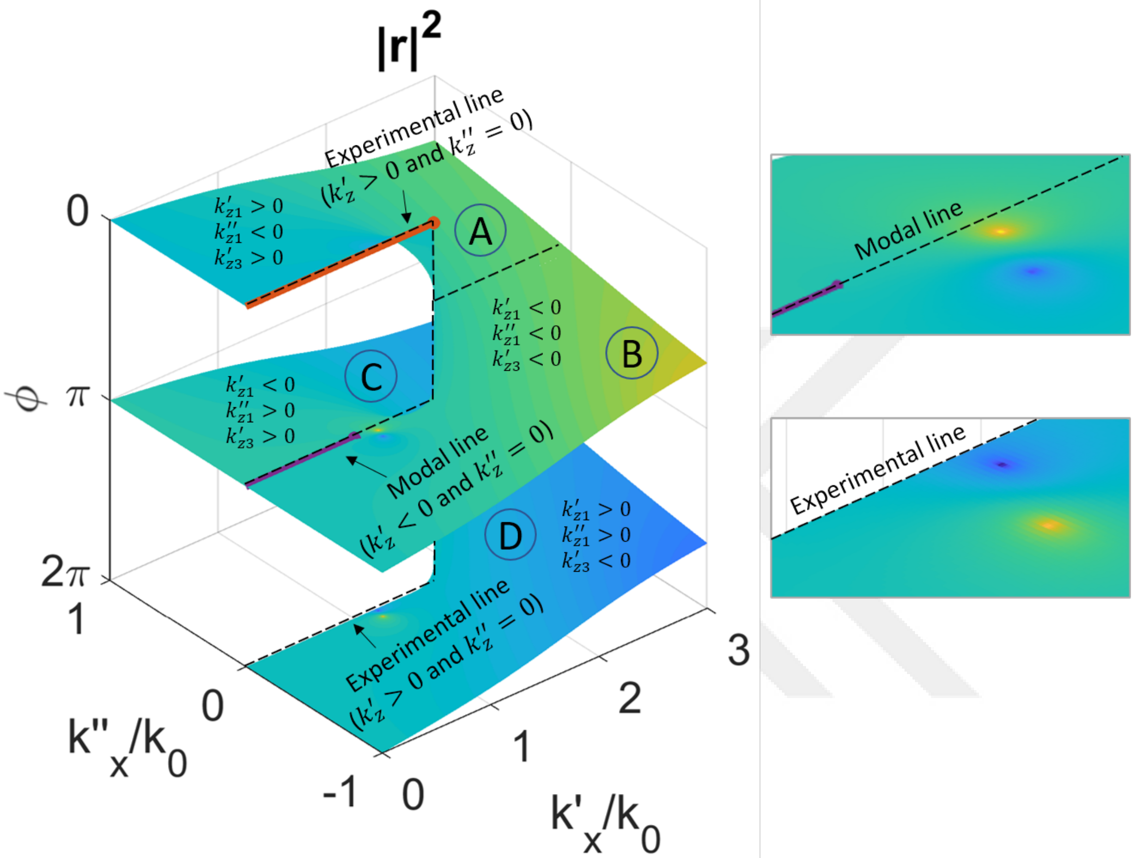


Figure 2.13: Nature of the fields on different regions of the Riemann sheet. The sheet shows the magnitude square of the generalized reflection coefficient evaluated on both proper and improper Riemann sheets. The Riemann sheets are divided into two regions each by lines going through the $k''_x = 0$ paths, i.e. the branch cuts. For each region $A$, $B$, $C$ and $D$, the signs of the wave vector components in the incidence and transmission media are shown. Note that $k''_{z3} < 0$ always. The incident wave in an experimental setup such as the KRC lies on the *experimental line* (dashed black line overlapping the red branch cut). The conventional description of an SPP mode fits the field profile of the pole near the *modal line* (dashed black line overlapping the purple branch cut). The details of these four regions are given in the main text.

At this point, we still know little about where the energy is flowing and how the fields of a mode in any of these regions are distributed. All we made sure is that the fields in the transmission medium decay away from the metal film albeit without paying any attention whether this is meaningful in all regions of the Riemann sheet.

Therefore, next, we look at the directions of the Poynting vector and field decay for modes in each of these regions. Note that the directions of the Poynting vector and the field decay are not necessarily the same, especially when electromagnetic modes in layered media are considered and/or the media involved are lossy. These directions can be determined using equation (2.8), which was derived previously to describe the Poynting vector of a mode in layered media:

$$\langle \mathbf{S}_1 \rangle = (\hat{\mathbf{x}}k'_x - \hat{\mathbf{z}}k'_{z1})\, e^{2k''_x x - 2k''_{z1} z} \frac{|H_1^-|^2}{\omega\epsilon_1\epsilon_0}$$
$$\langle \mathbf{S}_n \rangle = (\hat{\mathbf{x}}k'_x + \hat{\mathbf{z}}k'_{zn})\, e^{2k''_x x + 2k''_{zn} z} \frac{|H_n^+|^2}{\omega\epsilon_n\epsilon_0}$$

The exponents show the directions for the decay, and the power flow is determined by the coefficients of unit vectors $\hat{\mathbf{x}}$ and $\hat{\mathbf{z}}$. In Figure 2.14, the field decay and Poynting vector directions are qualitatively shown for the incidence and transmission media for all four regions of the Riemann sheet. Each case can be summarized as follows.

A The fields decay away from the intermediate layers in the normal direction in both the incidence and the transmission media. The power flow is towards infinity on both sides; the energy radiated by the intermediate layers to the outermost layers. The $\mathbf{x}$ component of the Poynting vector is in the direction of field growth.

B The fields decay in $+\mathbf{x}$ direction and away from the intermediate layers in the normal direction in both the incidence and the transmission media. The power flow is into the intermediate layers in the normal direction, implying absorption of energy by those layers. The $\mathbf{x}$ component of the Poynting vector is in the same direction as the field decay.

C The fields decay in $+\mathbf{z}$ direction in both the incidence and transmission layers. In other words, the fields decay towards the intermediate layers in the incidence layer, while they decay away from the intermediate layers in the transmission layer. Similarly, the Poynting vector is directed towards the intermediate layers in the incidence layer, and away from the intermediate layers in the transmission layer. The $\mathbf{x}$ component of the Poynting vector is in the direction of field growth.

(D) Similar to (C), the fields decay in $+\mathbf{z}$ direction in both the incidence and transmission layers. But this time, the $\mathbf{x}$ component of the Poynting vector is in the direction of field decay. The normal component of the Poynting vector point in the $-\mathbf{z}$ direction in both outermost layers, i.e. away from the intermediate layers in the incidence layer and towards the intermediate layers in the transmission layer.

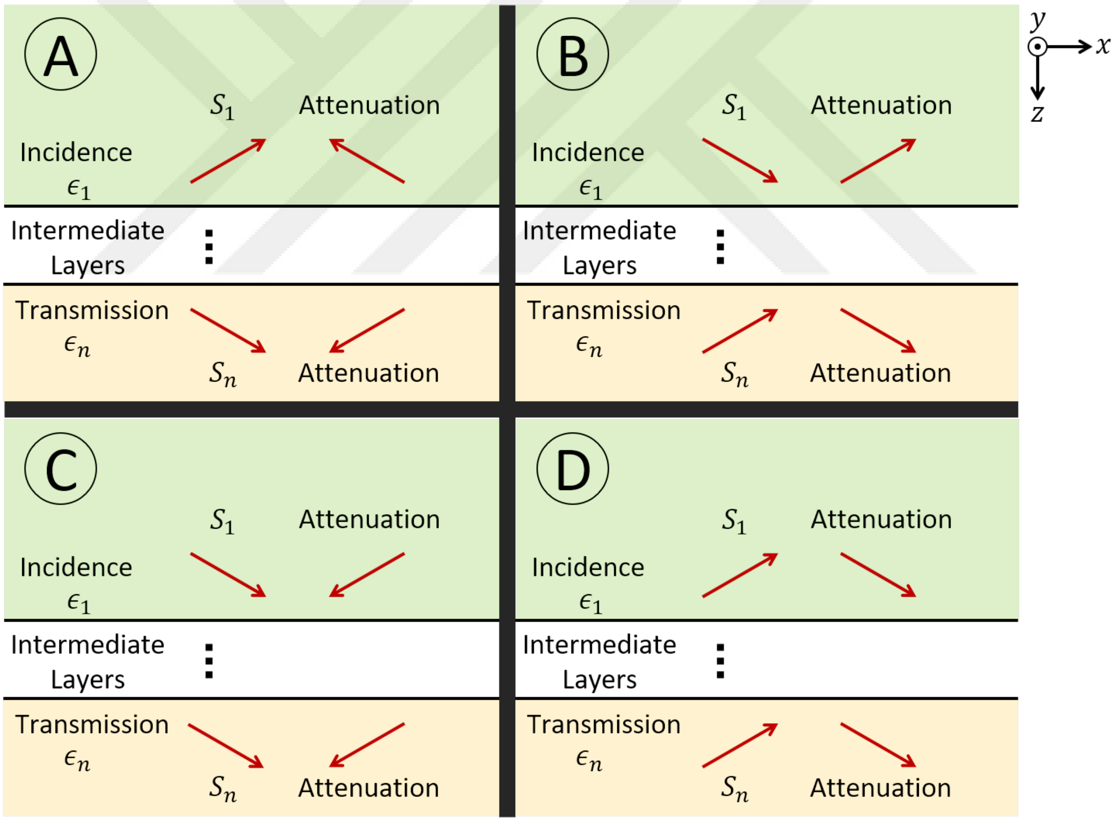


Figure 2.14: The directions of the Poynting vector and field attenuation for modes/poles in all four regions of the Riemann sheet as indicated in Figure 2.13. For each region A, B, C and D shown in Figure 2.13, the field decay and Poynting vector directions are schematically drawn in a different panel. The directions are calculated using equation (2.8). Layer 1 and $n$ are the incidence and transmission layers, respectively. The red arrows annotated with *Attenuation* show the field decay direction, and those annotated with $S$ show the Poynting vector.

We can try to qualitatively assign a physical picture to each of these cases depicted in Figure 2.14 with descriptions provided in the list above. In case A, it appears that the intermediate layers are radiating energy to outermost layers, indicating that the intermediate layers contain active media. The wave is traveling in $+\mathbf{x}$ direction and growing also in the same direction. The fact that the fields decay away from the intermediate layers indicates that the mode is bound to the waveguide; however, the fields grow in the propagation direction. Therefore, this does not fit the picture of an SPP traveling in lossy, passive media.

In case B, the fields decay away from the intermediate layers, meaning that the mode is bound to the waveguide. The energy is absorbed by the intermediate layers, as indicated by the Poynting vectors pointing towards the intermediate layers in both outermost layers. Furthermore, the tangential component of the Poynting vector is in the direction of field attenuation, which implies that the mode is losing energy as it propagates along the waveguide. Considering that, in our case, the only energy loss mechanism is the lossy metal film between the dielectric layers and the SPP is expected lose its energy as it propagates due to passive nature of the media involved, this description of field and power profile seems plausible for an SPP.

In case C, both the field decay and the Poynting vectors are in the $+\mathbf{z}$ direction in both the incidence and the transmission layers. This fits a description where the waveguide is illuminated from the incidence medium, but some of the energy leaks into the transmission medium. However, the $\mathbf{x}$ component of the Poynting vector is in the direction of field growth, which is not in line with the assumption that all media involved are passive.

In case D, the Poynting vectors are in the $-\mathbf{z}$ direction. The field and power profile in the transmission layer is in agreement with a bound mode traveling and decaying in $+\mathbf{x}$ direction. However, in the incidence layer, the Poynting vector is directed away from the intermediate layers and the fields grow in the $-\mathbf{z}$ direction, which indicates this profile does represent a bound mode.

Considering all of the observations listed above, one can say that the modes in region B fit the description of SPPs as bound modes traveling along a lossy metal waveguide which partially absorbs the energy of the SPP. This would be a correct conclusion, and this is the reason why we have labelled the poles in this region as SPPs in Section 2.3.2 and in Figures 2.5 and 2.8. However, the modes on other regions should not be dismissed as unphysical due to their unconventional field and Poynting vector profiles. We have already proved in equations (2.13) and (2.14) that SPP modes manifest themselves as poles and zeros in more than one region on the Riemann sheet as shown in Figure 2.13 with zoomed-in insets. In an experimental scenario, it is close to impossible to excite a mode with complete precision. One usually excites a plasmonic system with a practical light source, hoping that some of the electromagnetic energy will couple to the mode that is intended to be excited (of course, in practice, the source usually couples to many modes but the adverse effects of this can be reduced with clever experimental designs). One approach to excite a given SPP mode is to mimic the field profile of the SPP by, for example, matching the wave vector components of the incident wave to those of the SPP mode. This approach is used in experimental setups such the KRC (Kretschmann-Raether configuration), the Otto configuration and the grating coupler as discussed in Chapter 1. Therefore, it is critical to understand exactly what field profile the excitation source induces in the layered structure and where the source is located on the Riemann sheet.

### *2.3.7 Mapping between Riemann sheets and experimental configurations*

As explained previously, in an experimental scenario such as the KRC, the incident plane wave has a tangential wave vector that is purely real and can only excite the SPP mode partially. The Riemann sheet in Figure 2.13 for the KRC (glass-metal-air structure) has two different lines satisfying the condition $k_x'' = 0$, shown as black dashed lines (overlapping the branch cuts in red and purple). The insets in Figure 2.13 also shows the poles and zeros at a closer distance so that it is easier to distinguish visually. In the top inset where the pole and the zero are located in region B, the pole is closer to the $k_x'' = 0$ line and the effect of the zero on the $k_x'' = 0$ line is mostly masked by the pole. This implies that the response from the waveguide is expected to have a large amplitude. However, on the improper Riemann sheet, the poles and zeros are reversed, as previously shown in equation (2.13). In this case, the zero is closer to the $k''_x = 0$ line, masking the effects of the pole as shown in the bottom inset (region D), and, as a result, we expect to see a dip in the response of the waveguide. These two cases are clearly irreconcilable and cannot explain the same experimental setup. Therefore, we must be able to attribute one of these $k''_x = 0$ lines to the experimental setup without any ambiguity. To settle this, we observe the continuity of the generalized reflection and transmission coefficients ($\tilde{r}$ and $\tilde{t}$) between different regions of the Riemann sheet. Specifically, we look at how $k_{z1}$ changes when transitioning from region B and C when $k'_x$ is larger than the branch point in air but smaller than that in glass (this puts us in the vicinity of the pole and the zero, shown in the top inset of Figure 2.13). In both regions B and C, the real part of $k_{z1}$ is negative. Since $\tilde{r}$ must be continuous, we conclude that it must also be negative at the border between B and C. This is not in line with an incoming plane wave in the structure shown in Figure 2.2, where $k'_z$ must be positive. If we look at the border between A and D, we see that $k'_z > 0$, again, due to continuity of $\tilde{r}$. This is in agreement with the description of the experimental setup. To help us refer to these two lines with $k''_x = 0$, we call the one between A and D the *experimental line* and the one between B and C the *modal line*. The wave vector components on these lines can be summarized as follows.

- Modal line: $k'_{z1} < 0, \qquad k''_{z1} = 0, \qquad k'_x > 0, \qquad k''_x = 0$
- Experimental line: $k'_{z1} > 0, \qquad k''_{z1} = 0, \qquad k'_x > 0, \qquad k''_x = 0$

The modal line is between regions B and C. The wave has an outgoing nature away from the metal interface. The pole in region B near this line represents an SPP mode that is confined to the metal waveguide and losses its energy to the metal as it propagates. This perfectly fits the modal description of the SPP, hence the name of the line. On the other hand, the pole in region B manifests itself as a zero in region D near the experimental line, which is situated between regions A and D. The wave vector components fit well to the description of an incoming plane wave and being absorbed by the metal waveguide due to excitation of the SPP mode. This is the reason why a dip in the reflection spectrum is observed in experimental setups such as the KRC that are used to excite SPP modes.

In conclusion, in this section and the preceding sections, we have shown that the SPP modes may manifest themselves as zeros or poles in different Riemann sheets. Proper account of where those extrema are located and how experimental excitation sources map onto the Riemann sheet is a crucial step in understanding the SPP modes and experimental observations. Now that we are equipped with proper tools, we investigate the reflectance and transmittance spectra of plasmonic structures in the next section, starting with a short overview of the confusion in the scientific literature around the interpretation of such spectra.

### *2.3.8 Apparent discrepancy between the reflectance and transmittance spectra*

In the previous section, we discussed how experimental excitation sources relate to the SPP modes on the Riemann sheet. We now further elucidate how they affect the reflection and transmission observations in an experimental context. Figure 2.15 shows the Riemann sheets for the reflection and transmission coefficients in the KRC (glass-metal-air). The experimental line shows the $k_x$ values that are attainable in the incidence medium (glass in this case) by a propagating plane wave. The insets show, in detail, the locations of the poles and the zeros on the proper and improper sheets. Equation (2.14) dictates that the zeros in the proper sheet of $\tilde{r}$ become poles in the improper sheet of $\tilde{t}$ and the poles in the proper sheet of $\tilde{r}$ disappear in the improper sheet of $\tilde{t}$:

$$\tilde{t} = \begin{cases} \dfrac{1 + r_1^p + r_2 + r_1^p r_2 e^{-jk_{z2}d}}{1 + r_1^p r_2 e^{-jk_{z2}2d}} = \tilde{t}^p, & \text{proper Riemann sheet} \\[2em] \dfrac{1 + \frac{1}{r_1^p} + r_2 + \frac{1}{r_1^p} r_2 e^{-jk_{z2}d}}{1 + \frac{1}{r_1^p} r_2 e^{-jk_{z2}2d}} = \dfrac{\tilde{t}^p}{\tilde{r}^p}, & \text{improper Riemann sheet} \end{cases}$$

The corresponding locations of the poles of $\tilde{t}$ are shown in the insets by the black arrows. Notice that there is no longer a zero in the improper sheet of $\tilde{t}$ to block

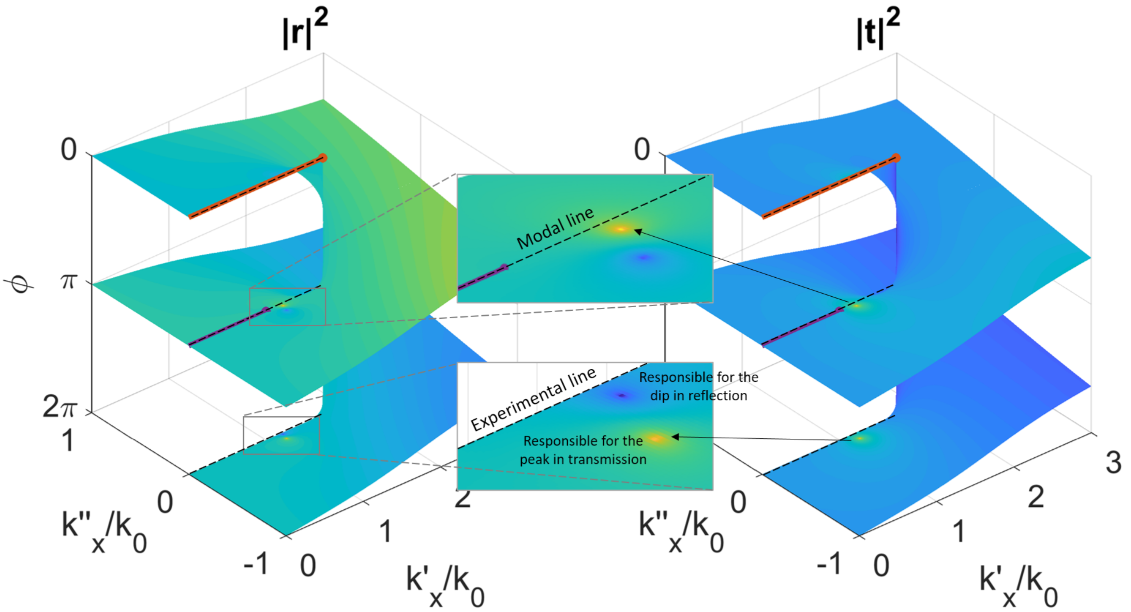


Figure 2.15: The underlying cause for the apparent discrepancy between the reflectance and transmittance spectra. The sheet shows magnitude square of the generalized reflection and transmission coefficients evaluated on both proper and improper Riemann sheets. Zoomed-in insets show the locations of the poles and zeros of the reflection coefficient. The poles on the proper and improper Riemann sheet of $|t|^2$ are located at different $k_x$ values. This in turn causes a difference between the dip of the reflection spectrum and the peak of the transmission spectrum observed on the experimental line.

the influence of the pole on the experimental line. This pole in the improper sheet of $\tilde{t}$ is responsible for the field enhancement commonly observed in the plasmonic waveguides. Since it is located at a different $k_x$ value compared to the zero that is responsible for the dip in the reflectance spectra, these two phenomena, namely the dip in reflection and the peak in transmission, occur at different angles of incidence. Indeed, many independent parameters such as the angle of incidence, the wavelength and the thickness of metal influence the outcome. Therefore, one must take this difference into account and design experimental parameters accordingly either to achieve maximum absorption or maximum field enhancement, depending on the aim of the experiment.

In order to illustrate the mismatch between the configurations where maximum absorption and the maximum field enhancement are observed, we calculate the reflection and transmission spectra for the KRC using aluminum as the metal. Figures 2.16 and 2.17 show these spectra for the free space wavelengths of $1.12\mu m$ and $1.7\mu m$, respectively. The calculations were done for two different thickness values for the aluminum metal film. The solid lines show the spectra using the thickness optimized for maximum absorption, whereas the dashed lines show the spectra using the thickness optimized for maximum field enhancement. There are a few observations to

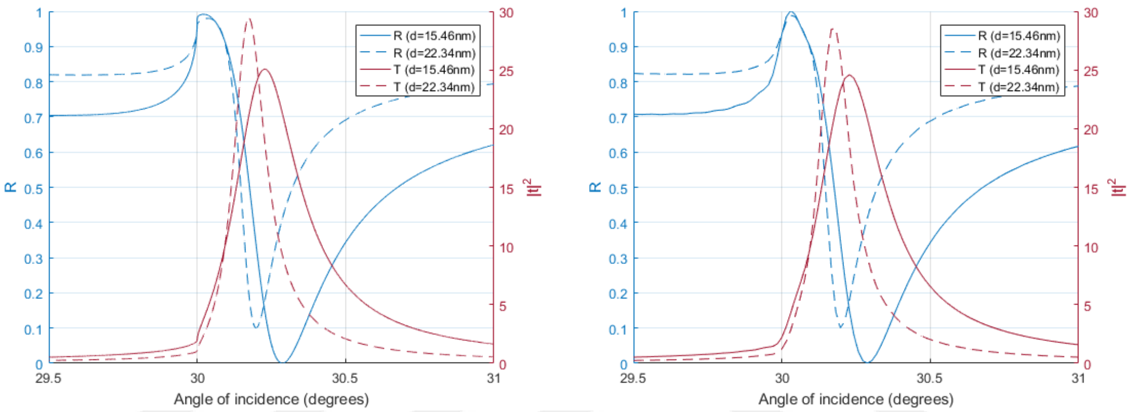


Figure 2.16: Reflection and transmission spectra for aluminum at $\lambda = 1.12\mu m$ using theory (left) and FDTD (right). The results are obtained for two different thicknesses for the aluminum: one optimized for maximum absorption, one for maximum field enhancement.

be made on these results. First, it is clear that, in all of these numerical experiments, the angle of incidence at which the minimum in $\tilde{r}$ is observed is different from the angle at which the maximum of $\tilde{t}$ is observed, for the reasons explained at the beginning of this section. This difference in the incidence angle, although small in absolute value, is very significant because plasmon resonances are usually very sharp. Second, the thickness one must choose to prioritize absorption over field enhancement (or vice versa) is significantly different. It is a common oversight within the scientific community to, for example, make the calculations using the minimum of the reflection even though the subject of the experiment is associated with the field enhancement. Third, optimizing for maximum field enhancement will result in a non-trivial amount of reflection from the metal film. This is not a contradictory result though. The field enhancement is only localized near the metal's surface

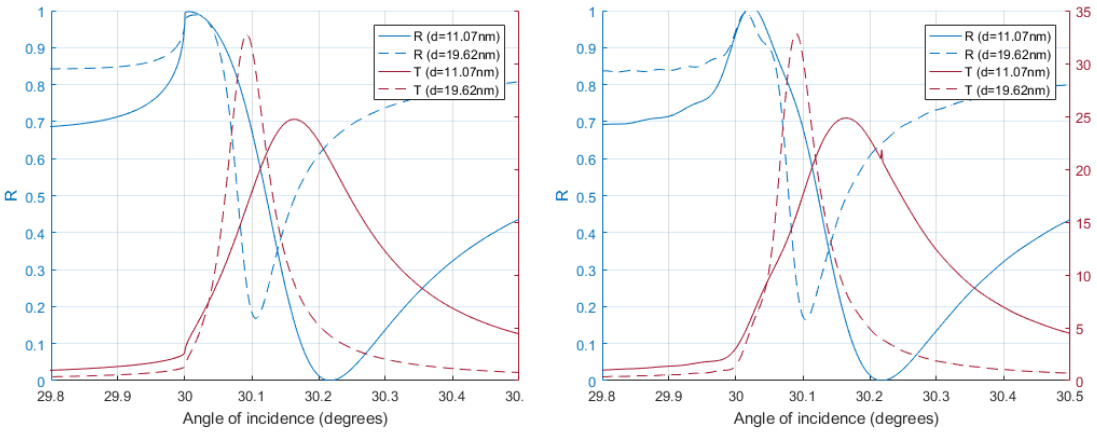


Figure 2.17: Reflection and transmission spectra for aluminum at $\lambda = 1.7\mu m$ using theory (left) and FDTD (right). The results are obtained for two different thicknesses for the aluminum: one optimized for maximum absorption, one for maximum field enhancement.

and it is not related to the power transmission (which is usually very close to zero since the tangential component of the wave vector is larger than $k_0$ in air). On the right panels of Figures 2.16 and 2.17, the theoretical calculations are validated with FDTD simulations. The results are in excellent agreement.

Next, we look at real metals and calculate how significant the difference is between the cases where the setup is optimized for maximum absorption and maximum field enhancement. Figure 2.18 shows the metal thickness optimized for either of maximum absorption or maximum field enhancement. Four different metals, namely aluminum, gold, silver and copper, are used in calculations as these metals are commonly used in plasmonic devices. The solid curves (marked as $R = 0$) show the metal film thicknesses optimized for maximum absorption for each wavelength. (Note that it is possible to obtain complete extinction of the incident wave for any plasmonic structure. This is discussed in the next section.) It is seen that the optimal thickness strongly depends on the wavelength, especially at higher frequencies for gold, silver and copper. The dashed curves (marked as $T = max$) show the metal film thicknesses optimized for maximum local field enhancement at each wavelength. The difference between thicknesses optimized for absorption and field enhancement is significant. This difference is increased for more lossy metals such as aluminum and copper. Figure 2.18 shows the importance of taking this difference into account so that plasmonic devices can be better tailored to their intended applications.

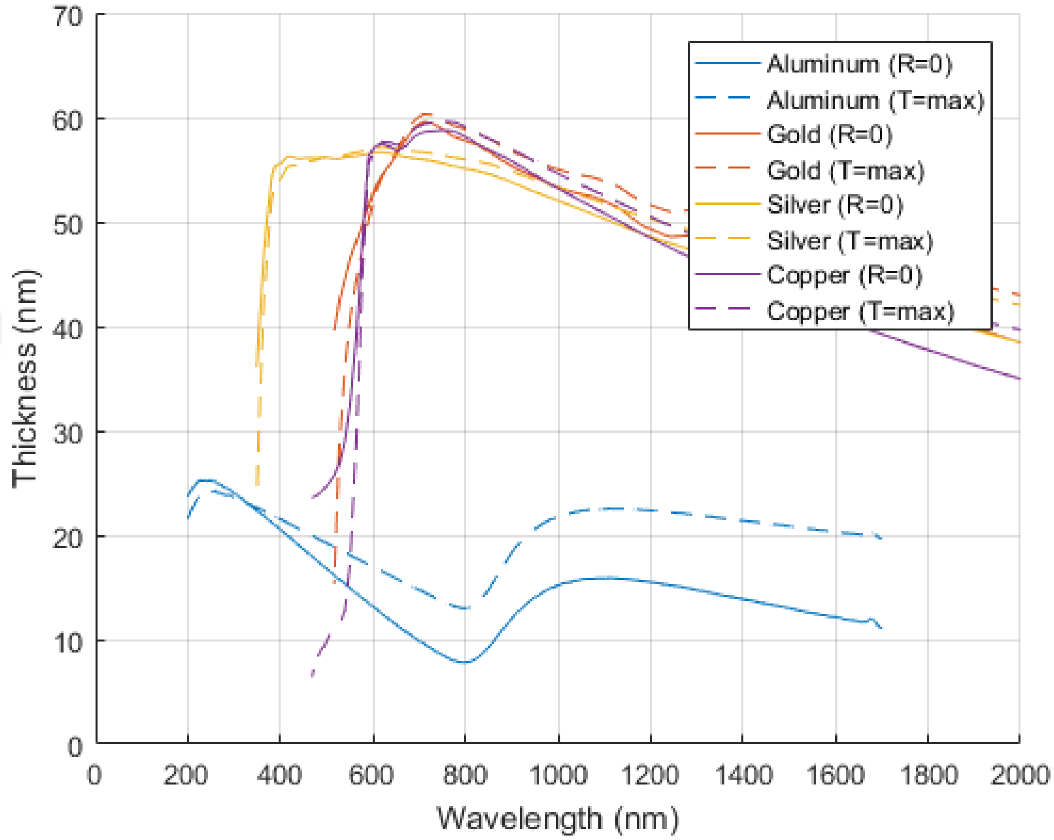


Figure 2.18: Metal film thickness optimized for either maximum absorption or maximum field enhancement. Solid curves (marked as $R = 0$) show the metal film thicknesses optimized for maximum absorption for each wavelength. Dashed curves (marked as $T = max$) show the metal film thicknesses optimized for maximum local field enhancement at each wavelength. The calculations are done for four different metals, namely aluminum, gold, silver and copper using the experimental data for metal permittivities. The metal film thicknesses for maximum absorption and maximum field enhancement are significantly different, especially for more lossy metals. Note that for each point on these curves, the optimal angle of incidence is chosen. These angles are not necessarily the same for different wavelengths, metals, or metal film thicknesses.

Another independent variable is the angle of incidence in experimental setups such as the KRC. We expect to see a similar difference in the angle of incidence as we have seen in the metal film thickness optimized for two distinct purposes. Figure

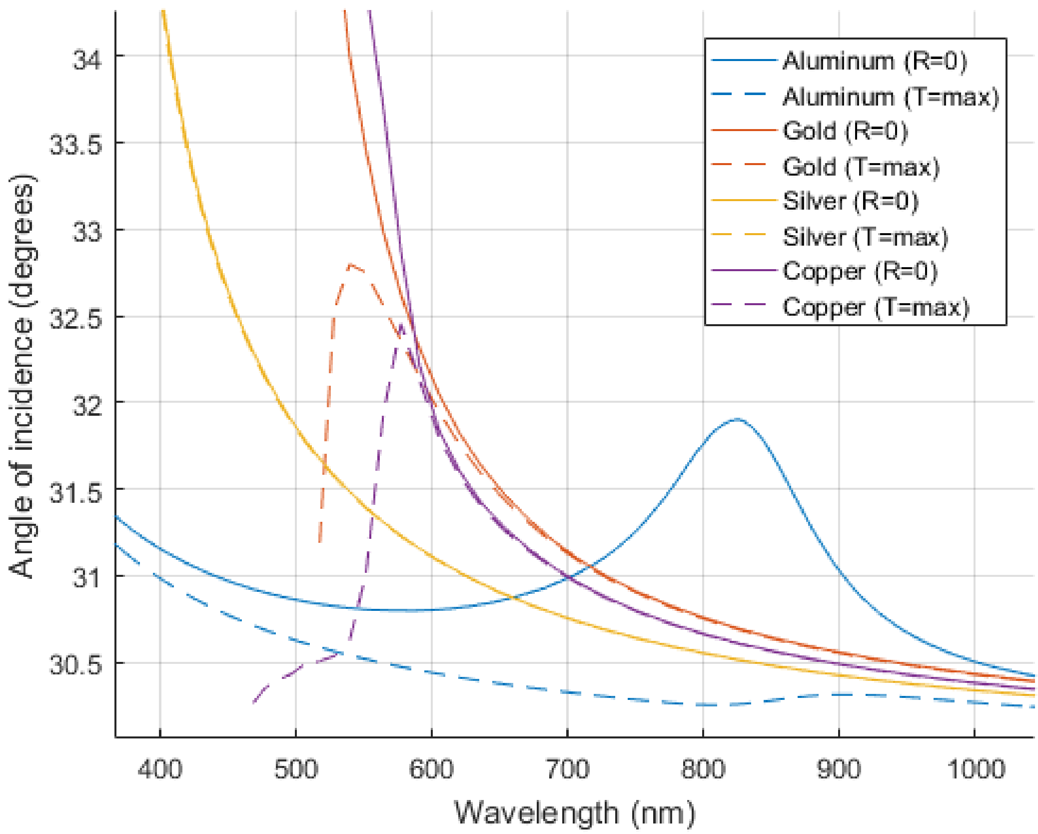


Figure 2.19: Angle of incidence optimized for either maximum absorption or maximum field enhancement. Solid curves (marked as $R = 0$) show the incidence angles optimized for maximum absorption for each wavelength. Dashed curves (marked as $T = max$) show the incidence angles optimized for maximum local field enhancement at each wavelength. The calculations are done for four different metals, namely aluminum, gold, silver and copper using the experimental data for metal permittivities. Note that for each point on these curves, the optimal metal film thickness is chosen. These thicknesses are not necessarily the same for different wavelengths, metals, or incidence angles.

2.19 shows the angle of incidence optimized for either of maximum absorption or maximum field enhancement. Again, the calculations are made for four different metals, namely aluminum, gold, silver and copper. It is clear that the angle of incidences that must be used for the two distinct purposes differ from each other. The angle of incidence is a much easier parameter to adjust in experimental setups, unlike the film thickness which cannot usually be changed after the plasmonic device is fabricated.

Finally, we note the difference between the theoretically calculated parameters to obtain maximum absorption or field enhancement and the experimentally attainable values which are located on the experimental line of the Riemann sheet (see Figure 2.15). Because of the interplay between the zero and the pole on the improper sheet of $\tilde{r}$, the real part of $k_x$ corresponding to the zero does not directly give the optimal angle of incidence for absorption. This has caused confusion in the literature as other studies tried to determine which pole belonged to the SPP and which did not [38, 39, 40, 52]. To resolve this confusion, we calculate the conditions for the reflection minimum and transmission maximum, first, by using the real part of the theoretically calculated $k_x$ locations and, second, by finding the minimum and the maximum of the response of the medium on the experimental line. The results are shown in Figure 2.20. The blue solid curve ($R_{min}$) shows the minimum of the generalized reflection coefficient observed on the experimental line (i.e. attainable using excitations with purely real $k_x$). The red solid curve ($T_{max}$) shows the maximum of the generalized transmission coefficient, again, observed on the experimental line. The dashed yellow line (*zero*) shows the real part of $k_x$ corresponding to the zero in the improper sheet of $\tilde{r}$ (see the bottom inset of Figure 2.15). The purple dashed line (*pole*) shows the real part of $k_x$ corresponding to the pole in the improper sheet of $\tilde{r}$. It is clear that even though all curves follow a similar trend, there are significant differences between them. Our immediate observation is that angles calculated using the experimental line and the exact locations of the extrema do not match. The calculations on the experimental line should act as a guide when designing a plasmonic device. The $T_{max}$ curve closely follows the exact location of the pole throughout the wavelength range. This is expected because there are no zeros in the vicinity of this pole in the improper sheet of $\tilde{t}$, and therefore, the influence of this pole is directly observable on the experimental line. The $R_{min}$ curve follows the location of the zero at small wavelengths (see the left inset). However, the difference between the two curves widens as the zero moves closer to the pole at large wavelengths (see the right inset). This is the main reason for the confusion in the literature: If the system is excited with higher frequencies, then the reflection minimum will appear to follow

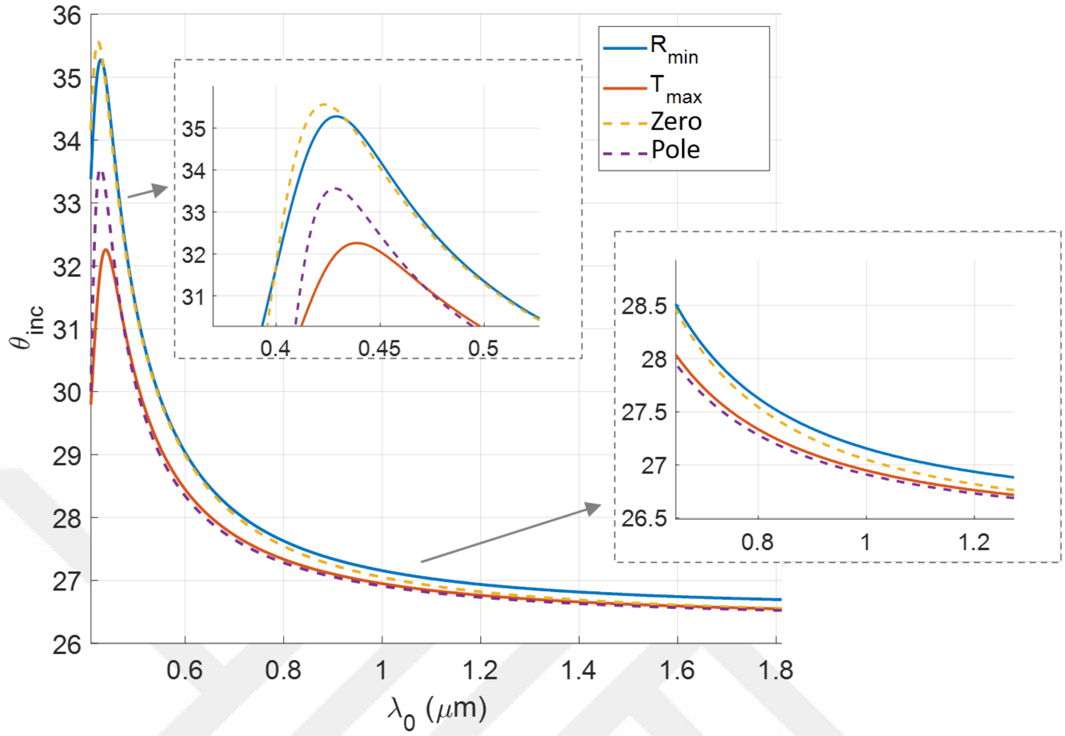


Figure 2.20: Optimal angle of incidence for SPP excitation. The blue solid curve ($R_{min}$) shows the minimum of the generalized reflection coefficient observed on the experimental line (i.e. attainable using excitations with purely real $k_x$). The red solid curve ($T_{max}$) shows the maximum of the generalized transmission coefficient, again, observed on the experimental line. The dashed yellow line (*zero*) shows the real part of $k_x$ corresponding to the zero in the improper sheet of $\tilde{r}$ (see the bottom inset of Figure 2.15). The purple dashed line (*pole*) shows the real part of $k_x$ corresponding to the pole in the improper sheet of $\tilde{r}$

the zero. If the system is excited with lower frequencies, then the reflection minimum will appear to follow the pole. In reality, this is just due to the interplay between the pole and the zero on the improper Riemann sheet. We will confirm in the following sections that the pole and the zero get infinitesimally close to each other as the frequency is lowered. Nevertheless, when the pole and the zero is sufficiently away from each other, the reflection minimum follows the zero in the improper sheet and the transmission maximum follows the pole in the improper sheet.

## 2.4 SPP dispersion and dependence on material properties

In this section, we investigate SPP dispersion and dependence of SPP's features on material properties such as the metal film thickness and the dielectric medium. The discussion around the dispersion requires its own chapter as it is a very rich topic requiring our utmost attention. The intention here is to provide only the basics and leave the detailed discussions to Chapter 3.

### *2.4.1 SPP dispersion*

The dispersion relation for SPPs at a single interface (2-layered media) was discussed in Chapter 1. Now, we discuss the SPP dispersion in multi-layered structures. Computationally, the problem of calculating the dispersion is a matter of tracking the poles and zeros on the Riemann sheet for either $\tilde{r}$ or $\tilde{t}$. In other words, this is a root finding problem.

To derive the dispersion relation for the glass-metal-air structure, we track the pole and the zero in the proper Riemann sheet of the generalized reflection coefficient $\tilde{r}$. The red and blue curves in Figure 2.21 show the frequency (normalized to the plasma frequency $\omega_p$) and the wave vector ($rad/\mu m$) values for the pole and the zero, respectively. The solid curves represent the real part of $k_x$ while the dashed curves represent the imaginary part. It is clearly seen that the pole and the zero have almost the same frequency - wave vector pairs for low frequencies, which is a verification of our observation in Figure 2.20 in the previous section. As the frequency increases, the wave vector increases faster than the light line in air, which should make the SPP more confined to the metal waveguide. Around $\omega = 0.43$, we observe back-bending towards smaller wave vectors and dramatically increased amount of losses. The dispersion curve does not cross the light line in glass at any frequency. This means that a propagating plane wave used as an excitation in the glass medium can be used to excite any SPP on this dispersion curve. The fact that the pole (in the proper sheet) can extend further into higher $k_x$ values also agrees with the observation that the incidence angle for the maximum absorption is larger

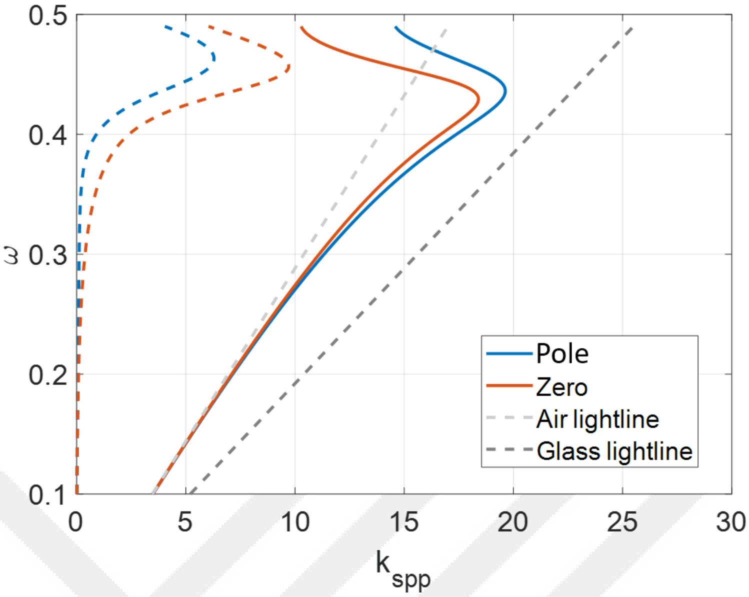


Figure 2.21: Dispersion curve for the KRC (glass-metal-air structure). The red and blue curves show the frequency (normalized to the plasma frequency $\omega_p$) and the wave vector ($rad/\mu m$) pairs for the pole and the zero in the proper Riemann sheet of the generalized reflection coefficient $\tilde{r}$, respectively. The solid curves show the real part of $k_x$ while the dashed curves show the imaginary part.

as seen in Figure 2.20. Note that the pole we are looking at is in the proper sheet; it manifests itself as a zero on the improper sheet near the experimental line (see Figure 2.15).

Next, we plot the field profiles for several SPP modes on the dispersion curve shown in Figure 2.21. We pick 6 different SPP modes starting with low frequencies and going up to the back-bending region. The field profiles for these 6 SPP modes are given in Figure 2.22. The legend shows the frequencies and the relative permittivity of the metal at the given frequency for each field profile. It is seen that the lower the frequency the larger the local field enhancement. This is the result of higher contrast between the metal's and air's permittivity and lower imaginary part of the characteristic wave number $k_x$ of the SPP mode. Although not shown here, the resonance at lower frequencies is much sharper than higher frequencies because SPP modes are less lossy at low frequencies. However, the SPP mode is also much less confined at lower frequencies. The decay rate in the normal direction is particularly slow in the glass region.

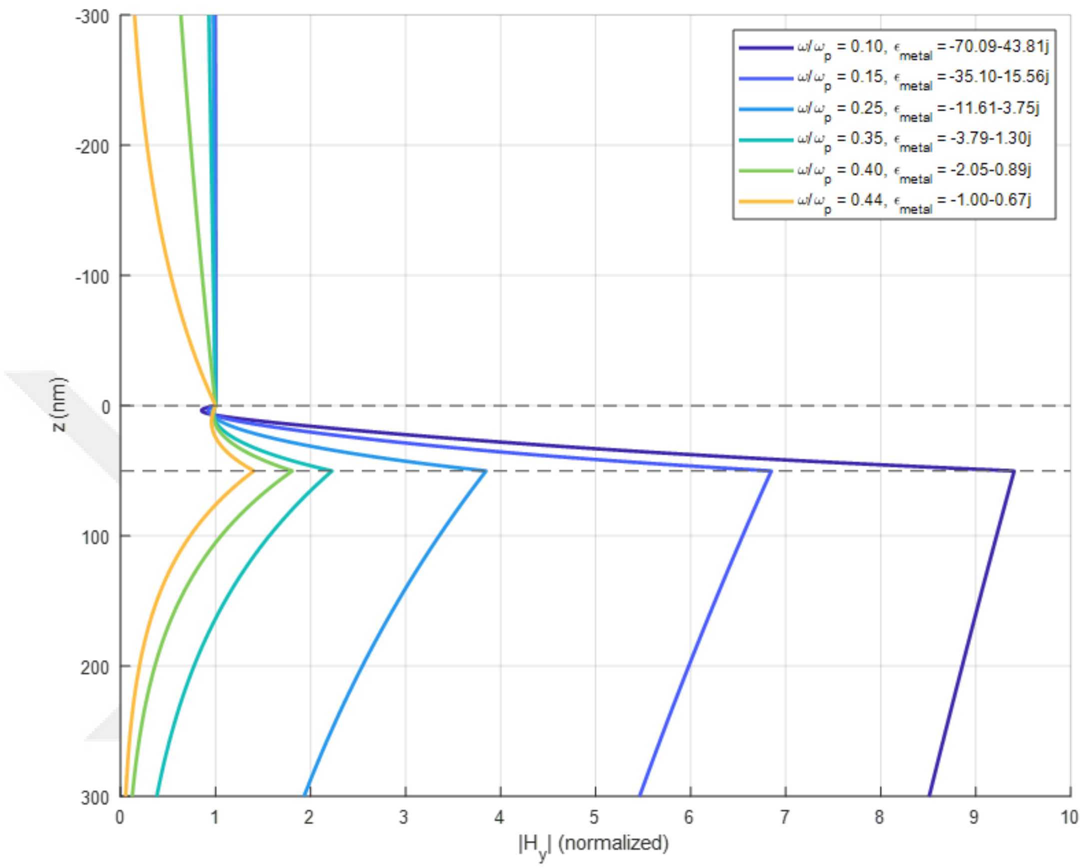


Figure 2.22: Field profiles for SPP modes at different frequencies. Six different SPP modes starting with low frequencies and going up to the back-bending region are selected from Figure 2.21 and plotted. The legend shows the frequencies and the relative permittivity of the metal at the given frequency for each field profile. The frequencies are normalized to the plasma frequency $\omega_p$ and the wave vectors are in units of $rad/\mu m$.

Finally, for a chosen frequency, we plot the field profiles at four different $k_x$ values that were explained in Figure 2.20. These profiles are shown in Figure 2.23. To reiterate, the blue curve ($R_{min}$) corresponds to the minimum of the generalized reflection coefficient observed on the experimental line (i.e. attainable using excitations with purely real $k_x$). The red curve ($T_{max}$) corresponds to the maximum of the generalized transmission coefficient, again, observed on the experimental line. The yellow curve ($zero$) exactly corresponds to the zero in the improper sheet of $\tilde{r}$

(see the bottom inset of Figure 2.15). The purple line (*pole*) exactly corresponds to the pole in the improper sheet of $\tilde{r}$ (again, see the bottom inset of Figure 2.15). It

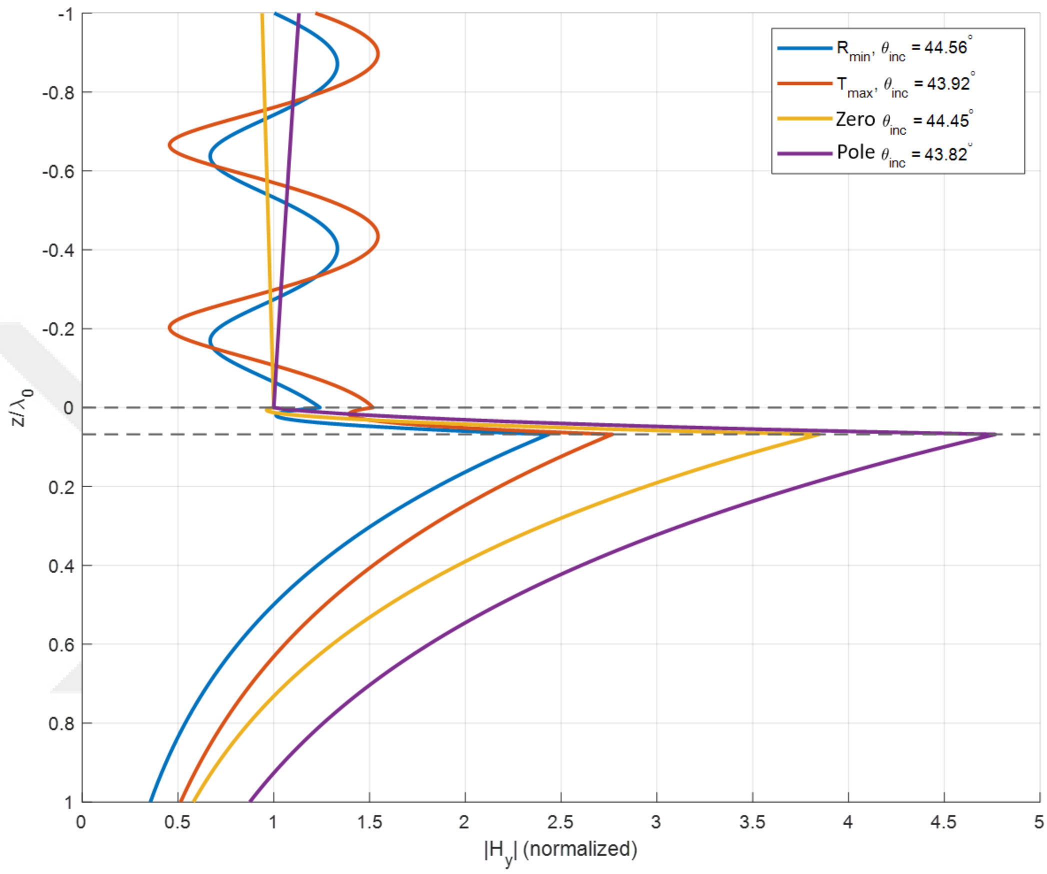


Figure 2.23: Field profiles at the exact pole and zero locations, and at optimal conditions attainable in experimental scenarios. The blue curve ($R_{min}$) corresponds to the minimum of the generalized reflection coefficient observed on the experimental line (i.e. attainable using excitations with purely real $k_x$). The red curve ($T_{max}$) corresponds to the maximum of the generalized transmission coefficient, again, observed on the experimental line. The yellow curve (*zero*) and the purple curve (*pole*) exactly correspond to the zero and the pole in the improper sheet of $\tilde{r}$, respectively (see the bottom inset of Figure 2.15). The angle of incidence is given in the legend for each curve.

is seen that optimizing for absorption results in the least amount of reflection while optimizing for the transmission maximum gives the largest local field enhancement. None of these cases, of course, reach the efficiency of the theoretical limit, that is the *zero* and *pole* curves.

### *2.4.2 Dielectric dependence of SPP modes*

In this section, we look at the dependence of the SPP modes on the dielectric material surrounding the metal film. In particular, we are interested in the dielectric constant of the incidence medium as its optical properties are usually available for tuning in experimental setups such as the KRC or the Otto configuration.

Figure 2.24 shows the dependence of the pole (SPP) and the zero in the proper sheet of the generalized reflection coefficient. The x-axis represents the dielectric constant of the incidence medium. This dielectric constant ranges from 1, making the waveguide symmetric, up to 2.5, which is a typical value for commonly used glasses in KRC experiments. Notice that from $\epsilon_{dielectric} = 1$ to about $\epsilon_{dielectric} = 1.3$,

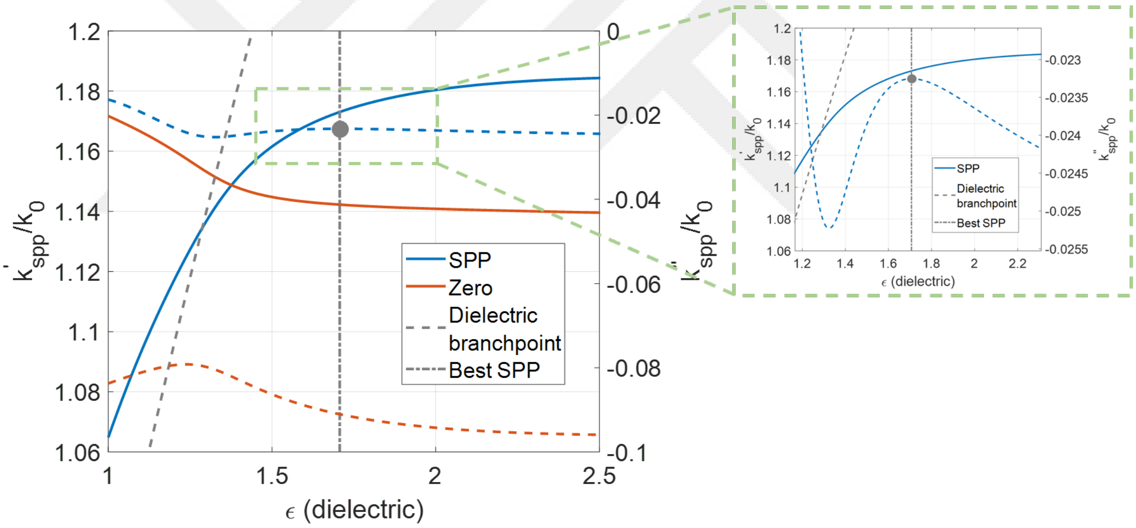


Figure 2.24: Dielectric constant dependence of SPP modes. The wave vector values for the SPP in a glass-metal-air structure, i.e. the KRC, is shown for a range of glass dielectric constants. Solid curves are the real part of $k_x$ (left y-axis), and the dashed curves are the imaginary part of $k_x$ (right y-axis). *SPP* refers to the pole in the proper Riemann sheet of the generalized reflection/transmission coefficient, and *Zero* refers to the zero in the proper Riemann sheet of the generalized reflection coefficient. The branch point in the glass is shown by the dashed gray curve. The vertical dotted-dashed gray line marks the critical value for the dielectric constant which enables the most efficient excitation of SPP in the KRC. The inset is a closer look at the SPP curve near this critical value.

the SPP remains outside the light cone of the dielectric, and therefore, it is impossible to couple to the SPP using a propagating plane wave excitation. After this limit, SPPs can be excited via coupling propagating waves to the metal waveguide from the glass side.

The wave vector of the SPP (the pole in the proper sheet of the generalized reflection/transmission coefficient) is highly dependent on the dielectric constant of the glass for small values. This regime is where the symmetry of the waveguide starts to brake. After the symmetry is lost, at higher glass permittivity values, the SPP wave vector remains relatively unchanged. The physics behind this behaviour is related to the fact that, for small values of $\epsilon_{glass}$, the single interface SPP modes, calculated using equation (1.15), at glass-metal and air-metal interfaces have very similar $k_x$ values. This induces a coupling between these two modes and their behaviour becomes dependent on each other. When $\epsilon_{glass}$ is large, the single interface SPP at the glass-metal interface moves away from the other SPP on the complex $k_x$, essentially removing the coupling between these two SPPs (see Figure 2.8 for an example of this). After these SPPs are decoupled, the SPP excited in the KRC becomes almost independent from the dielectric constant of the glass. On the other hand, the wave vector of the zero in the proper sheet of the generalized reflection coefficient (the red curve) is less affected by a change in the dielectric constant, compared to the SPP/pole.

Another important observation is that there exists an optimal dielectric constant at which the excitation of the SPP mode is the most efficient. The inset in Figure 2.24 provides a closer look at the SPP's wave vector near this critical dielectric constant. It is seen that the imaginary part of $k_x$ has a peak (or a dip in absolute value) indicating a point where the SPP propagation losses are at a minimum. This critical point provides a means for optimizing plasmonic structures for efficient SPP excitation.

Figure 2.25 shows the field profiles for a select number of dielectric constants. The field profile is symmetric when $\epsilon_{glass} = 1$, as expected, reflecting the symmetry of the waveguide itself. Higher dielectric constants break this symmetry but also provide higher field enhancement. However, this field enhancement comes at the cost of confinement in the glass region. Note that the SPPs in the cases where $\epsilon_{glass} < 1.29$ cannot be excited using propagating plan waves, for the reasons explained in Figure 2.24. $\epsilon_{glass} = 1.29$ marks the transition point above which SPPs can be excited in the KRC.

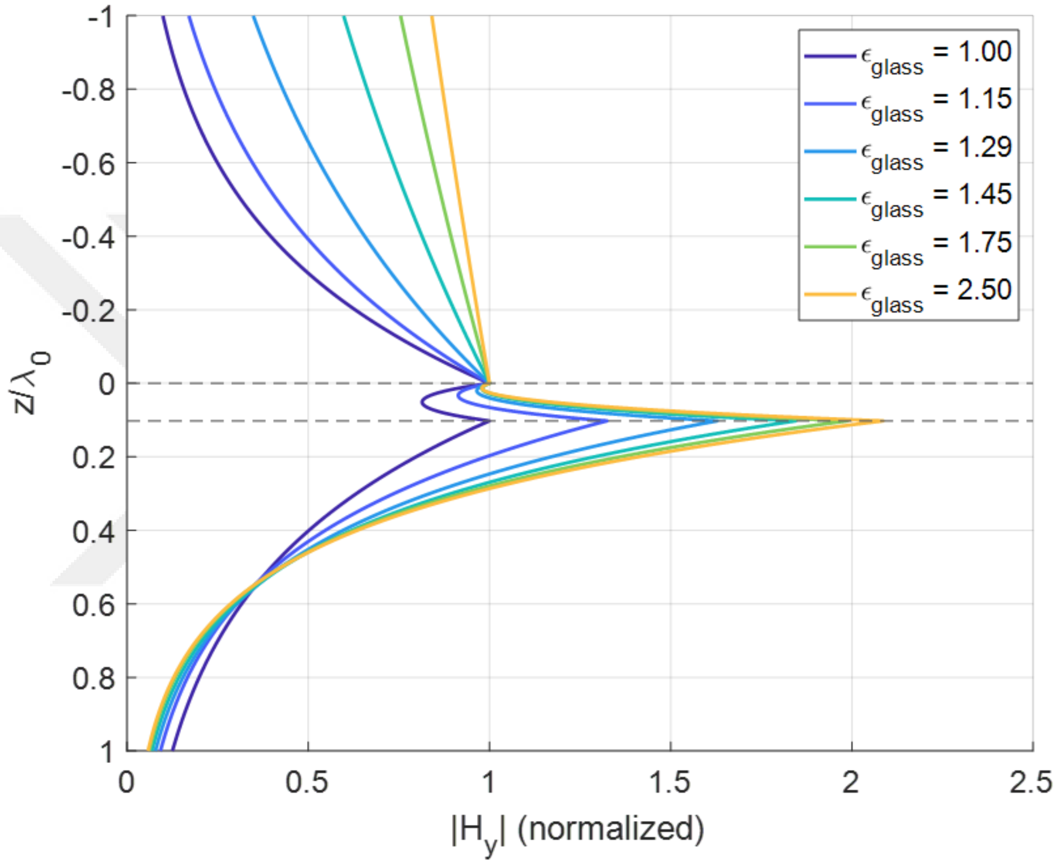


Figure 2.25: SPP field profiles in glass-metal-air structure for different values of glass permittivity.

### *2.4.3 Thickness dependence of SPP modes*

We have looked at the frequency and the dielectric constant dependence of SPPs in previous sections. In this section, we investigate the dependence on the metal film thickness. Figure 2.26 shows how the SPP wave vector changes with metal film thickness. The *SPP* (blue) and the *Zero* (red) curves are the pole and the zero in the proper Riemann sheet of the generalized reflection coefficient, respectively. The

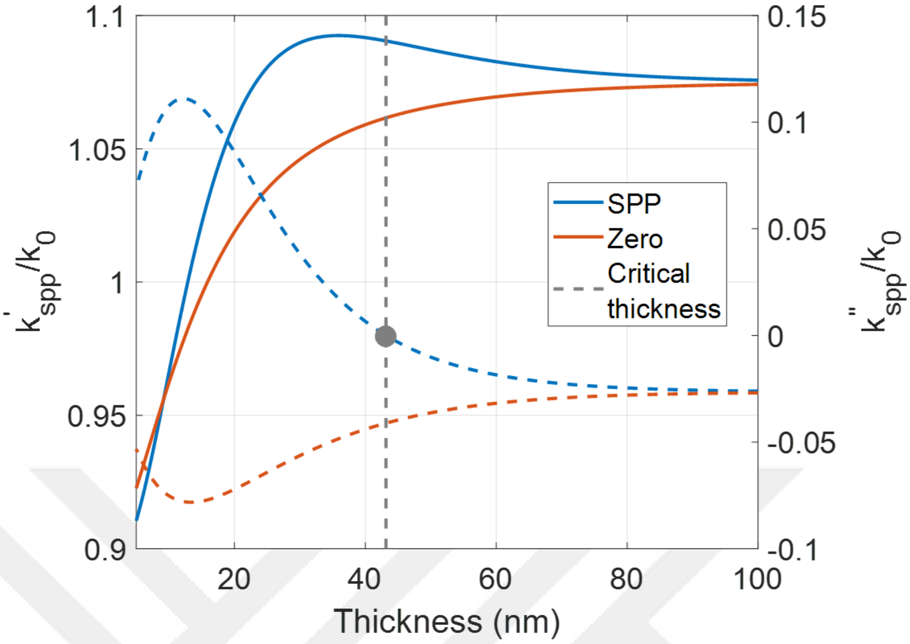


Figure 2.26: Thickness dependence of the long-range SPP mode in glass-metal-air structure. The *SPP* (blue) and the *Zero* (red) curves are the pole and the zero in the proper Riemann sheet of the generalized reflection coefficient, respectively. The solid and dashed lines show the real and imaginary parts of the wave vector $k_x$. The vertical dashed gray line marks the critical thickness at which complete extinction is observed, i.e. the reflection becomes zero.

solid and dashed lines show the real and imaginary parts of the wave vector $k_x$. For very small thicknesses, the pole and the zero have approximately the wave vector values. They diverge at larger thicknesses until they merge back for very large metal thicknesses.

Notice that, for very thin metal films ($< 10nm$ in this case), $k_{spp}$ is smaller than $k_0$, the wave number in air. This means that the SPP is not confined at all, and it becomes arguable whether this is actually an SPP in the conventional sense. We should note that this result is in perfect agreement with the observations and conclusions derived in Section 2.3.6, where we investigated the details of the four regions on the Riemann sheet. Since the SPP has a positive imaginary part $k_x''$, it is indeed in region C shown in Figures 2.13 and 2.14. In this region, modes have a profile fitting a description where the waveguide is illuminated from the incidence medium, but some of the energy leaks into the transmission medium. This is exactly what is implied by the condition $k_{spp} < k_0$.

Maybe the most important observation we can make in Figure 2.26 is that the imaginary part of $k_{spp}$ crosses the $k'' = 0$ on the left y-axis. This means that there is a point at which $k_{spp}$ becomes purely real and propagating waves from the glass side can perfectly couple to SPPs. This point is marked with a vertical dashed gray line. On the other hand, the zero never crosses $k'' = 0$ point and always has a negative imaginary part (decaying). This is also physically meaningful. The zero is responsible for the field enhancement in the plasmonic waveguide, since it manifests itself as a pole near the experimental line on the improper Riemann sheet. If it could become purely real, this would mean that one could obtain infinite field enhancement using propagating plane waves, which is impossible in physical scenarios.

For very thick metals, the pole and the zero converge to the same value, as expected because the top and the bottom interfaces of the metal get decoupled from each other and the SPP itself converges to the two-layered case. Note that in two-layered media, the zero does not exist; it is the result of the multi-layered structure of the waveguide.

Figure 2.27 shows the field profile for several SPPs in waveguides with different metal film thicknesses. Even though larger thicknesses provide higher field enhancement, it becomes prohibitively more difficult to couple to SPP from the other side of a thick metal film.

## 2.5 Numerical considerations

In general, the results found in this chapter rely on the calculation of several formulae including the generalized reflection and transmission coefficients, the electromagnetic fields and power with respect to space, the locations of the poles and zeros in the complex spectral (wave vector) domain, and the fields and the Poynting vector of surface modes. In this short section, we note a few observations and guidelines that make these calculations more tractable and computationally robust.

Due to the nature of its definition, the generalized reflection coefficient $\tilde{r}$ is cal-

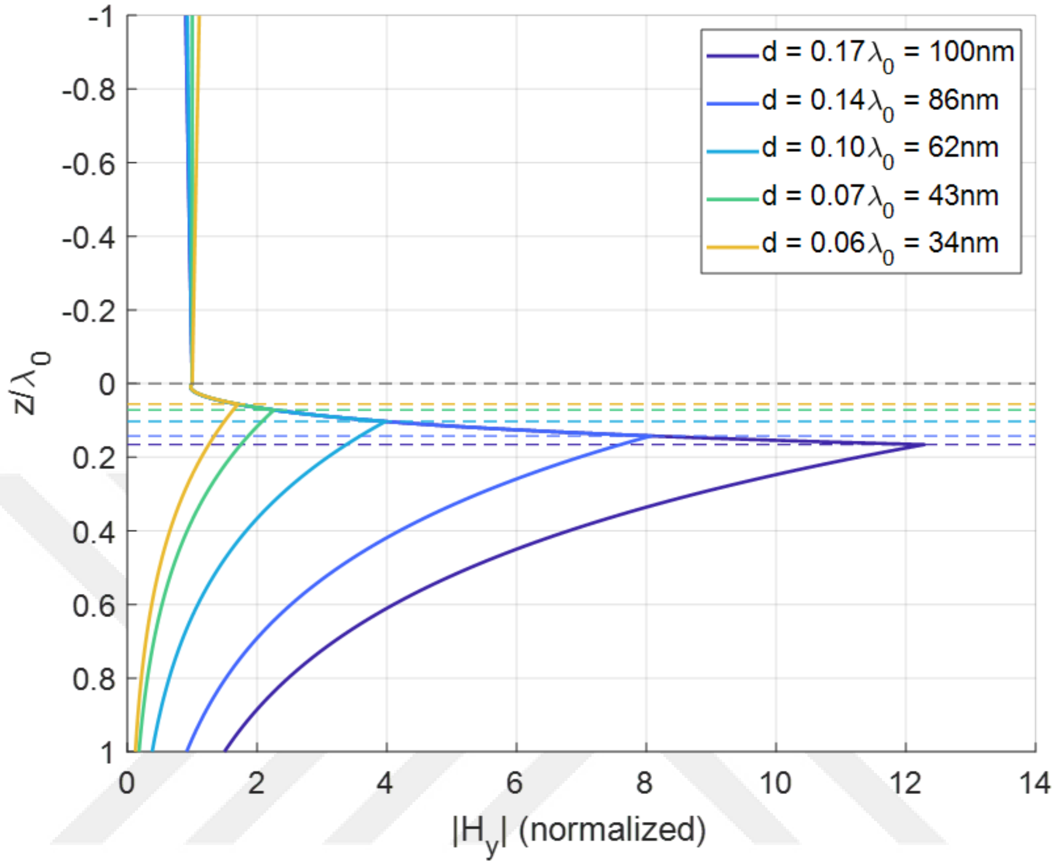


Figure 2.27: Field profiles for several SPPs in waveguides with different metal film thicknesses.

culated by starting with the last/transmission layer and recursively working your way toward the incidence layer. For the last layer $n$, simply the Fresnel reflection coefficient is calculated, which is, in turn, used for calculating the generalized reflection coefficient in the layer $n-1$ above. This procedure is repeated until the top interface is reached. Once $\tilde{r}$ is calculated, one can calculate all fields everywhere in the waveguide. For the first two layers, consider the following expressions.

$$\begin{aligned} &H_2^+ e^{+jk_{z2}d_1} + H_2^- e^{-jk_{z2}d_1} = H_1^+ + H_1^- \\ &H_2^+ \left(e^{+jk_{z2}d_1} + \tilde{r}_2 e^{-jk_{z2}d_1}\right) = H_1^+ \left(1 + \tilde{r}_1\right) \end{aligned} \tag{2.19}$$

For the field amplitudes in the second layer, we can formulate the following expression (2.20) using the field amplitudes in the first/incidence layer. The field amplitude

$H_1^+$ is an arbitrary constant at this point, which can simply be set to unity.

$$H_2^+ = \frac{H_1^+(1+\tilde{r}_1)}{e^{jk_{z2}d_1} + \tilde{r}_2 e^{-jk_{z2}d_1}} \tag{2.20}$$

One can extend this expression for an arbitrary layer $m$ as follows.

$$H_m^+ = \frac{H_{m-1}^+(1+\tilde{r}_{m-1})}{e^{jk_{zm}d_{m-1}} + \tilde{r}_m e^{-jk_{zm}d_{m-1}}} \tag{2.21}$$

There are two important edge cases when calculating the field amplitudes: A zero and a pole. At a zero of the generalized reflection coefficient, one replaces the term $\tilde{r}_2$ in equation (2.20) with 0, and then iteratively calculates the fields for the rest of the layers using equation (2.21) as usual. However, the derivation above will not work if the chosen frequency - wave vector pair corresponds to a pole of these transfer functions (generalized reflection or transmission coefficients). At a pole of the transfer function, there is no longer an incident electromagnetic wave, and therefore the 1 in the term $(1+\tilde{r}_1)$ in equation (2.20) must be set to zero before any fields are calculated. Moreover, since there is no incident electromagnetic wave, $\tilde{r}_1$ can be arbitrarily set to unity.

When finding the zeros and the poles of the transfer function of the plasmonic waveguide, it is preferable to use the generalized transmission coefficient instead of the generalized reflection coefficient. We proved in Section 2.3.5 that the pole representing the long-range SPP is always accompanied by a zero at a very close distance in the complex $k_x$ domain for multi-layered plasmonic structures (see, for example, Figure 2.8). The interplay between these pole and zero makes it difficult for root-finding algorithm to converge to the desired location and prevents the development of a numeric solution that is general enough to work at any frequency or material parameters. Especially for slightly thicker metal films, the pole and the zero get infinitesimally close to each other. However, equation (2.14) shows that the generalized transfer function is absent of any zeros (other than the trivial zero at the branch point of the dielectric). Therefore, we can use the generalized transmission coefficient without these computational issues. Specifically, the poles in the proper sheet of $\tilde{r}$ should be found by directly using the *proper* sheet of $\tilde{t}$. The zeros can in the proper sheet of $\tilde{r}$ should be found by directly using the *poles in the improper* sheet of $\tilde{t}$.

## 2.6 Conclusion

In this chapter, we provided a complete theoretical description of SPP modes in plasmonic waveguides. Starting with a derivation for the response of multi-layered media, i.e. the generalized reflection and transmission coefficients, we analyzed the response of plasmonic structures and extended the analysis to the entirety of the Riemann sheets. We identified multiple extrema determining the response of the plasmonic structures. By using the expressions for the electromagnetic fields and power, we investigated the behavior of these extrema in different regions on the Riemann sheets and also in different layers of the waveguide. The connection between these and the experimental observations was established. Contrary to the common misconception, we showed that all of these extrema play role in the characteristic features of plasmonic systems such as local field enhancement, confinement, resolution and absorption. Finally, in the light of these findings, we investigated the dependence of an SPP's properties on material and other experimental parameters, providing a clear method for optimizing plasmonic structures for various purposes.

Nevertheless, one component of this description is still lacking in-depth analysis, which is the dispersion relation for surface plasmons. We developed some basic understanding of the dispersion of SPP modes in this chapter; however, we will see that SPP dispersion is much richer than commonly thought. The next chapter is entirely dedicated to this topic.

# Chapter 3

## SURFACE PLASMON DISPERSION SURFACE

This chapter is dedicated to studying the dispersion of relation for surface plasmons in layered media. It might appear as if we covered everything related to SPPs in Chapter 2, including the dispersion relation. It is true that we provided a complete description of SPP modes for a given frequency, analyzed how SPPs behaved on the complex wave vector domain and on different Riemann sheets, developed an understanding of the relationship between theory and experiments, and discussed plasmonic device optimization. However, this chapter will show that the dispersion relation provides a much richer solution set that can be exploited for significantly improved plasmonic devices. The path to exploitation of this rich dispersion goes through making use of the time dimension of electromagnetic waves.

Highly lossy nature of metals has severely limited the scope of practical applications of plasmonics. The conventional approach to circumvent this limitation has been to search for new materials with more favorable dielectric properties (e.g., reduced loss), or to incorporate gain media to overcome the inherent loss. In this chapter, however, we turn our attention to the source and show that the wealth of new SPP modes with simultaneous complex frequencies and complex wave vectors that are otherwise unreachable can be excited by imposing temporal decay on the excitation. Therefore, to understand the possible implications of these new modes and how to tune them for specific applications, we propose a framework of pseudo-monochromatic modes that are generated by introducing exponential decays into otherwise monochromatic sources. Within this framework, the dispersion relation of complex SPPs is re-evaluated and cast to be a surface rather than a curve, depicting all possible $\omega - k$ pairs (both complex in general) that are supported by the given geometry. To demonstrate the potentials of the complex modes and the use of the framework to study them selectively, we have chosen two important, and somewhat limiting, features of SPPs to investigate; resolution in plasmonic lenses and propagation length in SPP waveguides. While the former is mainly used to validate the proposed method and the framework on the recent improvement of resolution in plasmonic superlenses, the latter provides a novel approach to extend the propagation length of the SPP modes in planar waveguides significantly. Since the improvement in propagation length due to the introduction of temporal decay to the excitation is rather counter-intuitive, the dispersion-based theoretical predictions have been validated via the FDTD simulations of Maxwell's equations in the same geometry without any a priori assumptions on the frequency or the wave vector.

## 3.1 Introduction

Surface plasmon polariton (SPP) is a coupled electromagnetic and electron wave that propagates along the interface between two dissimilar media, usually dielectric and metal. This harmonious union of electromagnetic wave and electrons, i.e., collective oscillations of surface charge density, is confined to the vicinity of the interface while propagating a rather long distance along the interface, as compared to the SPP wavelength. Therefore, SPPs provide a unique set of features including highly localized energy and enhanced field strength near the interface, rendering it very sensitive to surface structures. As such, SPPs have been quite instrumental to improve devices such as sensors, waveguides, photovoltaic cells, optical microscopes, photodetectors and modulators [53, 54, 55, 1]. Furthermore, SPPs have been proven to be the underlying cause of phenomena such as extraordinary transmission, negative refraction, superlens, and metasurfaces.

Although there are many such applications that SPPs can either facilitate or improve, their practical realizations have been severely limited by high intrinsic loss that naturally exists in metals [10, 56]. To remedy this inherent shortcoming of SPPs, an extensive search for materials with more favorable dielectric properties has already been conducted and is still on-going [57, 56, 58, 10]. In this chapter, however, we shift our attention towards the time signature of the excitation source and study the response of layered plasmonic structures to exponentially decaying but otherwise monochromatic excitations (complex frequency), with a view to mitigate the stated shortcoming. Since the SPPs excited by such sources can be represented by the eigenfunction of $e^{j\omega t - jkx}$, with associated complex eigenvalue pairs $(\omega, k)$, we can still use the frequency-domain approach and obtain the dispersion relation analytically, as it has been the case for monochromatic excitations. The use of a signal with complex frequency as the source does not only lend itself for a well-known and easy-to-use frequency-domain analysis, but also provides a convenient framework to study the effects of a spatio-temporal source and design its time signature for an intended application. Within this framework, the dispersion equation has been re-examined and visualized over the entire complex domains of $\omega$ and $k$ as a *surface*, instead of a curve. As a result, the range of possibilities for dispersion engineering has been dramatically broadened through the excitation of modes on the dispersion surface, allowing one to control and tailor the salient features of SPPs.

Several recent studies have demonstrated that introducing temporal variations to the excitation of the SPPs improves resolution in flat imaging devices [59, 60, 61]. These studies have played a crucial role in demonstrating the importance of time signature of the excitation, yet, they have been rather limited in scope and application because their main focus was the resolution aspect of imaging devices such as the superlens or the hyperbolic lens. In this study, however, we aim to generalize the use of non-monochromatic time varying sources for the excitation of SPPs and to propose a framework that will enable us to select a dispersion curve out of a dispersion surface for better and improved performance criteria, like resolution, propagation length and field enhancement.

## 3.2 Generalized solution to the dispersion relation: the dispersion surface

Although the approach proposed in this work is quite general for planar plasmonic waveguides, for the sake of illustration and with no loss of generality, we have chosen a metal-air-metal structure with two semi-infinite metal layers of the same material and an air gap of $50nm$ in between, as shown in Figure 3.1. Since the SPP modes of layered geometries can be obtained simply by finding the poles of the generalized reflection (or the transmission coefficient) [43, 15], the expression of the generalized reflection coefficient at the air-metal interface is given as

$$\tilde{r} = \frac{-r + re^{-jk_z 2d}}{1 - r^2 e^{-jk_z 2d}} \tag{3.1}$$

where $r$ is the Fresnel reflection coefficient at the air-metal interface, $k_z$ is the normal component of the wave vector in free space, and $d$ is the separation between the two semi-infinite metal layers. Note that, in this study, the relative permittivity of the metal layers $\epsilon_m$ is approximated by the Drude model (3.2), which agrees well up to ultraviolet or visible frequencies with the experimental data for metals such as silver, gold, copper and aluminum [62, 21, 22],

$$\epsilon_m = \epsilon_\infty - \frac{\omega_p^2}{\omega^2 - j\gamma\omega} \tag{3.2}$$

where $\omega_p = 1.04 \times 10^{16}\ rad/s$ is the plasma frequency of the metal, $\gamma = 6.15 \times 10^{14}\ rad/s = 0.059 \times \omega_p$ accounts for the loss in the metal, and $\epsilon_\infty = 4$ is the dielectric constant at very high frequencies ($\omega \gg \omega_p$).

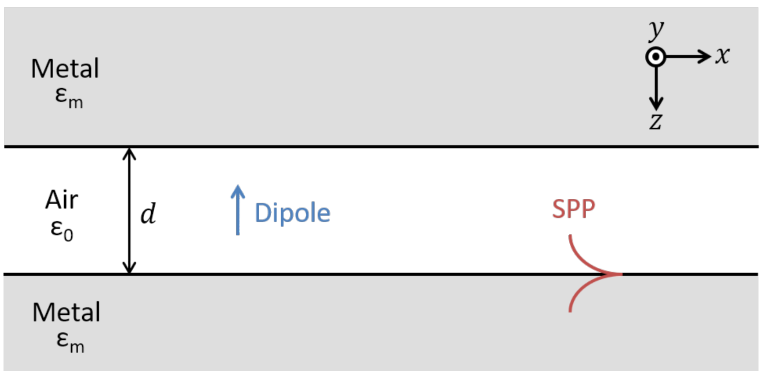


Figure 3.1: A typical metal-insulator-metal plasmonic waveguide. A vertical dipole, placed in the insulator of thickness $d$, is used to excite the SPP modes of the entire wave vector spectrum. At sufficiently large distances away from the dipole along the interface, only the SPP modes would survive as they would be the only modes supported by the waveguide within the frequency range of interest.

In finding the electromagnetic modes of a given structure, the conventional approach has been to find all possible solutions of the associated dispersion relation for either real frequencies or real wave vectors. These two choices result in non-identical dispersion relations with fundamental differences for the same geometry; an observation that was made in the field of plasmonics decades ago [63, 64, 65]. Similar observations have been made in linear chains of metallic nanospheres [66, 67, 68], cylindrical metallic nanowires [69], layered media [70], and grating structures [71, 72]. Indeed, this is not limited to SPPs, and the same situation emerges in photonic crystals [73], bulk polaritons [74], acoustic materials [75] and virtually any real physical problem that gives rise to a dispersion relation. Other discussions on this topic are available in [14, 70]. However, we have to note that, in a few recent studies [61, 76, 60, 59], time-domain signals with non-monochromatic time signatures have been used and shown to improve resolution and enable access to electromagnetic modes otherwise not possible. In this study, our aim has been to provide the basis of these observations, and in turn, to propose a general tool to help select the most suitable dispersion curve for a given application. This has been achieved by allowing both frequency and wave vector to take complex values simultaneously, with the imaginary parts representing temporal and spatial damping, respectively (see Section 3.7 for a discussion on the validity of using complex frequencies in both theoretical and numerical considerations). As a result, a dispersion surface comprising complex SPP modes emerges instead of a simple dispersion curve corresponding to either real frequencies or real wave vectors. Consequently, it has been shown that, due to these complex SPP modes, substantially higher resolution and longer propagation lengths can be realized from the same geometry and materials.

All $\omega, k$ pairs that satisfy the dispersion relation are calculated and displayed as two separate surfaces in Figures 3.2a and 3.2b for the real and imaginary parts of the wave vector, respectively. The color axis represents the imaginary part of the frequency, i.e., the temporal decay rate. For the sake of providing perspective, the conventional dispersion curve, for which real frequencies and complex wave vectors are assumed a priori, is shown by the dashed line at the edge of the dark blue region

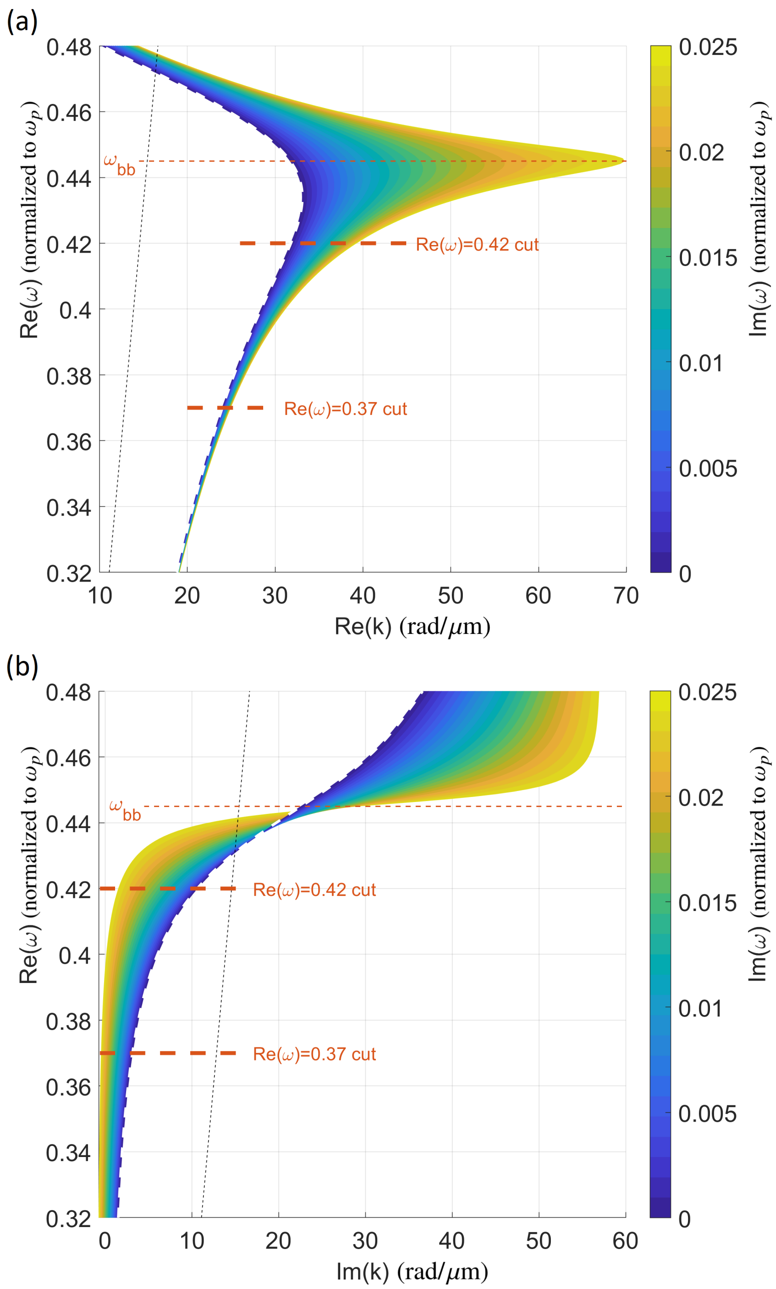


Figure 3.2: The dispersion surface for the metal-air-metal waveguide shown in Figure 3.1. **(a)** $Re(\omega)$ vs. $Re(k)$, and **(b)** $Re(\omega)$ vs. $Im(k)$ for a range of temporal decay rates $Im(\omega)$ represented by the color axis. The dark blue edge of the surface (delineated by a dashed line) corresponds to the case with zero temporal decay, i.e., $Im(\omega)$=0. Please note that, for frequencies below the back-bending frequency $\omega_{bb}$, increasing the temporal decay (towards lighter color in both) leads to larger wave vectors with smaller imaginary part. This is the key finding of this study as it provides an opportunity to improve the resolution and the propagation length of SPPs, which will be elucidated further by investigating the modes along the $Re(\omega)$ = 0.42 and $Re(\omega)$ = 0.37 cuts on the surface (red dashed lines). For the experimental configuration in Figure 3.1, the temporal decay of the SPP modes can be independently controlled by driving the dipole with the desired time signal. The dashed black line is the light cone in free space.

in Figure 3.2.

We identify two main regions on the dispersion surface: $Re(\omega) > \omega_{bb}$ and $Re(\omega) < \omega_{bb}$, where $\omega_{bb}$ marks the frequency corresponding to the tip of the back-bending region. Since, in $Re(\omega) > \omega_{bb}$ region, the imaginary part of the wave vector (Figure 3.2b) increases to prohibitively large values for any practical applications, we focus only on the modes below the back-bending frequency $\omega_{bb}$, where the contributions of this work, namely, the enhancements of resolution and propagation length, are more pronounced and visible. The key observation is, with increasing temporal decay ($Im\{\omega\}$), indicated by the lighter colors on the dispersion surface, the real part of the wave vector ($Re\{k\}$) reaches much larger values compared to the conventional dispersion curve with real frequencies (Figure 3.2a) while the imaginary part of the wave vector moves closer to zero (Figure 3.2b), which are the clear manifestations of better resolution and longer propagation length of the corresponding SPPs, respectively.

The main conclusion that has been derived from the study of dispersion relation in this section can be stated as follows: Sources decaying exponentially in time may excite complex SPPs that have higher resolution and longer propagation length. However, there are two legitimate concerns that need to be addressed, namely 1) if it is valid to use complex $\omega$ and $k$ in the formation of the dispersion surface, rather than the conventional choice of real $\omega$ and complex $k$, and 2) if it is possible to validate longer propagation length for the sources with decaying time signature, as being rather counterintuitive. Moreover, calculation of the propagation length when a temporal decay is introduced to the input signal needs to be re-defined as it should involve both temporal and spatial attenuation; that is, the propagation length can not be as simple as the reciprocal of the imaginary part of the wavevector anymore. Although the first concern can be resolved mathematically by showing that the eigenvalues of the wave equation in open structures are in general complex, both concerns can be alleviated at once by simply solving the same geometry by using a full-wave EM simulator, like those based on Finite Element Method or Finite-Difference Time-Domain method, without any prior assumption on the frequency or the wave vector.

### *3.2.1 Implications of the dispersion surface for SPP resolution, propagation length and lifetime*

In this section, we investigate, in detail, the salient features of the SPPs with temporal decay by using the FDTD simulations of Maxwell's equations, and compare and validate the theoretical results, i.e., the dispersion surface (Figure 3.2). For the FDTD simulations of the waveguide in Figure 3.1, we use Lumerical FDTD solutions [77] and observe the fields starting at a sufficiently large distance away from the dipole in order for the SPPs to be the only remaining wave in the waveguide. Once all the field components are collected over both time and space along the propagation direction, we use a numerical method, based on the generalized pencil of function (GPOF) method, to extract the frequency and the wave vector of the propagating SPP modes (see Methods) [78].

For the sake of elucidating the perceived improvements in the features of the SPPs upon studying the dispersion surface, we have chosen two samples of $Re(\omega)$: $Re(\omega) = 0.42$ for higher frequencies closer to $\omega_{bb}$ and $Re(\omega) = 0.37$ for lower frequencies away from $\omega_{bb}$, as delineated in Figure 3.2. The characteristics of the modes at both frequencies are analyzed in detail, both theoretically and using the FDTD simulations, and their improvements upon introducing temporal loss into the system have been demonstrated.

The resolution of an SPP is directly related to the real part of its wave vector along the propagation direction. If the wave vector is large enough that the wavelength of the SPP is comparable or smaller than the dimensions of an irregularity near or at the interface, the SPP fields scatter in measurable amounts and can be detected with a proper experimental setup. For the modes of interest, namely those corresponding to $Re(\omega) = 0.37$ and $Re(\omega) = 0.42$, the real part of the wave vector vs. temporal loss $Im(\omega)$ is given in Figure 3.3(a), where the agreement between the theory and the FDTD simulations is excellent. For both frequencies, the resolution increases with increasing temporal decay, as expected. While it is relatively small for modes corresponding to $Re(\omega) = 0.37$, we see more than 20% improvement in the resolution for the modes with $Re(\omega) = 0.42$. As also seen in the dispersion surface, the theoretical upper limit on resolution, which can be attained by introducing temporal decay to the excitation, grows with the real part of the frequency. For the range of frequencies shown in the dispersion surface, it is possible to more than double the resolution near the back-bending region.

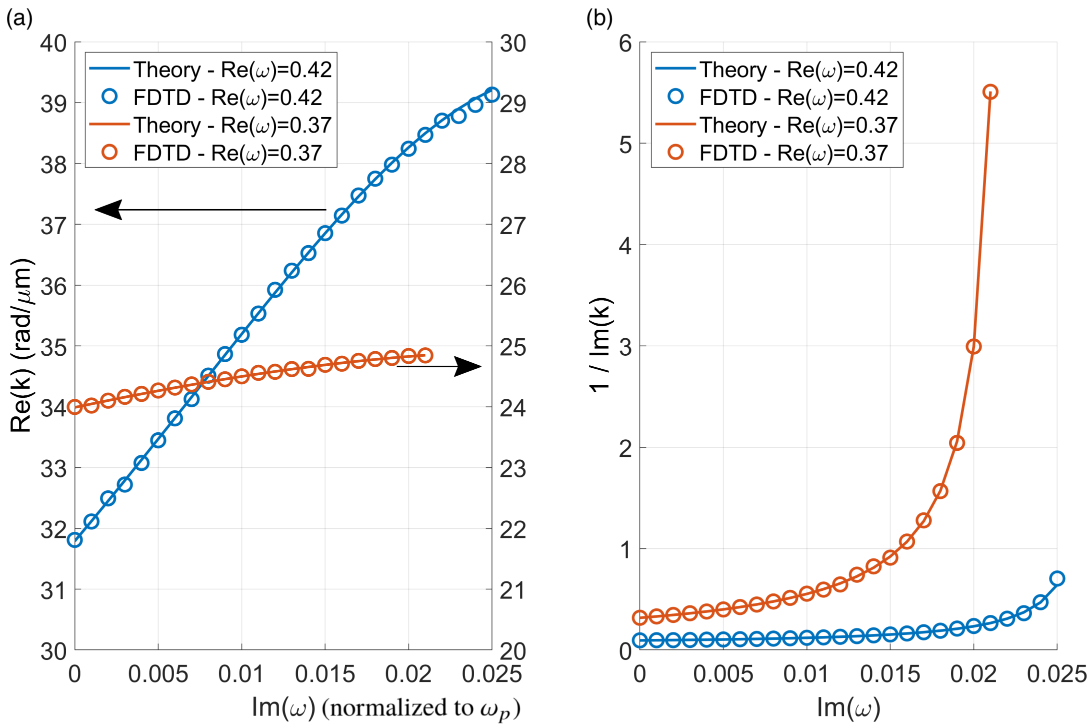


Figure 3.3: Salient characteristics of the SPPs excited in the metal-air-metal waveguide (Figure 3.1) for the frequencies of $Re(\omega) = 0.42$ and $Re(\omega) = 0.37$. An excellent agreement between the theory and the FDTD simulations is observed for all metrics. **(a)** The plot of $Re(k)$ vs. $Im(\omega)$ demonstrates a significant improvement in resolution, especially at $Re(\omega) = 0.42$, with the increase of temporal decay. The left and right y-axes are for the $Re(\omega) = 0.42$ and $Re(\omega) = 0.37$ curves, respectively. **(b)** The plot of $1/Im(k)$ vs. $Im(\omega)$ demonstrates an increase in the propagation length of the SPP. Especially for $Re(\omega) = 0.42$, it is more than an order of magnitude compared to the time harmonic case ($Im(\omega) = 0$). However, note that $1/Im(k)$ loosely represents the propagation length for non time-harmonic cases, for which the effective propagation length is shown in Figure 3.5.

Another feature of the SPPs that is crucial for applications is its lifetime, which is proportional to the reciprocal of the imaginary part of the frequency. Since we have used the same temporal decay rates at both frequencies, $Re(\omega) = 0.42$ and $Re(\omega) = 0.37$, their lifetimes obtained from the simulations are expected to coincide with each other, and moreover, to be in good agreement with the theory, both of which are demonstrated in Section 3.2.2.

The reciprocal of the imaginary part of the wave vector, $1/Im(k)$, is usually associated with the propagation length. As a key part of this study, it is given in Figure 3.3(b), demonstrating an excellent agreement between the theory and the simulations. It is important to note that $Im(k)$ decreases with increasing temporal decay, and it appears as if the propagation length can be increased by an order of magnitude. However, the definition of $1/Im(k)$ (or $1/Im(2k)$ to be precise) as the propagation length is only valid for the time-harmonic excitations where the attenuation of the wave is attributed solely to the spatial decay. For the SPP modes with complex frequencies, which experience *temporal decay* in addition to the spatial attenuation, one must take into account the *propagation time*. Therefore, defining an effective propagation length $l_{eff}$ is in order, as we would like to compare our results against the time-harmonic case. Since an SPP mode on the dispersion surface (Figure 3.2) has indeed a single complex frequency, we can write it in the form of $e^{j\omega t - jkx} = e^{j\omega' t - jk' x} e^{-\omega'' t - k'' x}$ where single and double primes represent real and imaginary parts, respectively. Hence, one can define the effective spatial decay parameter $\alpha$ by simply equating the amplitude of this expression to $e^{-\alpha x}$, resulting in

$$l_{eff} = \frac{1}{\alpha} = \frac{v_{spp}}{\omega'' + k'' v_{spp}} = \frac{\omega'}{\omega'' k' + \omega' k''} \tag{3.3}$$

where $v_{spp}$ is the propagation velocity of the SPP along the interface, and can be calculated directly from the dispersion relation.

For the sake of validating the theoretical effective propagation length given in (3.3) and the conclusions drawn from it, we obtain the propagation length from the FDTD simulations as follows: i) calculate the envelope of the SPP fields in time domain, and ii) track a selected point on the envelope as it propagates along the waveguide. To elucidate, an example is provided in Figure 3.4, where the waveguide is first excited by a time-harmonic excitation, and upon reaching its steady-state, the temporal decay is introduced on the excitation that excites the SPP with the complex frequency of $0.42 + 0.025j$. Then, we select a point in the exponentially decaying region (shown in purple) and measure how much it decays as it propagates, Such a measurement from the simulation results can be used to deduce the effective propagation length.

As the effective propagation length has been well-defined in cases of non-monochromatic excitations, both in theory and in the FDTD simulations, their comparisons provide additional validation for the assessment of longer propagation length when temporal loss is introduced, as shown in Figure 3.5. It is observed that the effective propagation length, $l_{eff}$, is approximately doubled for both frequencies ($Re(\omega) = 0.42$ and $Re(\omega) = 0.37$) over the range of $Im(\omega)$ analyzed in this study, and it can lead to orders of magnitude increase in the field enhancement depending on the distance between the excitation and the observation points. Further improvement is also possible with larger temporal decay rates; however, it becomes increasingly difficult to simulate rapidly-changing amplitudes by the FDTD method. Notice that the doubling of the effective propagation length is in contrast with the ten-fold improvement one would expect from Figure 3.3(b). Since the finite lifetime of SPPs partially counteracts this improvement, it is critical to take both the wave vector and the frequency into account in order to study the propagation characteristics of complex SPP modes. As an illustration, a detailed propagation movie of a complex SPP mode selected from Figure 3.5 is provided in Supplementary Movie C.1.

### *3.2.2 Comparison of the complex frequencies in theory and FDTD*

In Figure 3.3, the theoretical values for the wave vectors of the SPPs are compared to the simulation results. In this section, we further compare the complex frequencies between the theory and the simulations. Even though the frequency is an input to the system, which we can arbitrarily define, it is important to validate that the complex frequencies used in our theoretical calculations are indeed the fre-

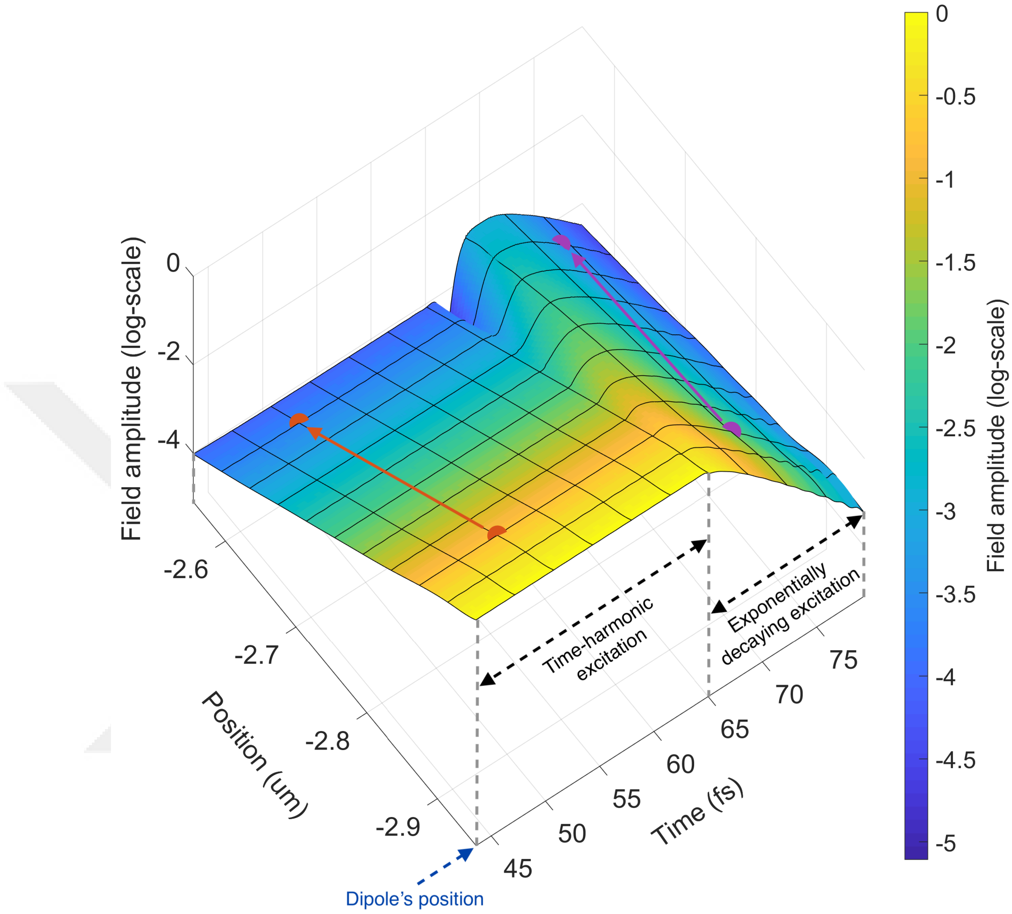


Figure 3.4: Calculation of the effective propagation length of the SPP from the FDTD simulation results. The vertical electric dipole, positioned within the plasmonic waveguide as shown in Figure 3.1, first excites the waveguide with a time-harmonic signal ($\omega = 0.42 + 0j$). After the system reaches the steady-state, the temporal decay is introduced and the SPP with a complex frequency of $0.42+0.025j$ begins to propagate within the waveguide. A point is selected on the SPP's field profile and its amplitude is observed after some time, as shown with the purple dots and arrow. The ratio of the initial and the final amplitudes can be used to calculate the effective propagation length $l_{eff}$. For comparison, we have also included the equivalent path for the steady-state case, shown in red, which coincides with the constant-time lines of the black grid, while the complex frequency path is tilted. This is because one needs to take both time and space into account for temporally varying field profiles, whereas time does not matter for time-harmonic waves as the field is constant for all times at a given position. All measurements are made long after switching from time-harmonic to complex frequency excitation.

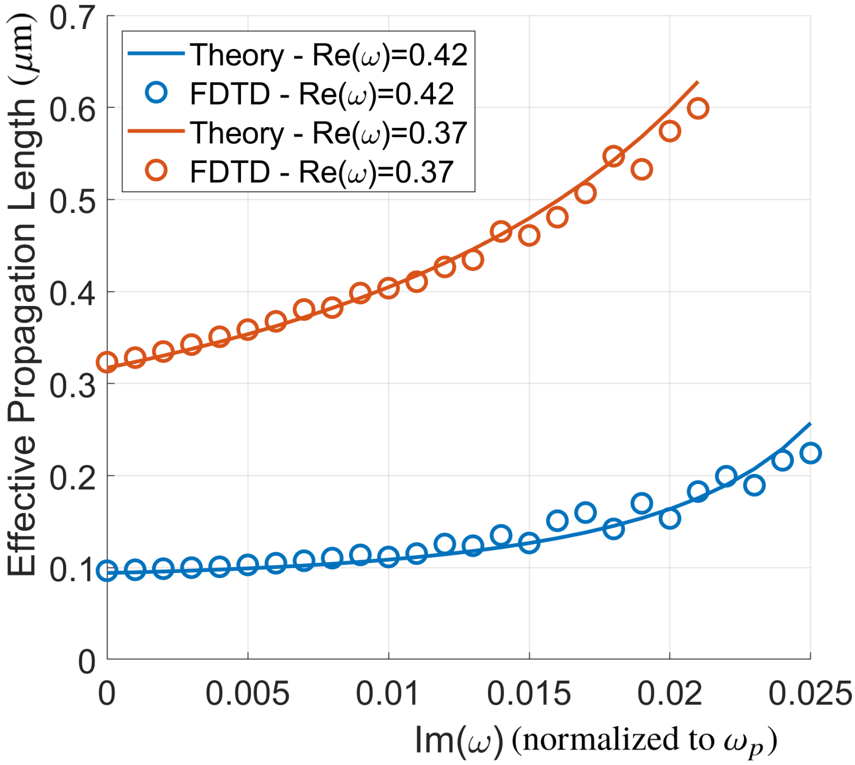


Figure 3.5: Effective propagation lengths vs. temporal loss for the modes along the $Re(\omega) = 0.42$ and $Re(\omega) = 0.37$ cuts on the dispersion surface (Figure 3.2). The theoretical curves, obtained from equation (3.3), and the FDTD results, calculated as explained in Figure 3.4, are in good agreement for all values of $Im(\omega)$. Increasing the temporal decay results in longer effective propagation length for both frequencies while the lower frequency SPPs ($Re(\omega) = 0.37$) propagate much further than the higher frequency SPPs ($Re(\omega) = 0.42$). Further improvement is possible with faster temporal decay rates. The slightly larger variations at higher $Im(\omega)$ values are due to the numerical noise caused by rapidly-changing amplitudes in the FDTD simulations.

quencies excited in the FDTD simulations by the waveform shown in Figure 3.14. Note that, similar to the wave vector measurements, the frequency measurements in FDTD simulations are made away from the source and long after the exponential decay starts. Figure 3.6 shows that there is excellent agreement between theoretical values and the FDTD measurements. This result verifies that the fields are pseudo-monochromatic and propagate with a single complex frequency.

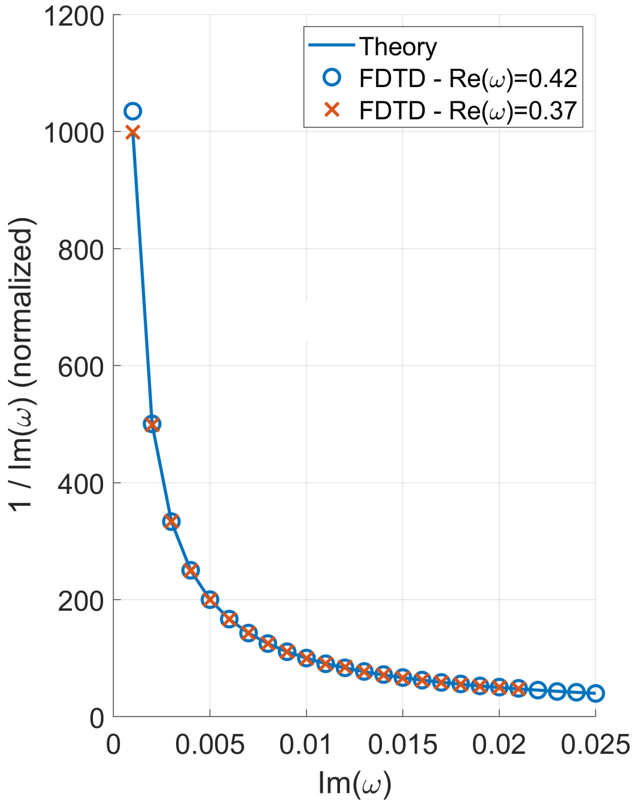


Figure 3.6: The comparison of the complex frequencies used in our theoretical calculations and those excited in the FDTD simulations. It is seen that the frequencies extracted from FDTD simulations using GPOF method (symbols) coincide with the theoretically used values (solid line). This indicates that the fields in the waveguide propagate with the complex frequency corresponding to the tail of the waveform shown in Figure 3.14.

### 3.3 Experimental methods and their relation to the dispersion surface

Historically, the first theoretical and experimental investigations involved fast electron beams that excite SPPs on metal surfaces upon impact [30, 31, 32]. Later, two similar methods were proposed by Otto [24] and Kretschamnn [23], which use light instead of electrons. (An overview of the historical development of SPPs is available in the literature [79]). Although both light and electrons can be used to excite SPPs supported by the same structure, Arakawa et al. realized that these two methods essentially gave different dispersion curves which predict different limits on resolution and confinement of the SPP [63]. As followed in the discussions by Alexander et al. [64] and Kovener et al. [65], even the light excitation alone can be interpreted in two different ways that result in different dispersion curves.

In the previous sections, it has been demonstrated that any dispersion curve obtained analytically from (3.1) (e.g. using real frequencies) is a subset of the more general and all inclusive dispersion surface. This is demonstrated in Figure 3.7. However, in experimental studies of the KRC, the excitation is a plane wave propagating in a lossless dielectric. This type of excitation always has a real $\omega$ and a real $k_x$ for which there is no solution that satisfies the dispersion relation. In other words, the (real $\omega$, real $k_x$) points can only partially excite the closest SPP modes on the dispersion surface defined on the (complex $\omega$, complex $k_x$) space. The closest SPP mode may not necessarily be on the *real* $k_{spp}$ or *real* $\omega$ dispersion curves, and consideration of the other modes on the dispersion surface may be required. In this section, this is demonstrated with a numerical simulation.

The following three experimental setups are considered: (i) the KRC, (ii) vertical electron beam excitation, (iii) parallel electron beam excitation, as shown in Figs. 3.8a, b and c, respectively. The focus of this numerical experiment is the KRC; the electron beam methods were discussed in Chapter 1 where the connection between the electron beam and the excited SPP is established.

In order to construct a dispersion curve from the KRC experiment, one might fix the frequency while searching for the minima of the reflectance over a set of

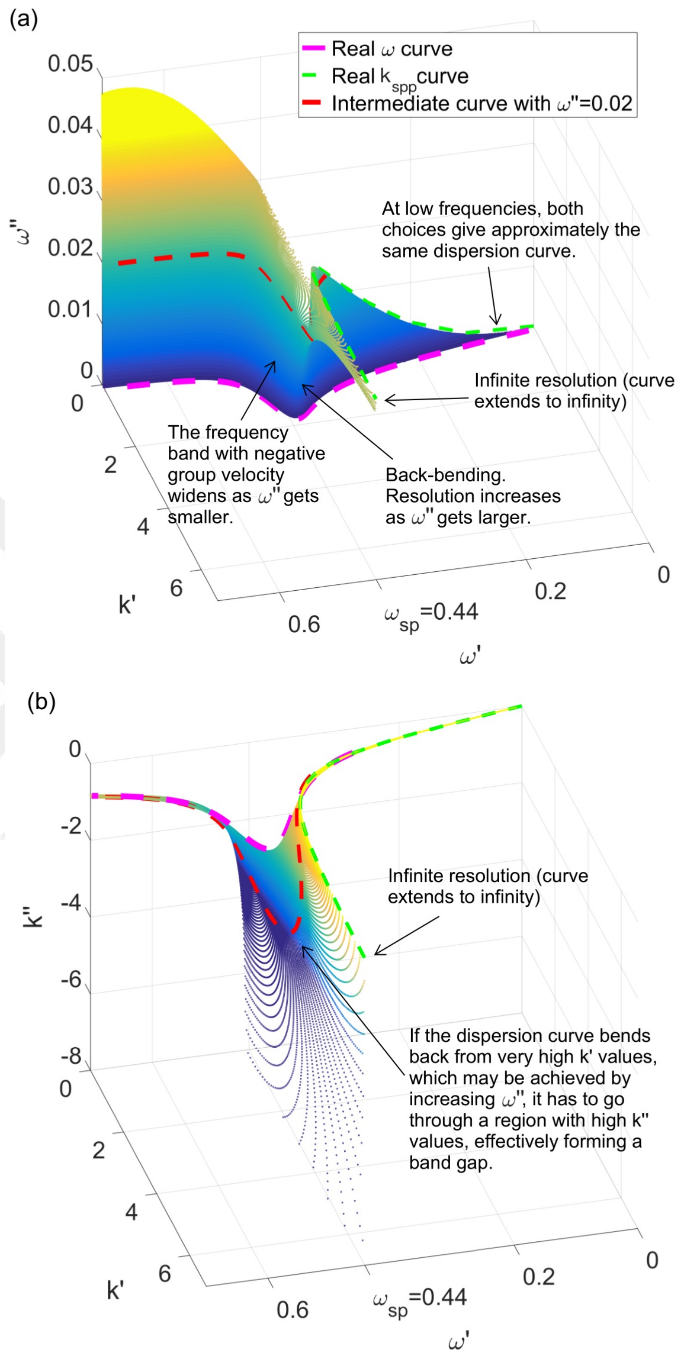


Figure 3.7: Surface plasmon dispersion surface for the air-metal interface shown in three dimensions with annotations of interesting regimes that can be exploited for different applications (c.f. Figure 3.2). The imaginary part of the frequency **(a)** and the imaginary part of the wave vector **(b)** are shown as the functions of the real parts of the frequency and the wave vector. The green curve is the *real* $k_{spp}$ solution where $k_x$ is assumed to be purely real when solving the dispersion equation. The magenta curve is the *real* $\omega$ solution where $\omega$ is assumed to be purely real when solving the dispersion equation. These curves are seen simply as the two subsets of the dispersion surfaces. An intermediate solution for $\omega'' = 0.02$ is also shown in red for comparison. Significant features are indicated on the figure with black arrows and explanatory comments (also see supplementary video C.2).

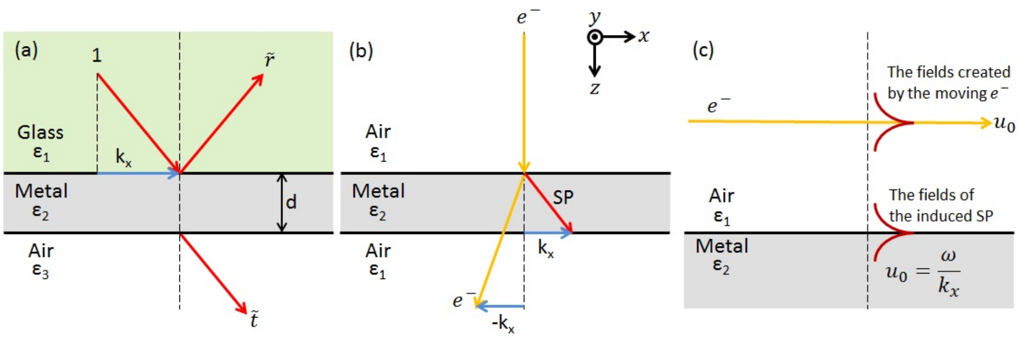


Figure 3.8: Different SPP excitation methods: (a) Kretschmann-Raether configuration (KRC), (b) vertical electron beam, and (c) parallel electron beam configurations. These experimental setups were discussed in Chapter 1.

angles of incidence (fixed-$\omega$ method), or fix the angle of incidence while searching for the minima over a range of frequencies (fixed-angle method), repeating the whole process for a range of frequencies or angles of incidence, respectively. In addition, one might also scan the excitation frequency for a fixed wave vector $k_x$ (fixed-$k_x$ method). Note that the fixed-$k_x$ method is not the same as the fixed-angle method, in which the ratio of $\omega$ to $k_x$ is kept constant (analogous to the parallel electron beam in Figure 3.8c).

Following the above procedure for real $\omega$ and real $k_x$, as dictated by the experiment, the dispersion curves have been obtained with the following features: (i) For the fixed-$\omega$ method, the dispersion curve has back-bending limiting the resolution to a maximum finite value; (ii) for the fixed-angle method, it shows no back-bending, implying $k_x$ asymptotically approaches infinity [63, 64, 65]; (iii) for the fixed-$k_x$ method, it shows no back-bending but is different from the one obtained for the fixed-angle method.

In order to elucidate the differences between the experimental dispersion curves and the theoretical dispersion surface, the fixed-$\omega$, fixed-angle and fixed-$k_x$ paths have been numerically implemented in the KRC and their solutions, the $(\omega, k_{spp})$ pairs, are compared to the exact solutions on the dispersion surface. It should be emphasized one more time that, in the experiments, no matter which parameter is fixed and which one is scanned, the search is always on the (real $\omega$, real $k_x$) plane, as dictated by the experimental setup. For this numerical experiment, a small portion of the dispersion surface is focused on with the three paths (blue for fixed-$\omega$, red for fixed-$k_x$ and green for fixed-angle) passing through a single point on the surface, namely $\omega = 0.65$ and $k = 1.1$, as shown in Fig. 3.9. Since the portion of the dispersion surface is viewed from the top, hiding the z-axis ($\omega''$ in Fig. 3.9a and $k''$ in Fig. 3.9b), the light (yellow) colors denote the higher values of z while the dark (blue) colors correspond to the lower values. Over each path, the reflectance is calculated and its minimum, where coupling of the excitation to the SPPs is the most efficient, is marked with a circle of the same color. These circles represent the experimental $(\omega, k_{spp})$ result over the path. It is seen that the circles are neither on the dispersion surface nor coincide with each other. Moreover, it is noteworthy that the solution over the fixed-$\omega$ path (blue vertical line) gives a point (blue circle) that does not match the real $\omega$ choice even though it intersects the dispersion surface at the $\omega'' = 0$ plane (the dark blue edge of the dispersion surface in Fig. 3.9a). This result contradicts the common assumption in many KRC studies that the experimental fixed-$\omega$ path corresponds to the *real* $\omega$ analytical solution.

Consequently, this numerical example verifies the earlier discussion that the experimental methods do not provide any of the two traditionally used solutions (the *real* $\omega$ and real *real* $k_{spp}$ choices) or any other solution on the dispersion surface. These observations further emphasize the importance of the dispersion surface in understanding the underlying differences between different experiments and analytical solutions of the dispersion relations.

## 3.4 Application of the dispersion surface to the superlens

Superlens structures are, in general, made out of metamaterials with negative permittivity and permeability, and provide resolving power beyond the conventional diffraction limit of $\lambda/2$. Moreover, plasmonic structures, as simple as a thin metal film, can also display superlens properties in the nearfield where the electrostatic approximation holds [80]. In this section, we analyze a Superlens structure of the

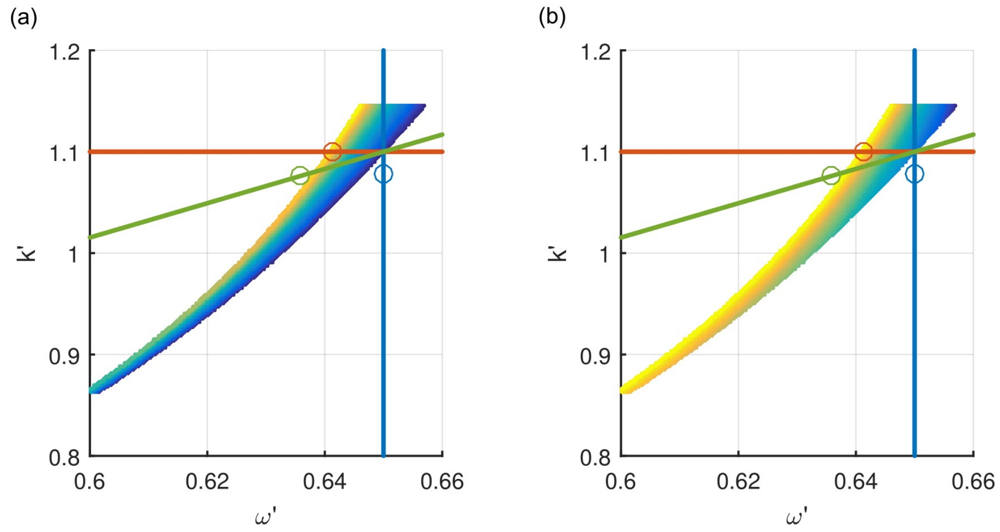


Figure 3.9: A small portion of the dispersion surface for the KRC viewed from the top for $\omega''$ (a) and for $k''$ (b). The light colors denote the higher values while the dark colors correspond to the lower values for $\omega''$ and $k''$. The overlying three experimental paths (blue for fixed-$\omega$, red for fixed-$k_x$ and green for fixed-angle) pass through a single point on the surface ($\omega = 0.65$ and $k = 1.1$).

latter type within the pseudo-monochromatic framework and show that its resolving power can be improvedby using the dispersion surface concept. For the sake of illustration, we have used a layered air-silver-air geometry with a silver slab of thickness $20nm$, for which we have fitted the Drude model (3.2) to the experimental data of silver within the $327-407nm$ range, where $\omega_p = 1.64 \times 10^{16}\ rad/s$, $\gamma = 1.36 \times 10^{14}\ rad/s$, $\epsilon_\infty = 7.45$ [21]. On one side of the slab, a point source (a vertical electric dipole) is positioned $20nm$ away from the lens, while the fields of the image are observed $20nm$ away from the interface on the other side.

Following the same procedure we outlined for the MIM waveguide, we have calculated the dispersion surface for the superlens, as shown in Figure 3.10a. Notice that the dispersion surface consists of two distinct regions corresponding to the two SPP modes supported by the insulator-metal-insulator (IMI) structure. The low frequency mode extends to very large values of $k$, making up the high spatial frequency components required for a high resolution image. As such, the backbending tip corresponds to the operating frequency of the superlens ($\omega_{lens}$) where the per-

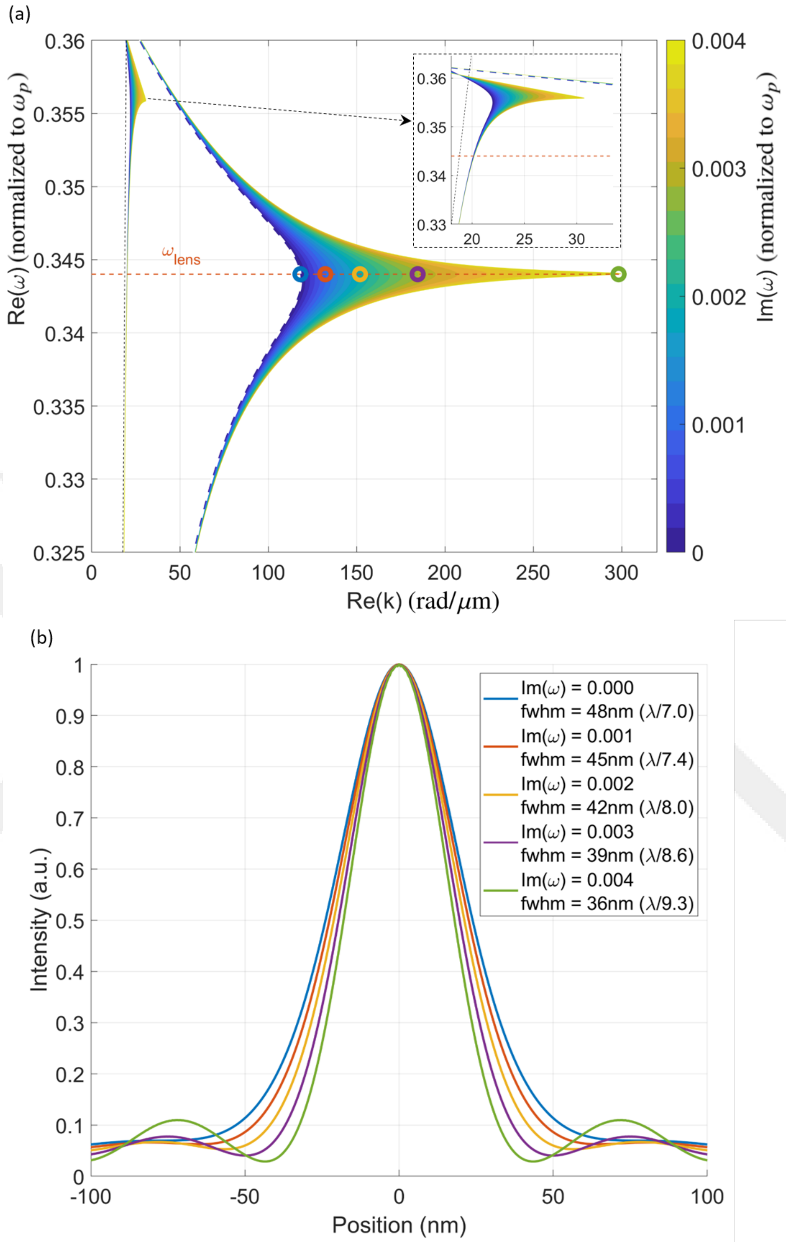


Figure 3.10: **(a)** The dispersion surface for the air-silver-air (IMI) structure, i.e. the superlens. Since the superlens supports two SPP modes, the dispersion surface consists of two distinct regions/surfaces, one for each mode. The higher frequency SPP (see inset) does not contain high spatial frequencies. The lower frequency SPP, however, extends to large $k$ values and its backbending region indeed defines the operating frequency ($\omega_{lens}$) of the superlens where $Re(\epsilon_{silver}) \approx -\epsilon_0$. The colored circles indicate the complex frequencies with different exponential decay rates that are selected for the FDTD simulations. **(b)** Using the FDTD simulations, image intensities are measured for each frequency selected on the dispersion surface (colored circles), with their full-widths at half-maximum (FWHM). It is seen that the faster decay rates provide better resolution. As predicted by the dispersion surface, the SPP modes excited with larger $Im(\omega)$ have larger wave vectors which, in turn, leads to a narrower point spread function.

mittivity of the silver matches the surrounding medium, i.e. $Re(\epsilon_{silver}) \approx -\epsilon_0$. The high frequency mode (see inset), on the other hand, bends back at significantly lower values of $k$ than the operating frequency of the superlens, and therefore, does not play any role in the operation of the superlens.

To demonstrate the improvement in the resolution of the superlens due to the introduction of temporal loss into the system, we have selected five different exponential decay rates in time, as indicated by the circles on the dispersion surface in Figure 3.10a, at the operating frequency of the superlens. Then, their image intensities are obtained from the FDTD simulations on a line parallel to the interface of the superlens, with their full-widths at half maximum (FWHM) calculated and shown in Figure 3.10b. As predicted by the dispersion surface, faster decay rate in time provides significantly better resolution in space because the excited SPP mode attains a larger characteristic wave vector. In this example, we have been able to improve the resolution of the superlens for a point object by 25%, from $48nm$ to $36nm$. In conclusion, we have demonstrated that, with the help of the dispersion surface, we can improve the resolution of the superlens, and can easily apply the approach to similar problems like those studied in [59, 60, 61].

### *3.4.1 Convergence of the FWHM of the superlens image*

As detailed in Section 3.7, the response of the system to the excitation in Figure 3.14 is $\epsilon(j\omega_c)E(t)$ for large $t$, i.e. it is excited with the waveform $e^{j\omega_c t}$. In this section, using FDTD experiments with different complex frequencies, we show how the FWHM of the superlens image converges to its final value as time progresses. In Figure 3.11, it is seen that the FWHM starts with a high value (i.e. the resolution is low). During the onset of the excitation, the FWHM is the same for all experiments because each experiment starts with the same waveform. When the exponential decay is introduced, we observe that each complex frequency converges to their corresponding FWHMs. As predicted by the dispersion surface (Figure 3.10), excitations with higher decay rates produce sharper images (i.e. higher resolution). It is also noticed that it takes longer for higher decay rates to converge to their final

FWHM values, as expected.

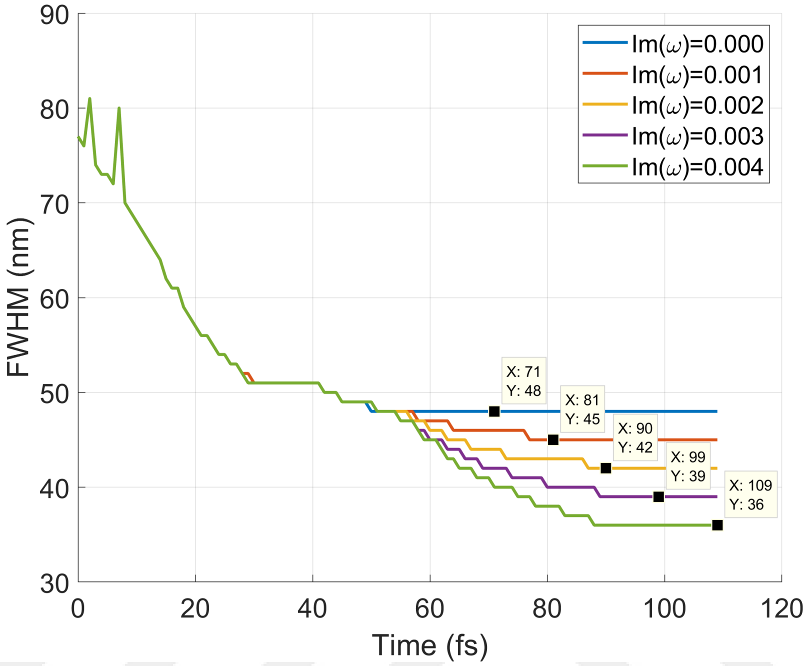


Figure 3.11: Full width at half maximum (FWHM) of the superlens images for experiments with different complex frequencies. The higher temporal decay rates result in better resolution, while it takes longer for the fields to converge to their steady-state value.

### *3.4.2 Mechanism responsible for super resolution in plasmonic structures*

In this section, we briefly touch on the SPP mode that is responsible for super resolution in the super lens structure. We previously discussed that a dielectric-metal-dielectric structure such as the super lens supports two SPP modes: One long-range SPP which has a relatively small $k_x$ with a small imaginary part and one short-range SPP which has a very high $k_x$ with a large imaginary part. In many experimental configurations including the ones discussed in Section 1.5, it is the long-range SPP that is excited and studied. It is close to impossible to excite the short-range SPP in such configurations because it is difficult generate a wave with a large enough momentum ($k_x$) in the tangential direction. This intuition might unintentionally lead one to think that it is the long-range SPP that leads to enhanced resolution in the super lens. Here, we clarify this issue and show that it is in fact the short-range SPP that begets the enhanced resolving power of the super lens.

The spectral response of the super lens studied throughout Section 3.4 is shown in Figure 3.12, where the generalized transmission coefficient is plotted with respect to the tangential component $k_x$ of the wave vector. Each curve corresponds to a different temporal decay rate, in other words, a different complex frequency. There are two peaks in the response of the super lens. The first peak around $k_x = 20$ is the long-range SPP and the second peak around $k_x \approx 150 - 350$ corresponds to the short-range SPP. It was shown in Chapter 2 that the short-range SPP is located at large $k_x$ values with a large imaginary part. This is in line with the observation that the short-range SPP peak is at a higher $k_x$ value but also much broader than the long-range SPP, indicating a high amount loss associated with the mode.

We compare the lateral wave number corresponding to these two peaks (via $2\pi/\lambda = k_x$) with the FWHM values in Figure 3.10b. The long-range SPP peak gives a wave number about $300nm$ which is not sufficient to obtain a FWHM that is as small as $40nm$. On the other hand, the short-range SPP peak corresponds to a wave number of only a few tens of nanometers, which clearly fits the FWHMs observed in our FDTD experiments. Furthermore, the improvement of resolution seen in Figure 3.10b with increasing complex frequency cannot be explained with the long-range SPP because the long-range SPP peak (see inset in Figure 3.12) shows that the resolving power drops beyond $Im(\omega) = 0.002$, which contradicts the FWHMs observed in Figure 3.10b. The growing trend of the transmitted field amplitude at the short-range SPP peak agrees with the observed improvement of FWHMs.

As discussed above, in common experimental configurations, it is difficult to couple to the short-range SPP. The super lens is different in this sense because both the light source (dipole) and the imaging plane are very close to the lens itself. This makes it possible for large spectral components (high $k_x$ values) of the fields generated by the dipole to excite the short-range SPP and consequently contribute to the fields observed on the imaging plane.

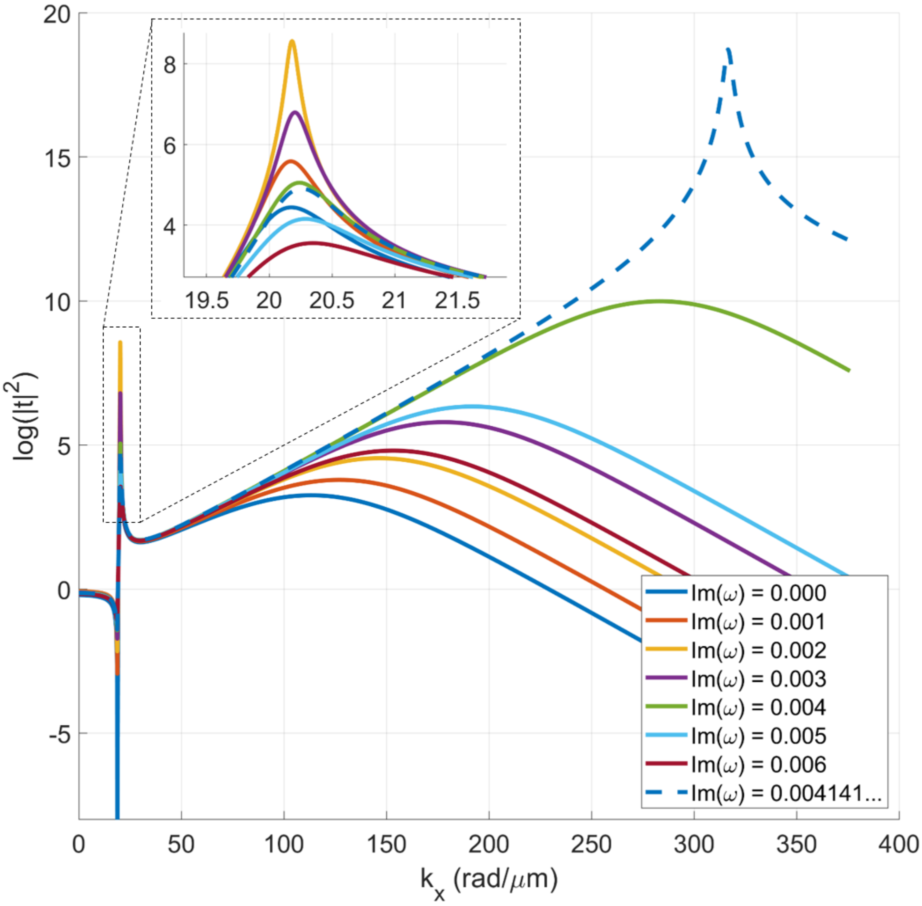


Figure 3.12: The magnitude of the generalized transmission coefficient for the super lens as a function of the wave vector. The first peak around $k_x = 20$ is the long-range SPP and the second peak around $k_x \approx 150 - 350$ corresponds to the short-range SPP, which is a much lossier mode compared to the long-range SPP. The inset shows the region around the long-range SPP peak in detail. Each curve corresponds to a different temporal decay rate.

## 3.5 *Interpretation of the dispersion surface and pseudo-monochromatic SPP modes*

In this chapter, it has been demonstrated theoretically, as well as numerically, that the resolution and the propagation length of SPPs in plasmonic structures can be improved by introducing temporal loss into the system. Although this sentence captures the main highlights of the study, the underlying principle needs to be emphasized for the sake of clarity. The whole idea of introducing temporal loss into plasmonic layered media started from a long lasting confusion of how to decide on the permissible ranges of values of the frequency and the wavenumber in the solution set of the wave equation in such structures. However, in the mathematical study of wave equations with boundary conditions, it has been proven that the solutions in layered open geometries are in the form of $e^{j\omega t - jkx}$ (also referred to as eigen-mode) where the permissible ranges of $\omega$ and $k$ are over the entire complex plane unless the boundary conditions dictate otherwise. Contrary to what mathematics dictates on the choices of $\omega$ and $k$ values, they have been generally assumed that either one has to be real depending on the exact physical situation, excitation and experimental setup. Therefore, the solutions of the wave equation with simultaneous complex wave vectors and complex frequencies have been dismissed and not investigated so far. In this study, we have considered $e^{j\omega t - jkx}$ with complex frequency $\omega$ and complex wave vector $k$ as the fundamental mode of the plasmonic waveguide, and showed that they have properties superior to the SPPs with real frequencies or real wave vectors. In addition, having the fundamental mode represented in exponential form with both $\omega$ and $k$ complex enables us to utilize the conventional frequency-domain tools and results, such as the Fresnel reflection coefficient, the Drude model, and the dispersion equation, by just substituting in complex $\omega$ and $k$. As a result, a simple yet powerful framework for pseudo-monochromatic modes has been established and verified using the FDTD simulations.

Another issue that needs further clarification is the counterintuitive improvements in resolution and propagation length of the SPPs when the source is turned off exponentially in time, in other words, when the temporal loss is introduced into the system. The underlying physics responsible for these phenomena is actually hidden in the equation of motion for free electrons, which is used to derive the Drude model for the relative permittivity of the metal, whose real and imaginary parts are shown in Figure 3.13 for a range of complex frequencies. While the increase in the effective propagation length can be attributed to the decrease in the magnitude of the imaginary part of the permittivity (dashed lines), the resolution benefits from both the decrease in $|Im(\epsilon)|$ and the increase in $|Re(\epsilon)|$ (solid lines). We have found that there is a theoretical upper limit on resolution, which is exactly at the natural resonance frequency of the electrons, i.e., at $Im(\omega) = \gamma/2$, where $Im(\epsilon)$ is zero and $|Re(\epsilon)|$ reaches its maximum. However, there is no such limit for the propagation length, except for many practical limits arising as the temporal decay rate increases.

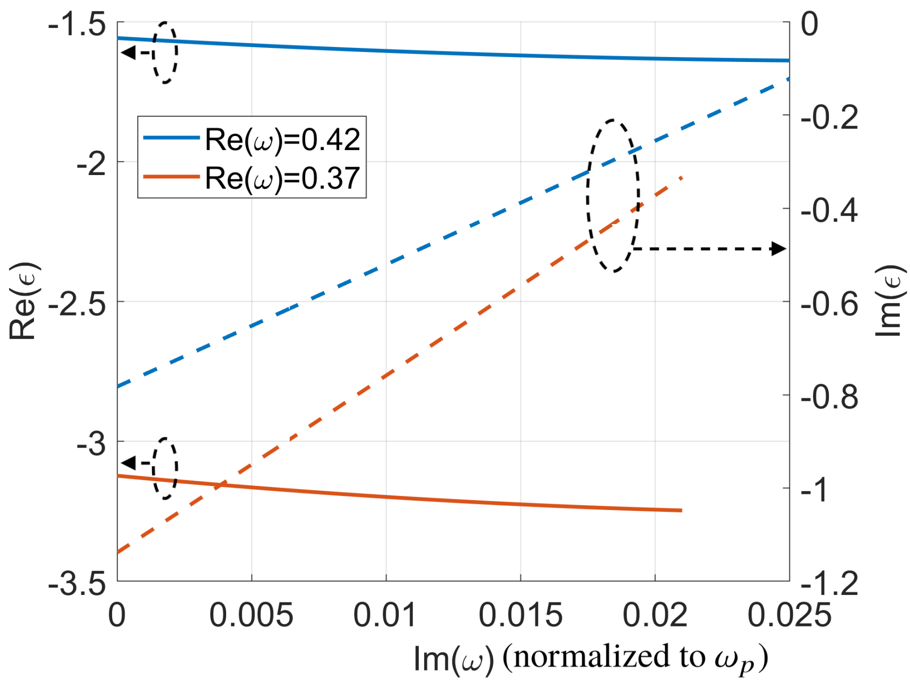


Figure 3.13: Relative permittivity of the metal by the Drude model for a range of complex frequency (3.2), where $\omega_p = 1.04 \times 10^{16}\ rad/s$, $\gamma = 6.15 \times 10^{14}\ rad/s = 0.059 \times \omega_p$, $\epsilon_\infty = 4$ are used. Note that $|Im(\epsilon)|$ decreases and $|Re(\epsilon)|$ increases as temporal decay $Im(\omega)$ is introduced to the excitation source. This is the underlying reason for the improvements observed in the resolution and propagation length.

Considering the results in Figure 3.2 and Figure 3.3, it is possible to prescribe a recipe for manipulating the characteristics of an SPP. If a wide tuning range for the resolution is desired, the frequencies closer to (and below) the back-bending region are more advantageous. This comes at the cost of propagation length since the SPPs at those frequencies experience relatively higher loss compared to lower frequency SPPs. On the other hand, if one desires to maximize the propagation length, one should resort to the lower frequencies away from the back-bending region. This will provide a means to significantly increase the propagation length without going into the extreme $Im(\omega)$ values. There will also be a slight increase in the resolution, although it is minor compared to the higher frequency SPPs.

Another advantage of the pseudo-monochromatic framework presented in this study is the simplicity of the source used to excite the complex SPP modes. Ultrafast pulse shaping techniques are already available for even more complex waveform generation [81, 82]. Therefore, we do not expect a significant problem in realizing practical sources with complex frequencies. Moreover, fluorescent molecules might also provide a natural source of pseudo-monochromatic light excitation since their temporal decays are always exponential in nature. Finally, already existing experimental methods, such as the Kretschmann-Raether, Otto configurations or electron beams, or their modified versions may be employed to selectively control the frequency, wave vector, or the propagation speed of the SPPs [15, 33].

## 3.6 Numerical simulation of plasmonic waveguides and identification of complex SPP modes

The open waveguide (see Figure 3.1) is simulated in a 2D FDTD region with the dimensions of $6um$ along the waveguide direction ($x$), and $4um$ in the vertical direction ($z$). The simulation region is surrounded by perfectly matched layers (PML) on all four sides in order to mimic the open structure with minimal artificial reflections from the PMLs. A uniform square mesh with a side length of $0.5nm$ covers the $50nm$ thick insulating layer (air in this case) and extends $175nm$ into the metal layers on both sides. For the rest of the metal layers, a conformal mesh that gradually becomes less dense away from the interfaces is used to reduce the computation time. With regard to the source and the resulting field distributions, a vertical electric dipole is placed in the insulating layer, while a time-domain line monitor is used in the same layer along the propagation direction to collect the field components as a function of both space and time.

The waveform used to excite the waveguide is shown in Figure 3.14, where the time signature of the dipole source is shown to oscillate with a frequency of $Re(\omega)$ at all times with an amplitude modulation. Initially, the amplitude is slowly increased from zero to a finite value, by modulating it with the sigmoid function $\frac{1}{1+e^{-at}}$. This is to alleviate possible convergence issues that may be encountered in the FDTD simulations when the source is turned on abruptly, resulting in an excitation of a wide spectrum of frequencies that might in turn give rise to unwanted reflections from the PML. Note that this slow buildup is needed only for the FDTD simulations and has no relevance to any real-life applications. Following that, the dipole is let to oscillate for a while at this constant amplitude so that the transient fields generated by the ramp-up attenuate significantly. When the steady-state is reached, an exponential temporal decay $e^{-Im(\omega)t}$ is introduced in order for effectively making the oscillation frequency complex. As a result, a complex SPP mode with improved resolution and propagation length can be excited. To detect this SPP mode, the fields are observed long after the exponential decay is applied (indicated by the red arrow in Figure 3.14), making sure the transient fields due to switching from monochromatic to pseudo-monochromatic region have died off.

The field components of the SPP are collected on a $1\mu m$ long line along the waveguide away from the dipole. In order to extract the frequency and the wave vector of the SPP from the field distribution, we use the generalized pencil-of-function (GPOF) method, which helps represent the field in terms of complex exponentials [78], whose exponents are proportional to $kx - \omega t$. That is, the field distribution monitored along the $1\mu m$ line at a fixed time, which contains approximately 5 periods of the SPP, is decomposed into two complex exponentials, one for the SPP and the other for the numerical noise or any remaining lossy waves. Since the waveguide supports only the SPP mode at such a distance, two exponentials are sufficient to obtain accurate results of $k$. The same approach is also used to retrieve the complex $\omega$ from the same field distribution, but this time at a fixed distance $x$ over a finite time span.

For the sake of demonstration, we ran a few numerical experiments following the outlined procedure for the source with the temporal decay of up to $Im(\omega) = 0.025$,

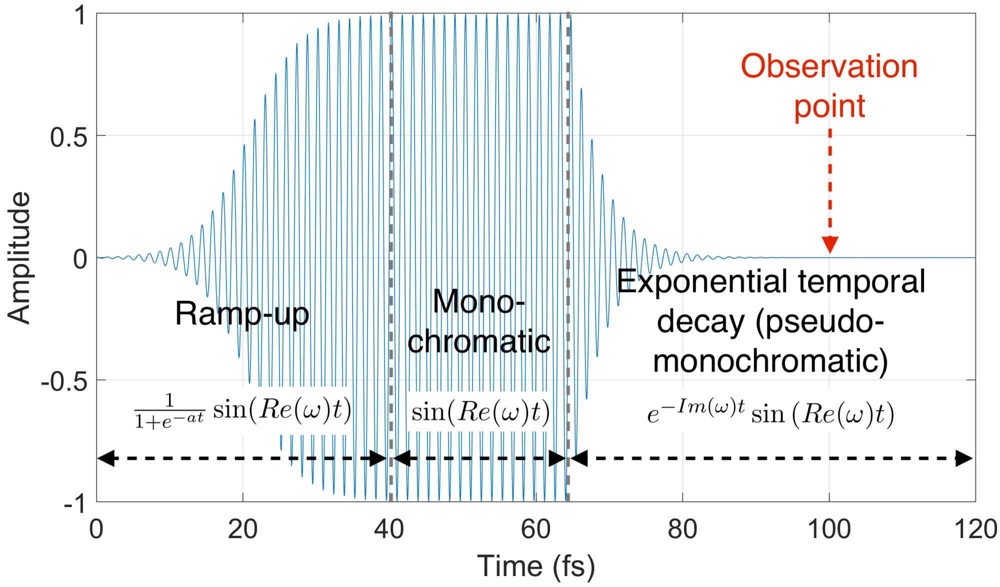


Figure 3.14: The dipole excitation signal used in the FDTD simulations. The oscillation amplitude is slowly increased in order to avoid undesired numerical noise in simulations. Then, the system is driven monochromatically until it reaches the steady-state, making sure the transient fields have decayed. Finally, the exponential temporal decay is applied to the dipole. The resulting complex excitation frequency generates a complex SPP mode with improved resolution and propagation length. The fields are observed long after the start of the pseudo-monochromatic signal, making sure any transient fields due to switching do not affect the measurements.

as normalized to the plasma frequency $\omega_p$, since faster decays require finer and larger FDTD simulations. We believe that the results presented in this study are sufficient to showcase this new venue for dispersion engineering, and to convey the underlying physics. As discussed in previous sections, it is possible to obtain even further improvements than shown in Figure 3.3 & 3.5 by employing faster temporal decay rates.

## 3.7 Validity of using complex frequencies

### 3.7.1 Response of metals to realizable complex frequency signals

In this section, we discuss the validity of using complex frequencies in our study. We aim to address several concerns that might be brought up by the unconventional nature of our approach and its counter-intuitive implications. The response of the plasmonic structures we study is fundamentally governed by the motion of free electrons in the metal, which renders the entire system dispersive. Therefore, we start with the equation of motion for free electrons in the metal and derive the response to an arbitrary input.

$$m\ddot{x}(t) = -eE(t) - m\gamma\dot{x}(t) - m\omega_0^2 x(t) \tag{3.4}$$

Assuming $\omega_0 = 0$ (free electrons) and zero initial conditions, we get the following Laplace transform (we use Laplace transform since we will be using complex frequencies).

$$X(s) = \frac{-e/m}{s^2 + s\gamma} E(s) \tag{3.5}$$

Using polarization density $P = -nex$ and $D(s) = \epsilon_0 E(s) + P(s)$, we can obtain the permittivity (i.e. the response) of the medium.

$$\epsilon(s) = \epsilon_0 + \frac{\epsilon_0 \omega_p^2}{s^2 + \gamma s} \tag{3.6}$$

Next, we excite the system with an input of $E(t) = e^{j\omega_c t}u(t)$, whose Laplace transform is $E(s) = 1/(s - j\omega_c)$, where the frequency $\omega_c$ is complex-valued ($Im(\omega_c) > 0$). Note that this is a realistic signal that switches on at $t = 0$ and exponentially decays with increasing $t$. The switching at $t = 0$ causes frequencies other than $\omega_c$ to be excited; however, we show below that these frequencies are highly damped and can be ignored under certain conditions, which are valid in our study.

$$D(s) = \epsilon(s)E(s) = \frac{\epsilon_0}{s - j\omega_c} + \frac{\epsilon_0 \omega_p^2}{(s^2 + \gamma s)(s - j\omega_c)} \tag{3.7}$$

After calculating the inverse Laplace transform, we get

$$D(t) = \epsilon_0 e^{j\omega_c t} u(t) + \epsilon_0 \omega_p^2 [A + Be^{-\gamma t} + Ce^{j\omega_c t}] u(t) \tag{3.8}$$

where $A = -1/(j\omega_c \gamma)$, $B = 1/(\gamma^2 + j\omega_c \gamma)$ and $C = 1/(-\omega_c^2 + j\omega_c \gamma)$. Recombining the terms,

$$D(t) = \epsilon(j\omega_c) e^{j\omega_c t} u(t) + B\epsilon_0 \omega_p^2 e^{-\gamma t} u(t) + A\epsilon_0 \omega_p^2 u(t) \tag{3.9}$$

The first term on the right hand side is the response of the medium to the monochromatic excitation with the frequency $\omega_c$, as understood from $\epsilon(j\omega_c)$ (permittivity is evaluated at the complex frequency $\omega_c$). The second term with B is the response due to the switching at $t = 0$, which decays with the natural decay rate $\gamma$ of the electrons. The third term with A represents the constant displacement due to the lack of restoring force $\omega_0$, which we can ignore. Notice that for $\gamma > Im(\omega_c)$, the response of the system is governed by $\epsilon(j\omega_c)E(t)$ for large $t$. These conditions (i.e. $\gamma > Im(\omega_c)$ and large $t$) holds true in all of the source and waveguide configurations we investigate. As explained in Section 3.6, the numerical measurements are made long after the switching at $t = 0$, allowing all fields to dissipate except the $\epsilon(j\omega_c)e^{j\omega_c t}u(t)$ term. Therefore, one can conclude that the medium behaves as if it is excited by a single frequency $\omega_c$. This is true for both the theoretical calculations and the numerical simulations with the excitation shown in Figure 3.14. This is further validated by the agreement between the theoretical predictions and the results of the numerical simulations as shown in Figure 3.3.

### *3.7.2 Discussion on the boundary value problem for layered media*

From a mathematical point of view, dispersion relation is nothing but an equation that defines all possible eigenvalues associated with the eigenfunctions in a given operator equation. In most problems related to physics and engineering, the operators are usually cast into the differential-equation form, with appropriate boundary and/or initial conditions defined by the specific problem at hand, whose unique solution can be written as a linear combination of eigenfunctions (modes). For example, for the wave equation in a translationally invariant geometry, such as planar layered structures, the eigenfunctions are easily obtained to be in the form of $e^{j\omega t - jkr}$, for which no restriction is imposed on neither $\omega$ nor $k$ yet. Therefore, at this stage, the eigenvalue pairs, $\omega$ and $k$, are to be assumed complex values in order to account for the possible temporal and spatial losses, respectively, until the initial and/or boundary conditions are imposed to eliminate some eigenvalue sets that can not comply with these conditions. Only then, the remaining $(\omega, k)$ pairs would be the possible eigenvalue pairs, i.e., the dispersion relation, for the specific problem with the given boundary/initial conditions.

To have a better physical underpinning for the dispersion relation associated with the same wave equation stated above, one may need to examine the losses involved in the system and their manifestations in the solution. Therefore, it is necessary to account for the temporal loss and the spatial loss in the wave equation, where the former manifests itself as the imaginary part of complex $\omega$, the latter, on the other hand, sneaks into the dielectric function of the medium (the Drude model) through the Lorentz model for the atomic polarizability and presents itself in the imaginary part of the dielectric function $\epsilon(\omega)$. Since the dielectric function of a metal is also a function of frequency, $k$ has to be a nonlinear function of $\omega$; as such, it is impossible to separate the contributions of the temporal loss and the spatial loss in the solution. Therefore, one can not arbitrarily lump these two losses into $\omega$ or $k$ by letting one to be complex and the other to be real quantity unless the boundary/initial conditions force them to. For example, if the excitation is a uniform plane wave with decaying sinusoidal time variation, like $e^{j\omega t}$ where $\omega = \omega' + j\omega''$ $(e^{-\omega'' t}cos(\omega' t))$, in a Kretschmann configuration, it is inevitable to keep $\omega$ complex while the values of $k$ are set by the medium and the boundary conditions.

To summarize, one cannot arbitrarily decide the nature of $k$ and $\omega$, they should be dictated by the boundary and/or initial conditions of the specific problem at hand. Although this conclusion is rather obvious from mathematical point of view, for the sake of completeness, it will be demonstrated in a simple setting of a one-dimensional cavity, for which the governing equation can be written as

$$[\partial_x \partial_x - \gamma \partial_t - \partial_t \partial_t]\, u(x,t) = 0 \tag{3.10}$$

Assuming that the boundary/initial conditions to be used would allow the use of the method of separation of variables ($u(x,t) = u_x(x)u_t(t)$), the solutions of the differential equation can be composed of

$$u_x = Ae^{jkx} + Be^{-jkx}\ , \qquad u_t = Ce^{j\omega_1 t} + De^{j\omega_2 t} \tag{3.11}$$

where $A, B, C, D$ are unknown coefficients, and $\omega_1$, $\omega_2$ and $k$ are related through the dispersion relation as

$$\omega_{1,2} = \pm\sqrt{k^2 - \frac{\gamma^2}{4}} + j\frac{\gamma}{2} \tag{3.12}$$

Note that only the dissipation coefficient $\gamma$ is assumed to be real and positive so far, but there is no restriction on the selection of the other parameters, $\omega_{1,2}$ and $k$, yet. However, with the introduction of the boundary/initial conditions stated below, it will be demonstrated that the solution set and the associated eigenvalue pairs will be further restricted.

- Assume a one-dimensional cavity between $x = 0$ and $x = 1$ with the boundary conditions of $u(0,t) = u(1,t) = 0$ and $e^{j\omega t}$ time dependence. Imposing these conditions on $u_x$ in (3.11) results in $u_x = j2Asin(n\pi x)$ where $k = n\pi$, and in turn, the dispersion relation turns out to be

$$\omega = \sqrt{n^2\pi^2 - \frac{\gamma^2}{4}} + j\frac{\gamma}{2} \tag{3.13}$$

  where $\omega$ has to be a complex quantity in order to account for the dissipation loss in the medium. This is like the motion of an oscillating string fixed at both ends, where the amplitude of oscillation decays in time due to the friction and air resistance in space. In other words, the dissipation loss in medium manifests itself as a temporal loss in $\omega$.

- Assume a one-dimensional, semi-infinite ($x \in [0, \infty)$) geometry, which is a better representation of the problem at hand, with the following boundary conditions:

$$u(0, t) = f(t) \tag{3.14}$$

$$\lim_{x \to \infty} u(x, t) = 0 \tag{3.15}$$

  where the excitation $f(t)$ is assumed to be a decaying sinusoid, i.e., $e^{j\omega_c t}$ with complex $\omega_c = \omega'_c + j\omega''_c$, and is applied at $x = 0$. Note that, although this problem may not seem suitable for the separation of variables with the given boundary conditions, the solution turns out to be separable ($u(x, t) = e^{-jkx}e^{j\omega_c t}$) because of the complex harmonic nature of the source at $x = 0$. Consequently, both $\omega$ and $k$ have to be complex in order to account for the temporal decay in the source and the spatial attenuation due to the loss in the medium, respectively:

$$\omega = \omega_c = \omega'_c + j\omega''_c \tag{3.16}$$

$$k = \sqrt{\omega_c^2 - j\gamma\omega_c} \tag{3.17}$$

It is important to notice that the imaginary parts in frequency and wave number represent decay with respect to time and space, respectively. Looking at a single solution of the wave equation in the form of $e^{j\omega t - jkx}$, one may be inclined to think that the imaginary part of one may be lumped into the imaginary part of the other. However, the relationship between the frequency and the wave number is not trivial (see Eq. (3.12)), hence arbitrary exchange of imaginary parts would violate the dispersion relation.

### *3.7.3 Fourier expansion of a complex frequency in terms of real frequencies*

Although it has been shown that the modes with both complex frequency and complex wave number are supported by the medium defined above, one may still question the validity of the modes with complex frequency on the basis that $e^{j\omega_c t}$ can be written in terms of infinitely many modes with real frequencies using the Fourier transform as

$$e^{j\omega_c t}u(t) = \int_{-\infty}^{\infty} F(\omega)e^{j\omega t}d\omega \tag{3.18}$$

where $F(\omega) = 1/j(\omega - \omega_c)$. For large enough $t$, the Fourier expansion on the right-hand side of (3.18) will converge to the solution with the complex frequency $\omega_c$. However, one needs to include frequencies from $-\infty$ to $\infty$ for the Fourier transform to be accurate. This is implemented numerically for $\omega_c = 1+j0.1$ (see Supplementary Movie C.3). In Fig. 3.15, the convergence with respect to the limits of integration is plotted (a cutoff frequency is applied to the limits of integration, and convergence is observed as the cutoff frequency is increased).

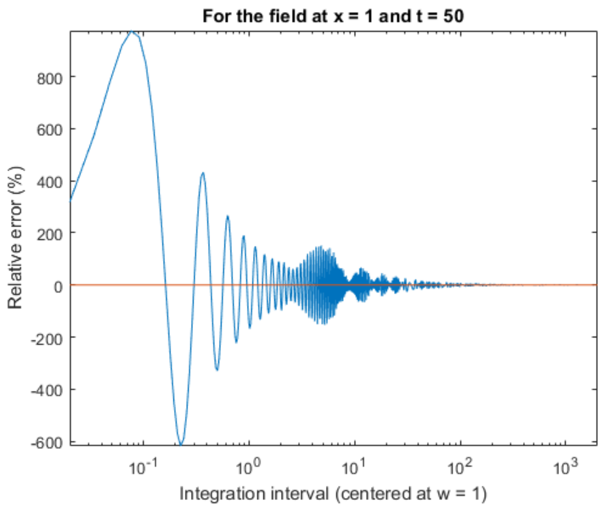


Figure 3.15: Convergence of Fourier transform solution to the exact solution with complex frequency for 1D problem.

The analysis above is also applied to the SPPs in the KRC studied in this chapter, where a temporally decaying wave with a normalized frequency of $\omega_c = 0.5+j0.02$ is employed as the incident wave at the glass-metal interface. Once the magnetic field at $x = z = 0$ is calculated directly using the reflection coefficient corresponding to $\omega_c$, it is compared to the result obtained by using the real frequencies in the Fourier transform,

$$e^{j\omega_c t}u(t) = \int_{-\infty}^{\infty} \frac{1}{j(\omega - \omega_c)}[1 + r(\omega)]e^{j\omega t}d\omega \tag{3.19}$$

where $r$ is the generalized reflection coefficient as defined in equation (3.1). The comparison is made over a time interval for a range of integral limits (see Supplementary Movie C.4). Similarly, in Fig. 3.16, it is shown at a single position and time how the Fourier transform solution converges to the exact solution using the complex frequency $\omega_c$.

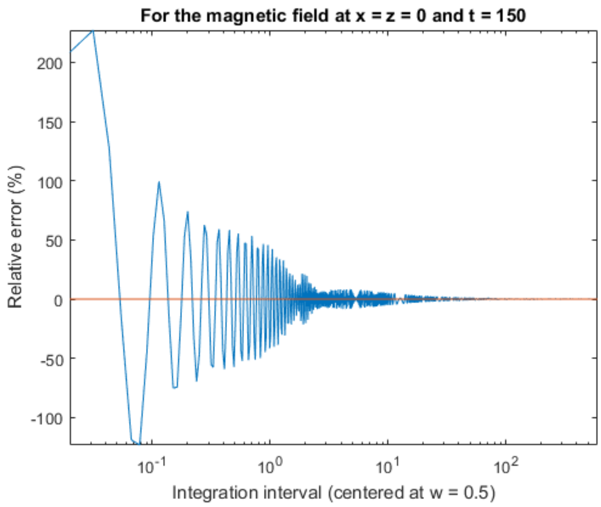


Figure 3.16: Convergence of Fourier transform solution to the exact solution with complex frequency for SPP's magnetic field in the KRC.

This analysis proves that the approach used in this chapter with complex frequencies is valid, and the solutions with both complex frequencies and complex wave numbers are indeed eigenmodes supported by the structure at hand. A set of real frequencies used by the Fourier transform method provides only an approximation that converges to the exact solution in the limit.

## *3.8 Conclusion*

In this chapter, the dispersion equation for surface plasmons in layered media was investigated and shown to be surface rather than a curve. On this dispersion surface, there exists previously unidentified SPP modes whose characteristic frequencies and wave vectors are simultaneously complex valued. These complex SPP modes were studied in the pseudo-monochromatic framework where the standard frequency domain approach is extended to time-varying signals with decaying or growing amplitudes using a single complex frequency. This allowed the use of simple frequency domain expressions to theoretically calculate SPP features such as resolution and propagation length. The results of the dispersion surface was demonstrated on two iconic examples in the field of plasmonics: The metal-insultor-metal plasmonic waveguide and the silver superlens. It was shown that the propagation length in the MIM waveguide is significantly higher than what is possible by using the conventional SPP modes with real frequencies. Moreover, for the silver superlens structure, it was shown that the resolution can be enhanced by using complex frequencies to make use of complex SPP modes. The theoretical predictions were validated using FDTD simulations. Finally, the underlying physical mechanism for the dispersion surface was discussed. The main findings in this chapter have been published in the scientific literature [83].

Chapter 4

# CONCLUDING REMARKS AND FUTURE WORK

The aim of this thesis has been to critically scrutinize the theoretical foundations on which the field of plasmonics based. By reviewing the fundamentals of plasmonics, we set the stage for more detailed discussions around what a surface plasmon is, what its field and energy profiles look like, and how they are excited in experimental configurations. It was shown that a complete theoretical treatment of surface plasmons had been lacking in the literature. The treatment in this thesis revealed missing pieces and settled the confusion around the experimental observations and theoretical calculations. Furthermore, the SPP dispersion was proven to be much richer than what is presented in current studies. This rich dispersion was shown to consist of complex SPP modes that provide better features than common SPP modes and can be excited by utilizing the time dimension of the excitation signal.

The first chapter laid the basics of plasmonics which are referred to in subsequent chapters. The definition of a surface wave, which is confined to an interface between two dissimilar media, was provided. This was later extended to multi-layered media in Chapter 2. The Drude model for metals was derived and the physical picture behind the model was discussed. This model is revisited in Chapter 3. Finally, the experimental configurations that can be used to excite SPPs were presented. For each configuration, the physical mechanism that facilitates the SPP excitation was discussed. The relationship between experimental configurations and theoretical results were detailed in Chapter 2.

In Chapter 2, a comprehensive analysis for SPPs was provided. The detailed descriptions for field and energy profiles were discussed for all extrema of the transfer function of plasmonic structures. It was shown that the conventional picture of an SPP as a single pole in the proper Riemann sheet of the generalized reflection or transmission coefficient is incomplete. The SPP-related phenomena such as field enhancement, confinement and extinction can only be explained by taking into account all poles and zeros in both the proper and the improper Riemann sheets. The so-called unphysical modes on the improper sheet have been shown to play a vital role in the behaviour of plasmonic modes. This complete picture also resolved the confusion around the dip of the reflectance spectrum and the peak of the transmission spectrum in experimental contexts. The investigation of these poles and zeros and the identification of experimental excitations on the Riemann sheets yielded a clear quantitative mapping between theoretical and experimental observations. Empowered by this analysis, the dependence of SPP features on design parameters such as dielectric constant and metal film thickness were re-investigated. Several optimization schemes were provided depending on the experimental applications and the desired output.

In Chapter 3, a generalized solution to the SPP dispersion equation was presented. SPP modes with simultaneous complex frequency and complex wave vector were identified. As a result, the dispersion equation was cast as a surface consisting of a rich solution set of complex SPPs, rather than just a curve. These complex SPP modes were investigated in the pseudo-monochromatic framework and shown to have superior features compared to the conventional modes with real frequencies or real wave vectors. Specifically, it was shown that these complex SPP modes provided better resolution is IMI superlens structures and longer propagation length in MIM plasmonic waveguides. The theoretical calculations were validated with full-wave FDTD simulations. The underlying physical mechanism responsible for the existence of complex SPP modes were discussed by re-investigating the response of a metal in the Laplace domain. Furthermore, the relationship between experimental observations and the dispersion surface was discussed. It was shown that by tailoring the time signature of the excitation source, it is possible to excite complex SPP modes.

The theoretical investigation conducted in this thesis should be applicable to plasmonic structures other than layered media. Another popular and commonly used plasmonic structure is the metallic nanosphere. The field enhancement caused by localized surface plasmons, which is the result of the interaction between electromagnetic fields and metallic nanoparticles, is also expected to benefit from excitations with complex frequencies. Tapered IMI or MIM waveguides to trap and study light are other examples where this approach can be utilized. Another example is the layered plasmonic structure used for the detection of molecules binding to the surface of the structure or the excitation of molecules to study higher order (nonlinear) electromagnetic response. This type of experiments should readily benefit from a properly designed source exciting complex SPPs.

Hopefully the findings in this thesis will eventually lead to experimental realizations of better plasmonic devices for a multitude of applications. An immediate and practical extension of the work presented in this thesis should be the design of a source that is easy to implement experimentally and can be used to excite plasmonic structures such as an MIM waveguide or an IMI superlens.

It should be noted that the analysis conducted throughout this thesis is applicable to other fields studying wave phenomena and dispersion. Within the field of electromagnetics, an immediate list of candidates that comes to mind contains photonics crystals, metamaterials, graphene-based devices, transformation optics, among others. All of these subjects heavily involve dispersive materials which can possibly be exploited further by using complex frequency excitations. Acoustics is also another field of study where a discrepancy between real frequency and real wave vector solutions have already been observed. The complex frequency - complex wave vector approach should unify these seemingly incompatible solutions, as it did for surface plasmons. A similar approach can also be attempted for the study of spatial dispersion although this has not been elaborated on in this work. Based on the analogy between frequency and wave vector, interesting phenomena may emerge when excitations with complex wave vectors are employed in spatially dispersive materials.

# BIBLIOGRAPHY

[1] H. A. Atwater and A. Polman, "Plasmonics for improved photovoltaic devices," *Nature materials*, vol. 9, no. 3, pp. 205–213, 2010.

[2] S. Pillai, , and M. Green, "Plasmonics for photovoltaic applications," *Solar Energy Materials and Solar Cells*, vol. 94, no. 9, pp. 1481–1486, 2010.

[3] M. Loyez, J.-C. Larrieu, S. Chevineau, M. Remmelink, D. Leduc, B. Bondue, P. Lambert, J. Devière, R. Wattiez, and C. Caucheteur, "In situ cancer diagnosis through online plasmonics," *Biosensors and Bioelectronics*, vol. 131, pp. 104–112, 2019.

[4] S. D. Russell and J. N. Ptasinski, "Plasmonic transistor," Feb. 7 2012. US Patent 8,111,443.

[5] J. Tominaga, C. Mihalcea, D. Büchel, H. Fukuda, T. Nakano, N. Atoda, H. Fuji, and T. Kikukawa, "Local plasmon photonic transistor," *Applied Physics Letters*, vol. 78, no. 17, pp. 2417–2419, 2001.

[6] J. Lin, H. Li, H. Zhang, and W. Chen, "Plasmonic enhancement of photocurrent in mos2 field-effect-transistor," *Applied Physics Letters*, vol. 102, no. 20, p. 203109, 2013.

[7] A. Purkayastha, T. Srivastava, and R. Jha, "Ultrasensitive thz–plasmonics gaseous sensor using doped graphene," *Sensors and Actuators B: Chemical*, vol. 227, pp. 291–295, 2016.

[8] A. Farmani and A. Mir, "Graphene sensor based on surface plasmon resonance for optical scanning," *IEEE Photonics Technology Letters*, vol. 31, no. 8, pp. 643–646, 2019.

[9] A. G. Brolo, “Plasmonics for future biosensors,” *Nature Photonics*, vol. 6, no. 11, pp. 709–713, 2012.

[10] M. I. Stockman, K. Kneipp, S. I. Bozhevolnyi, S. Saha, A. Dutta, J. Ndukaife, N. Kinsey, H. Reddy, U. Guler, V. M. Shalaev, *et al.*, “Roadmap on plasmonics,” *Journal of Optics*, vol. 20, no. 4, p. 043001, 2018.

[11] A. M. Urbas, Z. Jacob, L. Dal Negro, N. Engheta, A. Boardman, P. Egan, A. B. Khanikaev, V. Menon, M. Ferrera, N. Kinsey, *et al.*, “Roadmap on optical metamaterials,” *Journal of Optics*, vol. 18, no. 9, p. 093005, 2016.

[12] N. C. Lindquist, P. Nagpal, K. M. McPeak, D. J. Norris, and S.-H. Oh, “Engineering metallic nanostructures for plasmonics and nanophotonics,” *Reports on Progress in Physics*, vol. 75, no. 3, p. 036501, 2012.

[13] M. L. Brongersma and V. M. Shalaev, “The case for plasmonics,” *science*, vol. 328, no. 5977, pp. 440–441, 2010.

[14] E. Le Ru and P. Etchegoin, *Principles of Surface-Enhanced Raman Spectroscopy: and related plasmonic effects.* Elsevier, 2008.

[15] S. A. Maier, *Plasmonics: fundamentals and applications.* Springer Science & Business Media, 2007.

[16] M. Born and E. Wolf, *Principles of optics: electromagnetic theory of propagation, interference and diffraction of light.* Cambridge university press, 1999.

[17] D. J. Griffiths, *Introduction to Electrodynamics.* Printice-Hall International, Inc., 1999.

[18] J. D. Jackson, “Classical electrodynamics,” 1999.

[19] S. Raza, T. Christensen, M. Wubs, S. I. Bozhevolnyi, and N. A. Mortensen, "Nonlocal response in thin-film waveguides: loss versus nonlocality and breaking of complementarity," *Physical Review B*, vol. 88, no. 11, p. 115401, 2013.

[20] S. Raza, S. I. Bozhevolnyi, M. Wubs, and N. A. Mortensen, "Nonlocal optical response in metallic nanostructures," *Journal of Physics: Condensed Matter*, vol. 27, no. 18, p. 183204, 2015.

[21] S. Babar and J. Weaver, "Optical constants of cu, ag, and au revisited," *Applied Optics*, vol. 54, no. 3, pp. 477–481, 2015.

[22] K. M. McPeak, S. V. Jayanti, S. J. Kress, S. Meyer, S. Iotti, A. Rossinelli, and D. J. Norris, "Plasmonic films can easily be better: rules and recipes," *ACS photonics*, vol. 2, no. 3, pp. 326–333, 2015.

[23] E. Kretschmann and H. Raether, "Notizen: Radiative decay of non radiative surface plasmons excited by light," *Zeitschrift für Naturforschung A*, vol. 23, no. 12, pp. 2135–2136, 1968.

[24] A. Otto, "Excitation of nonradiative surface plasma waves in silver by the method of frustrated total reflection," *Zeitschrift für Physik*, vol. 216, no. 4, pp. 398–410, 1968.

[25] F. López-Tejeira, S. G. Rodrigo, L. Martín-Moreno, F. J. García-Vidal, E. Devaux, T. W. Ebbesen, J. R. Krenn, I. Radko, S. I. Bozhevolnyi, M. U. González, *et al.*, "Efficient unidirectional nanoslit couplers for surface plasmons," *Nature Physics*, vol. 3, no. 5, pp. 324–328, 2007.

[26] E. G. Loewen and E. Popov, *Diffraction gratings and applications.* CRC Press, 2018.

[27] J. Homola, I. Koudela, and S. S. Yee, "Surface plasmon resonance sensors based on diffraction gratings and prism couplers: sensitivity comparison," *Sensors and Actuators B: Chemical*, vol. 54, no. 1-2, pp. 16–24, 1999.

[28] S. S. Akarca-Biyikli, I. Bulu, and E. Ozbay, "Resonant excitation of surface plasmons in one-dimensional metallic grating structures at microwave frequencies," *Journal of Optics A: Pure and Applied Optics*, vol. 7, no. 2, p. S159, 2005.

[29] P. Lalanne, J. Hugonin, and J. Rodier, "Theory of surface plasmon generation at nanoslit apertures," *Physical review letters*, vol. 95, no. 26, p. 263902, 2005.

[30] D. Bohm and D. Pines, "A collective description of electron interactions. i. magnetic interactions," *Physical Review*, vol. 82, no. 5, p. 625, 1951.

[31] H. Watanabe, "Experimental evidence for the collective nature of the characteristic energy loss of electrons in solids–studies on the dispersion relation of plasma frequency–," *Journal of the Physical Society of Japan*, vol. 11, no. 2, pp. 112–119, 1956.

[32] R. Ritchie, "Plasma losses by fast electrons in thin films," *Physical Review*, vol. 106, no. 5, p. 874, 1957.

[33] S. Gong, M. Hu, R. Zhong, X. Chen, P. Zhang, T. Zhao, and S. Liu, "Electron beam excitation of surface plasmon polaritons," *Optics express*, vol. 22, no. 16, pp. 19252–19261, 2014.

[34] S. Gong, M. Hu, R. Zhong, T. Zhao, C. Zhang, and S. Liu, "Mediated coupling of surface plasmon polaritons by a moving electron beam," *Optics express*, vol. 25, no. 21, pp. 25919–25928, 2017.

[35] Z. Song, X. Li, J. Hao, S. Xiao, M. Qiu, Q. He, S. Ma, and L. Zhou, "Tailor the surface-wave properties of a plasmonic metal by a metamaterial capping," *Optics Express*, vol. 21, no. 15, pp. 18178–18187, 2013.

[36] W. Sun, Q. He, S. Sun, and L. Zhou, "High-efficiency surface plasmon meta-couplers: concept and microwave-regime realizations," *Light: Science & Applications*, vol. 5, no. 1, p. e16003, 2016.

[37] F. Ding and S. I. Bozhevolnyi, "A review of unidirectional surface plasmon polariton metacouplers," *IEEE Journal of Selected Topics in Quantum Electronics*, vol. 25, no. 3, pp. 1–11, 2019.

[38] T. Wakamatsu and K. Saito, "Interpretation of attenuated-total-reflection dips observed in surface plasmon resonance," *JOSA B*, vol. 24, no. 9, pp. 2307–2313, 2007.

[39] D. Brissinger, L. Salomon, and F. De Fornel, "Unguided plasmon-mode resonance in optically excited thin film: exact modal description of kretschmann–raether experiment," *JOSA B*, vol. 30, no. 2, pp. 333–337, 2013.

[40] J. J. Foley IV, H. Harutyunyan, D. Rosenmann, R. Divan, G. P. Wiederrecht, and S. K. Gray, "When are surface plasmon polaritons excited in the kretschmann-raether configuration?," *Scientific reports*, vol. 5, 2015.

[41] P. Ferguson, R. Wallis, M. Belakhovsky, J. Jadot, and J. Tomkinson, "Surface plasma waves in silver and gold," *Surface Science*, vol. 76, no. 2, pp. 483–498, 1978.

[42] R. D. Olney and R. J. Romagnoli, "Optical effects of surface plasma waves with damping in metallic thin films," *Applied optics*, vol. 26, no. 11, pp. 2279–2282, 1987.

[43] W. C. Chew, *Waves and fields in inhomogeneous media*, vol. 522. IEEE press New York, 1995.

[44] N. Kinayman and M. Aksun, *Modern microwave circuits*. Artech House, 2005.

[45] A. Sennaroglu, *Photonics and laser engineering: principles, devices, and applications*. McGraw-Hill, 2010.

[46] T. Tamir and A. A. Oliner, "Guided complex waves. part 1: Fields at an interface," in *Proceedings of the Institution of Electrical Engineers*, vol. 110, pp. 310–324, IET, 1963.

[47] T. Tamir and A. Oliner, "Guided complex waves. part 2: Relation to radiation patterns," in *Proceedings of the Institution of Electrical Engineers*, vol. 110, pp. 325–334, IET, 1963.

[48] J. Dionne, L. Sweatlock, H. Atwater, and A. Polman, "Planar metal plasmon waveguides: frequency-dependent dispersion, propagation, localization, and loss beyond the free electron model," *Physical Review B*, vol. 72, no. 7, p. 075405, 2005.

[49] A. Chandran, E. S. Barnard, J. S. White, and M. L. Brongersma, "Metal-dielectric-metal surface plasmon-polariton resonators," *Physical Review B*, vol. 85, no. 8, p. 085416, 2012.

[50] J. Dionne, L. Sweatlock, H. Atwater, and A. Polman, "Plasmon slot waveguides: Towards chip-scale propagation with subwavelength-scale localization," *Physical Review B*, vol. 73, no. 3, p. 035407, 2006.

[51] P. Berini, "Long-range surface plasmon polaritons," *Advances in Optics and Photonics*, vol. 1, no. 3, pp. 484–588, 2009.

[52] A. Vinogradov, A. Dorofeenko, A. Pukhov, and A. Lisyansky, "Exciting surface plasmon polaritons in the kretschmann configuration by a light beam," *Physical Review B*, vol. 97, no. 23, p. 235407, 2018.

[53] W. L. Barnes, A. Dereux, and T. W. Ebbesen, "Surface plasmon subwavelength optics," *Nature*, vol. 424, no. 6950, pp. 824–830, 2003.

[54] T. W. Ebbesen, C. Genet, and S. I. Bozhevolnyi, "Surface-plasmon circuitry," *Physics Today*, vol. 61, no. 5, p. 44, 2008.

[55] J. A. Schuller, E. S. Barnard, W. Cai, Y. C. Jun, J. S. White, and M. L. Brongersma, "Plasmonics for extreme light concentration and manipulation," *Nature materials*, vol. 9, no. 3, pp. 193–204, 2010.

[56] G. V. Naik, V. M. Shalaev, and A. Boltasseva, "Alternative plasmonic materials: beyond gold and silver," *Advanced Materials*, vol. 25, no. 24, pp. 3264–3294, 2013.

[57] P. R. West, S. Ishii, G. V. Naik, N. K. Emani, V. M. Shalaev, and A. Boltasseva, "Searching for better plasmonic materials," *Laser & Photonics Reviews*, vol. 4, no. 6, pp. 795–808, 2010.

[58] A. Boltasseva and H. A. Atwater, "Low-loss plasmonic metamaterials," *Science*, vol. 331, no. 6015, pp. 290–291, 2011.

[59] A. Rogov and E. Narimanov, "Space–time metamaterials," *ACS Photonics*, vol. 5, no. 7, pp. 2868–2877, 2018.

[60] M. Dubois, E. Bossy, S. Enoch, S. Guenneau, G. Lerosey, and P. Sebbah, "Time-driven superoscillations with negative refraction," *Physical review letters*, vol. 114, no. 1, p. 013902, 2015.

[61] A. Archambault, M. Besbes, and J.-J. Greffet, "Superlens in the time domain," *Physical review letters*, vol. 109, no. 9, p. 097405, 2012.

[62] P. B. Johnson and R.-W. Christy, "Optical constants of the noble metals," *Physical review B*, vol. 6, no. 12, p. 4370, 1972.

[63] E. Arakawa, M. Williams, R. Hamm, and R. Ritchie, "Effect of damping on surface plasmon dispersion," *Physical Review Letters*, vol. 31, no. 18, p. 1127, 1973.

[64] R. Alexander, G. Kovener, and R. Bell, "Dispersion curves for surface electromagnetic waves with damping," *Physical Review Letters*, vol. 32, no. 4, p. 154, 1974.

[65] G. Kovener, R. Alexander Jr, and R. Bell, "Surface electromagnetic waves with damping. i. isotropic media," *Physical Review B*, vol. 14, no. 4, p. 1458, 1976.

[66] A. F. Koenderink and A. Polman, "Complex response and polariton-like dispersion splitting in periodic metal nanoparticle chains," *Physical Review B*, vol. 74, no. 3, p. 033402, 2006.

[67] M. Conforti and M. Guasoni, "Dispersive properties of linear chains of lossy metal nanoparticles," *JOSA B*, vol. 27, no. 8, pp. 1576–1582, 2010.

[68] I. B. Udagedara, I. D. Rukhlenko, and M. Premaratne, "Complex-$\omega$ approach versus complex-k approach in description of gain-assisted surface plasmon-polariton propagation along linear chains of metallic nanospheres," *Physical Review B*, vol. 83, no. 11, p. 115451, 2011.

[69] L. Wan, Y.-M. Huang, C.-K. Dong, and H.-J. Luo, "Analytical solutions to zeroth-order dispersion relations of a cylindrical metallic nanowire near the backbending point," *The European Physical Journal B*, vol. 85, no. 1, pp. 1–6, 2012.

[70] A. Archambault, T. V. Teperik, F. Marquier, and J.-J. Greffet, "Surface plasmon fourier optics," *Physical Review B*, vol. 79, no. 19, p. 195414, 2009.

[71] M. Weber and D. Mills, "Determination of surface-polariton minigaps on grating structures: A comparison between constant-frequency and constant-angle scans," *Physical Review B*, vol. 34, no. 4, p. 2893, 1986.

[72] W. Barnes, T. Preist, S. Kitson, and J. Sambles, "Physical origin of photonic energy gaps in the propagation of surface plasmons on gratings," *Physical Review B*, vol. 54, no. 9, p. 6227, 1996.

[73] K. C. Huang, E. Lidorikis, X. Jiang, J. D. Joannopoulos, K. A. Nelson, P. Bienstman, and S. Fan, "Nature of lossy bloch states in polaritonic photonic crystals," *Physical Review B*, vol. 69, no. 19, p. 195111, 2004.

[74] J. AS Barker and R. Loudon, "Response functions in the theory of raman scattering by vibrational and polariton modes in dielectric crystals," *Reviews of Modern Physics*, vol. 44, no. 1, p. 18, 1972.

[75] N. Fang, D. Xi, J. Xu, M. Ambati, W. Srituravanich, C. Sun, and X. Zhang, "Ultrasonic metamaterials with negative modulus," *Nature materials*, vol. 5, no. 6, pp. 452–456, 2006.

[76] D. G. Baranov, A. Krasnok, and A. Alù, "Coherent virtual absorption based on complex zero excitation for ideal light capturing," *Optica*, vol. 4, no. 12, pp. 1457–1461, 2017.

[77] Lumerical Inc., "Lumerical fdtd solutions."

[78] Y. Hua and T. Sarkar, "Generalized pencil-of-function method for extracting poles of an em system from its transient response," *IEEE Transactions on Antennas and Propagation*, vol. 37, no. 2, pp. 229–234, 1989.

[79] J. Pitarke, V. Silkin, E. Chulkov, and P. Echenique, "Theory of surface plasmons and surface-plasmon polaritons," *Reports on progress in physics*, vol. 70, no. 1, p. 1, 2006.

[80] J. B. Pendry, "Negative refraction makes a perfect lens," *Physical review letters*, vol. 85, no. 18, p. 3966, 2000.

[81] F. Ferdous, H. Miao, D. E. Leaird, K. Srinivasan, J. Wang, L. Chen, L. T. Varghese, and A. M. Weiner, "Spectral line-by-line pulse shaping of on-chip microresonator frequency combs," *Nature Photonics*, vol. 5, no. 12, p. 770, 2011.

[82] A. M. Weiner, "Ultrafast optical pulse shaping: A tutorial review," *Optics Communications*, vol. 284, no. 15, pp. 3669–3692, 2011.

[83] H. S. Tetikol and M. I. Aksun, "Enhancement of resolution and propagation length by sources with temporal decay in plasmonic devices," *Plasmonics*, pp. 1–10, 2020.

# Appendix A

## CHOICES OF BRANCH IN THE GENERALIZED REFLECTION AND TRANSMISSION COEFFICIENTS

For the branch cut in $k_{z1}$,

$$\tilde{r} = \begin{cases} \frac{r_{12}^p + r_{23}e^{-jk_{z2}2d}}{1+r_{12}^p r_{23}e^{-jk_{z2}2d}} = \tilde{r}^p, \quad \text{proper (Riemann sheet)} \\ \\ \frac{1/r_{12}^p + r_{23}e^{-jk_{z2}2d}}{1+(r_{23}/r_{12}^p)e^{-jk_{z2}2d}} = \frac{1+r_{12}^p r_{23}e^{-jk_{z2}2d}}{r_{12}^p + r_{23}e^{-jk_{z2}2d}} = \frac{1}{\tilde{r}^p}, \quad \text{improper (Riemann sheet)} \end{cases} \tag{A.1}$$

$$\tilde{t} = \begin{cases} \frac{(1+r_{12}^p + r_{23} + r_{12}^p r_{23})e^{-jk_{z2}d}}{1+r_{12}^p r_{23}e^{-jk_{z2}2d}} = \tilde{t}^p, \quad \text{proper} \\ \\ \frac{(1+1/r_{12}^p + r_{23} + r_{23}/r_{12}^p)e^{-jk_{z2}d}}{1+(r_{23}/r_{12}^p)e^{-jk_{z2}2d}} = \frac{(1+r_{12}^p + r_{23} + r_{12}^p r_{23})e^{-jk_{z2}d}}{r_{12}^p + r_{23}e^{-jk_{z2}2d}} = \frac{\tilde{t}^p}{\tilde{r}^p}, \quad \text{improper} \end{cases} \tag{A.2}$$

For the branch cut in $k_{z2}$,

$$r_{23} = \begin{cases} \frac{\epsilon_3 k_{z2} - \epsilon_2 k_{z3}}{\epsilon_3 k_{z2} + \epsilon_2 k_{z3}} = r_{23}^p, \quad \text{proper} \\ \frac{-\epsilon_3 k_{z2} - \epsilon_2 k_{z3}}{-\epsilon_3 k_{z2} + \epsilon_2 k_{z3}} = \frac{1}{r_{23}^p}, \quad \text{improper} \end{cases} \tag{A.3}$$

Then,

$$\tilde{r} = \begin{cases} \frac{r_{12}^p + r_{23}^p e^{-jk_{z2}2d}}{1+r_{12}^p r_{23}^p e^{-jk_{z2}2d}} = \tilde{r}^p, \quad \text{proper} \\ \\ \frac{1/r_{12}^p + (1/r_{23}^p)e^{+jk_{z2}2d}}{1+1/(r_{23}^p r_{12}^p)e^{+jk_{z2}2d}} = \frac{r_{12}^p + r_{23}^p e^{-jk_{z2}2d}}{1+r_{12}^p r_{23}^p e^{-jk_{z2}2d}} = \tilde{r}^p, \quad \text{improper} \end{cases} \tag{A.4}$$

$$\tilde{t} = \begin{cases} \frac{(1+r_{12}^p+r_{23}^p+r_{12}^p r_{23}^p)e^{-jk_{z2}d}}{1+r_{12}^p r_{23}^p e^{-jk_{z2}2d}} = \tilde{t}^p, \quad \text{proper} \\ \\ \frac{(1+1/r_{12}^p+1/r_{23}^p+1/(r_{23}^p r_{12}^p)e^{+jk_{z2}d}}{1+1/(r_{23}^p r_{12}^p)e^{+jk_{z2}2d}} = \frac{(1+r_{12}^p+r_{23}^p+r_{12}^p r_{23}^p)e^{-jk_{z2}d}}{1+r_{12}^p r_{23}^p e^{-jk_{z2}2d}} = \tilde{t}^p, \quad \text{improper} \end{cases} \tag{A.5}$$

For the branch cut in $k_{z3}$,

$$\tilde{r} = \begin{cases} \frac{r_{12}+r_{23}^p e^{-jk_{z2}2d}}{1+r_{12}r_{23}^p e^{-jk_{z2}2d}} = \tilde{r}^p, \quad \text{proper} \\ \\ \frac{r_{12}+(1/r_{23}^p)e^{-jk_{z2}2d}}{1+(r_{12}/r_{23}^p)e^{-jk_{z2}2d}} = \frac{1+r_{12}r_{23}^p e^{+jk_{z2}2d}}{r_{12}+r_{23}^p e^{+jk_{z2}2d}} = \frac{1}{\tilde{r}^p}\Big|_{d\to -d}, \quad \text{improper} \end{cases} \tag{A.6}$$

$$\tilde{t} = \begin{cases} \frac{(1+r_{12}+r_{23}^p+r_{12}r_{23}^p)e^{-jk_{z2}d}}{1+r_{12}r_{23}^p e^{-jk_{z2}2d}} = \tilde{t}^p, \quad \text{proper} \\ \\ \frac{(1+r_{12}+1/r_{23}^p+r_{12}/r_{23}^p)e^{-jk_{z2}d}}{1+(r_{12}/r_{23}^p)e^{-jk_{z2}2d}} = \frac{(1+r_{12}+r_{23}^p+r_{12}r_{23}^p)e^{+jk_{z2}d}}{r_{12}+r_{23}^p e^{+jk_{z2}2d}} = \frac{\tilde{t}^p}{\tilde{r}^p}\Big|_{d\to -d}, \quad \text{improper} \end{cases} \tag{A.7}$$

Appendix B

# ADDITIONAL MATERIAL ON SPP MODES

## *B.1 Detailed field distributions of SPP modes*

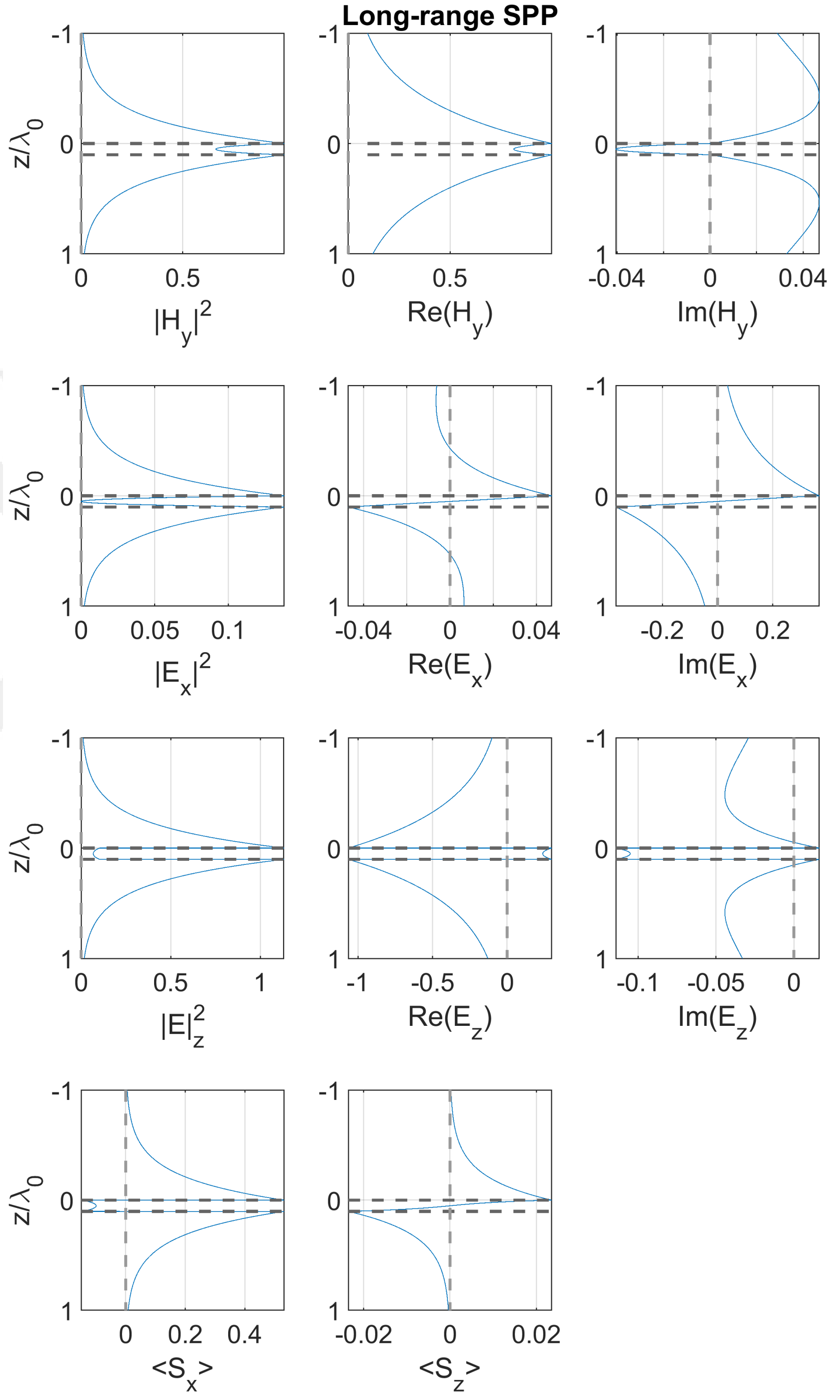


Figure B.1: The field and time-averaged Poynting vector distributions for the long-range SPP mode in the air-metal-air structure as shown in Figure 2.5.

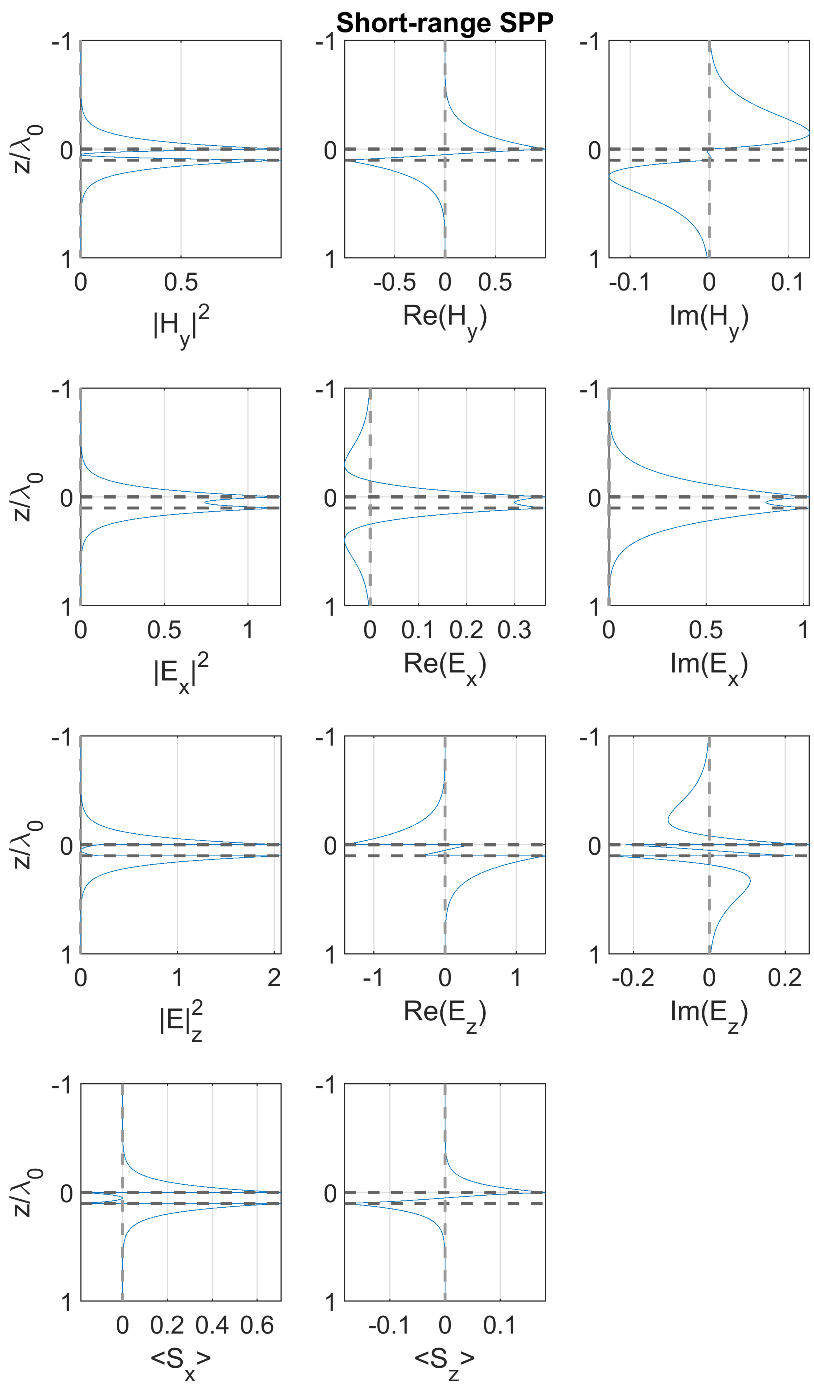


Figure B.2: The field and time-averaged Poynting vector distributions for the short-range SPP mode in the air-metal-air structure as shown in Figure 2.5.

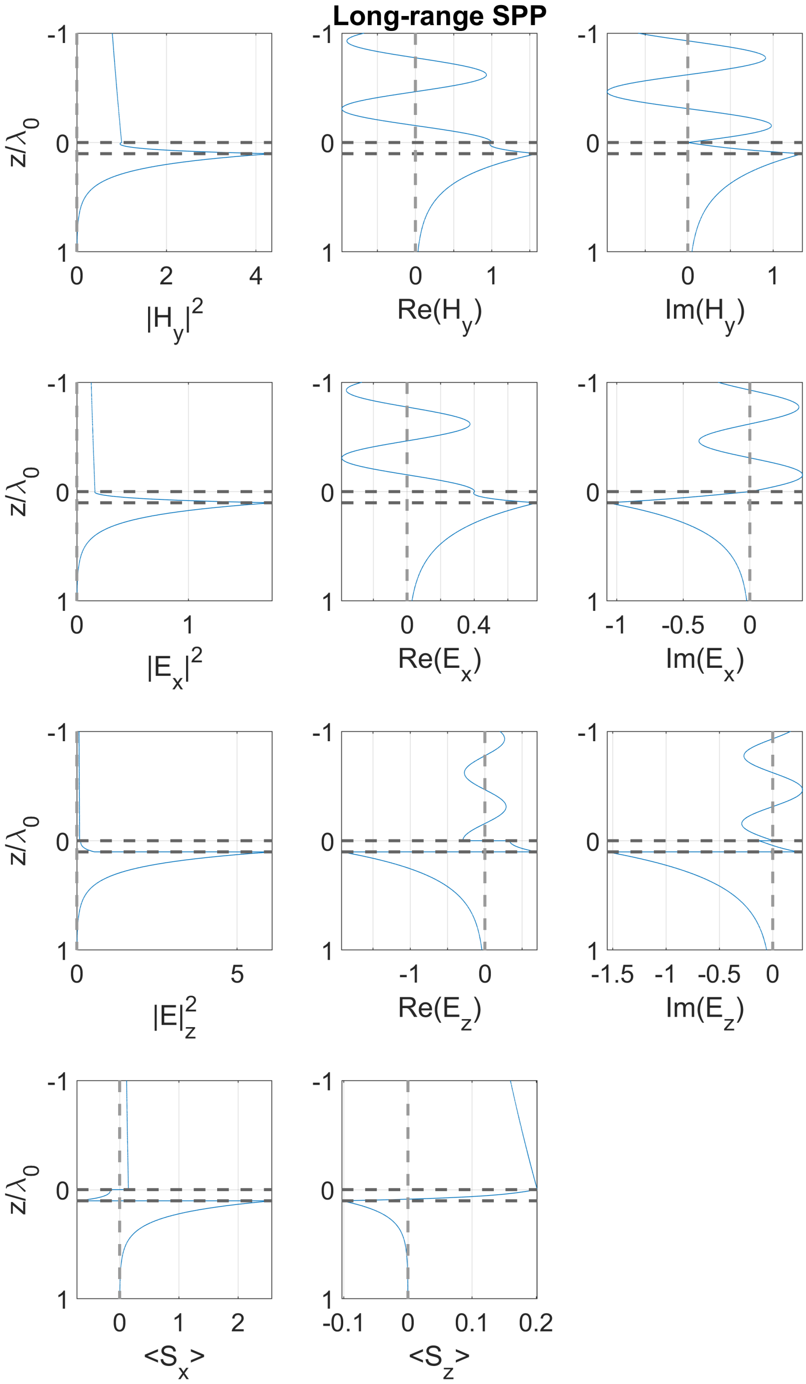


Figure B.3: The field and time-averaged Poynting vector distributions for the long-range SPP mode in the glass-metal-air structure as shown in Figure 2.8.

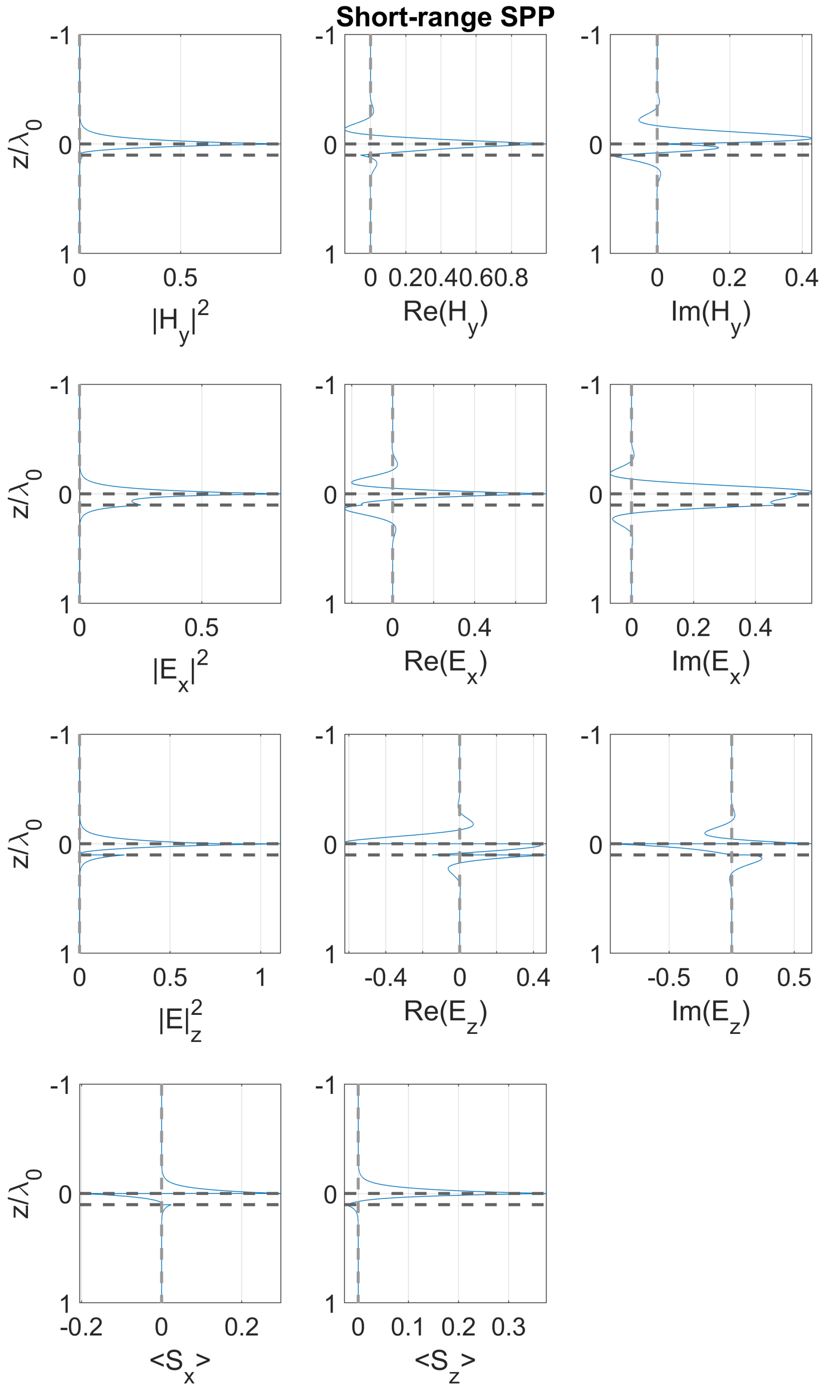


Figure B.4: The field and time-averaged Poynting vector distributions for the short-range SPP mode in the glass-metal-air structure as shown in Figure 2.8.

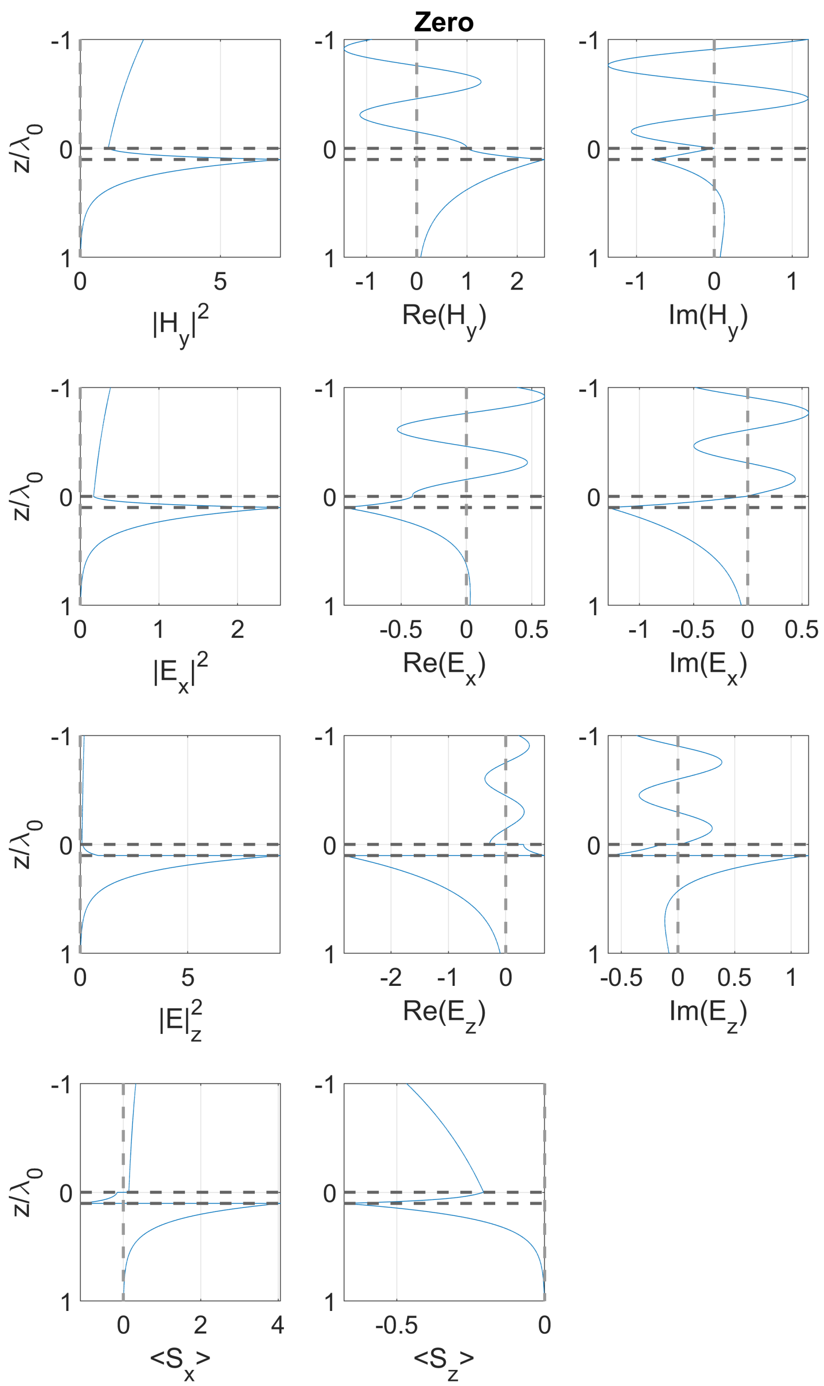


Figure B.5: The field and time-averaged Poynting vector distributions for the zero in the glass-metal-air structure as shown in Figure 2.8.

# Appendix C

# SUPPLEMENTARY MOVIES

## C.1 Supplementary Movie

A supplementary movie titled *Supplementary Movie MIM signal propagation* is available at *youtu.be/1_F6W0WAVNc*, showing the propagation of a complex SPP mode with a complex vector and a complex frequency in a metal-insulator-metal plasmonic waveguide. See Section 3.2.1 for details.

## C.2 Supplementary Movie

A supplementary movie titled *Supplementary Movie dispersion surface annotations* is available at *youtu.be/rfR7lPA4koQ*, showing various regions of the dispersion surface with annotations explaining their implications for plasmonic applications. See Section 3.3 for details.

## C.3 Supplementary Movie

A supplementary movie titled *Supplementary Movie convergence of 1D problem* is available at *youtu.be/Y4h2zTjymxc*, showing the convergence of the Fourier integral to the solution obtained using a single complex frequency. See Section 3.7.3 for details.

## C.4 Supplementary Movie

A supplementary movie titled *Supplementary Movie convergence of spp fields* is available at *youtu.be/vyfGilpVpcg*, showing the convergence of the Fourier integral to the solution obtained using a single SPP mode with a complex frequency. See

Section 3.7.3 for details.